ADSORPTION/DESORPTION STUDIES ON SOLID ACID ALKYLATION CATALYSTS USING A TAPERED ELEMENT OSCILLATING MICROBALANCE (TEOM)

By

Kening Gong

Submitted to the Department of Chemical & Petroleum Engineering and the Graduate Faculty of the University of Kansas in partial fulfillment of the requirements for the degree of Doctor of Philosophy.

Bala Subramaniam (Chairperson)

Palghat A. Ramachandran

Raghunath V. Chaudhari

Keith W. Hutchenson

Mikhail V. Barybin

Date defended: September 23, 2008

The Dissertation Committee for Kening Gong certifies
that this is the approved version of the following dissertation:

ADSORPTION/DESORPTION STUDIES ON SOLID ACID ALKYLATION CATALYSTS USING A TAPERED ELEMENT OSCILLATING MICROBALANCE (TEOM)

_____
Bala Subramaniam (Chairperson)

_____
Palghat A. Ramachandran

_____
Raghunath V. Chaudhari

_____
Keith W. Hutchenson

_____
Mikhail V. Barybin

Date approved:_____

Abstract

Developing economically viable solid acid catalyzed alkylation processes (as environmentally beneficial alternatives to conventional mineral acid based processes) continues to be a major goal of the refining industry. Comparative economic and environmental impact assessments of a conventional sulfuric acid based alkylation process with a previously developed CO_2-based alkylation process using SiO_2-supported Nafion catalyst indicate that the solid acid catalyst must be at least four times more active while providing > 80% C_8 alkylates selectivity for the process to be economically competitive with the conventional process. The Y- and β-zeolites display such activity and C_8 alkylates selectivity; however, they deactivate rapidly. Understanding the fundamentals of the adsorption, desorption, and mass transfer rates of reactants and products in these large-pore (12-ring) zeolites is key to rationally design/screen solid acid catalysts with the requisite performance criteria. This work uses a TEOM to elucidate for the first time the adsorption/desorption characteristics of alkylation reactants and products on these zeolites and some mesoporous materials.

Equilibrium adsorption isotherms were obtained on these catalysts using *n*-butane, isobutane, and propane as proxy reactant molecules (T = 303-398 K, adsorbate partial pressure 0-1.2 bar) and 224-trimethylpentane (224-TMP) as proxy product molecule (T = 298-473 K, $P_{224\text{-TMP}}$ = 0-0.3 bar). The dual-site Langmuir model provides good descriptions for the equilibrium adsorption isotherms of light alkanes and 224-TMP in β-zeolite at relatively low temperatures.

Analysis of the transient adsorption/desorption profiles of the reactant molecules from either a bed of the catalyst or pelletized particles of the crystals (with mean size < 1 μm) demonstrate that diffusion in the secondary meso-/macroporous structure formed in the packing or the pellets control the overall sorption rates. The experimental adsorption/desorption profiles from the pelletized zeolites were regressed with available mathematical models to obtain effective meso-/macropore diffusivities for reactant molecules, and nearly perfect fits of the experimental and the modeled profiles were obtained. Taking into account dead volume in the system, a reasonable criterion for reliable measurements of either micropore or mesopore diffusion time constant by the TEOM technique is derived as: $D/R^2 < 0.02\ s^{-1}$.

The desorption rates of 224-TMP from saturated β-zeolite by helium purging are extremely slow and discontinuous in nature, with a rapid "burst" of 224-TMP initially followed by a much slower transient. Further investigations using pelleted β-zeolites with different sizes suggest that the adsorption and initial desorption (the burst phase) of 224-TMP are controlled by meso-/macropore diffusion resistance and the long transient could be due to pore diffusion resistance within the zeolite crystals. The significant buildup of 224-TMP causes significant mass transport limitations inside the β-zeolite pores and will eventually lead to catalyst deactivation by fouling. In contrast, mesoporous silica materials provide good pore accessibility for large alkylate molecules such as 224-TMP, as evidenced by complete desorption of 224-TMP even at mild temperatures. This explains the longer catalyst life time observed by Lyon et al. in silica-supported Nafion catalyst.

Table of Contents

List of Tables

List of Figures

Acknowledgements

I would like to express my deep appreciation to my advisor Dr. Subramaniam for giving me the great opportunity to work with him and other outstanding researchers in the multidisciplinary research center CEBC, for his expert guidance on my research projects as well as on my future career, and for his encouragement and support at the various stages of my research work. I would also like to thank my other dissertation committee members (Dr. Ramachandran, Dr. Hutchenson, Dr. Chaudhari, and Dr. Barybin) for their time and instruction.

I am very grateful to the members of Solid Acid Catalysis Testbed at CEBC (faculty: Dr. Dudukovic, Dr. Ramachandran, Dr. Subramaniam, and Dr. Barybin; industrial liaison director: Dr. Fahey; postdoctoral research associate: Dr. Houndonougbo; and graduate students: Sagar Sarsani, Alexander Vorouchilov, and Subramanya Nayak) for their extremely valuable input to this dissertation research. I would like to thank Steve Chafin, Kent Pennybaker, Dr. Fahey, and Dr. Subramaniam for their instructions on the economic and environmental impact analyses. I would like to thank Dr. Ziebarth from GRACE-Davison for providing catalyst samples and technical support. I am also grateful to Dr. Hutchenson, Dr. Allison, and Dr. Yao for their help on the catalyst characterizations.

In addition, I would like to thank my colleagues in Dr. Subramaniam's research group (past and present): Dr. Shi, Dr. Snavley, Hong Jin, Chad Johnson, Bhuma

Rajagopalan, Sagar Sarsani, Jing Fang, Dr. Ford, Dr. Tang, Zhuanzhuan Xie, Madhav Ghanta, and Meng Li for their support, with my special appreciation given to Dr. Shi and Dr. Snavley for their help on the equipments.

I appreciate the help from the staff members at CEBC and KU Chemical & Petroleum Engineering Department (Dr. Lyon, James Busse, Dr. Bode, Deanna Bieberly, Dr. Niu, Ed Atchison, Nancy Crisp, Alan Walker, Scott Ramskill, and Jim Pilch).

This work was supported by the National Science Foundation, whose grant (Engineering Research Centers Program EEC-0310689) is gratefully acknowledged.

Finally, I would like to thank my wife Yaqin for accompanying me, and more importantly, for encouraging me to overcome various hurdles. I am also very grateful to my parents for their support over the vast Pacific Ocean.

Chapter 1 Introduction

Solid acid catalysts such as zeolites are considered to be environmentally benign alternatives to liquid mineral acids (e.g., sulfuric acid and hydrofluoric acid) and waste-generating Lewis acids (e.g., aluminum chloride) used in many industrial processes. Solid acids are promising alternatives because of their tunable Brønsted acidity, good thermal stability, and ease of separation. However, solid acid catalysts have found limited commercial applications because of rapid deactivation due to carbon deposition, unacceptable product quality, and catalyst instability under regeneration conditions. The Center for Environmentally Beneficial Catalysts (CEBC) is involved in research focused on the mitigation of these negative aspects of solid acids and the development of new types of solid acids with practical viability.

The alkylation of 1-butene with isobutane was chosen as a model system due to its industrial importance in gasoline production. Acylation of anisole and 2-methoxynaphthlene (2-MON) are also being studied due to their potential applications in the pharmaceutical industry. The objectives of the 1-butene+isobutane alkylation testbed are to:

- Develop catalysts that display activity, selectivity and durability that are either comparable to or better than known liquid and solid acids

- Develop a fundamental understanding of reaction mechanisms, including deactivation, and of the transport of reactant/product molecules in solid acid catalyzed processes in order to guide the rational design of solid acids for a given application

- Quantitatively assess the economic viability and lowered environmental impact potential for novel solid acid catalyzed processes to obtain performance metrics for process engineering and research guidance.

The foregoing objectives are being addressed at CEBC from four perspectives conforming to a systems approach: (1) development of novel acids and anchoring them to solid supports, (2) utilization of novel CO_2-expanded solvents to improve desorption and pore-transport of products, (3) fundamental kinetic studies and diffusion measurements, and (4) reactor- and molecular-scale modeling. Economic and environmental impact analyses identify the performance targets and benchmarks, thereby directing research activities in the most efficient direction. A brief summary of these activities along with the focus of the current dissertation are provided in the following paragraphs.

Irreversible adsorption of hydrocarbons on active sites is indicated as a major cause of deactivation in the alkylation reaction to produce gasoline fractions from C_4 hydrocarbons [deJong, 1996; Nivarthy, 1998; Weitkamp, 1999; Yoo, 2001; Platon, 2005]. The use of CO_2-based reaction media previously demonstrated that it is possible to enhance the diffusion of the products from the pores of the catalyst

thereby stabilizing catalyst activity [Lyon, 2001; Lyon, 2002; Lyon, 2004]. However, the selectivity towards trimethylpentanes (TMPs), the components that enhance the octane number, was in the 25-30% range which is not comparable to the liquid acid benchmark (70+% in both the sulfuric acid and hydrofluoric acid processes). Hence improved solid acid catalysts are needed.

In order to better understand adsorption/desorption and transport phenomena within the catalyst pore structure, a combination of experimental methods (Tapered Element Oscillating Microbalance (TEOM), Temporal Analysis of Products (TAP) reactor) together with Grand Canonical Monte Carlo (GCMC) simulations are being employed in the CEBC approach. In addition, reactor scale models at several hierarchical levels are being utilized, providing a rationale for reactor and process design.

The modeling work is led by Professor P. A. Ramachandran's group at Washington University in St. Louis and involves a study of a system of CSTRs with the kinetic model proposed by deJong and coworkers [deJong, 1996]. This scheme considered a direct reaction between isobutane and butene to form C_8 alkylate. However, according to the carbenium ion mechanism [Weitkamp, 1999], C_8 alkylate is only formed when hydride transfer occurs between C_8 carbocation with isobutane. To overcome this discrepancy, a new kinetic model was proposed, wherein 1-butene reacts with 1-butene on an active site to form C_8 carbocation. The formed C_8 carbocation either undergoes hydride transfer with isobutane or oligomerizes with 1-

butene in parallel reactions to form product alkylate or heavy hydrocarbons. As a result, this updated model suggests that greater intraparticle butene concentrations lead to more rapid deactivation.

On the catalyst design side, novel [C-H] acids have been synthesized by Professor Barybin's group in the Department of Chemistry at the University of Kansas and tested for acylation reactions. The rate and selectivity of the acylation processes involving new types of superacids synthesized at CEBC compare favorably with those employing silica-supported Nafion. Further catalyst development studies by the Barybin group included derivatization of the "parent" acid $C_6F_5CH(SO_2CF_3)_2$ at the *para*-position (relevant to catalyst support strategies), documentation of the solvent effect on the ultimate product distribution, and analysis of the origin of catalyst deactivation. Both the "parent" acid $C_6F_5CH(SO_2CF_3)_2$ and its *para*-alkoxy derivatives are highly active in catalyzing regioselective acylation of 2-MON. Importantly, no excess 2-MON is required and the acylation outcome is extremely solvent-dependent. In a polar medium, such as nitromethane, regioselective (> 90%) production of 2,6-AMN (acetylmethoxynaphthalene), which is a valuable pharmaceutical precursor, takes place. The mechanism of this reaction likely involves catalytic deacylation of 1,2-AMN (a kinetic product) and 1,6-diacylated 2-MON (a transient intermediate) during the competitive formation of 1,2-AMN and 2,6-AMN. On the other hand, in a nonpolar medium (e.g., hexane), exclusive and complete conversion of 2-MON into 1,2-AMN is observed. Thus, altering the solvent system allows regioselective production of either 1,2- or 2,6-AMN under homogeneous

conditions. Catalyst deactivation is dramatically less pronounced in the nonpolar reaction medium. NMR evidence clearly suggests that the conjugate base of the homogenous spent catalyst remains intact. However, at this time, regeneration of the catalyst back to its original acid form is difficult at best.

In order to facilitate catalyst separation, anchoring of these to solid supports is being investigated. Several supported versions of the above catalyst have been prepared and tested but invariably provided only small albeit regioselective conversions. The supporting strategies included (1) entrapment of the molecular catalyst in high surface area SiO_2, (2) covalent attachment of the derivatized molecular catalyst to porous silica networks, and (3) attachment of the molecular catalyst to a polymer backbone (e.g., polystyrene). The sol-gel method allowed incorporation of 13% of the [C-H] acid. The material has high surface area and pore volume (242 m^2/g, 0.44 cc/g). Acylation of 2-MON in the presence of the minute amounts of this catalyst (0.01% of the [C-H] unit) gave 2,6–AMN as the only product. Although this high selectivity was remarkable, the rather low conversion (5.5% after 24 h, 2-MON/Ac_2O = 1/1) and detectable catalyst leaching were observed leading to catalyst reusability problems.

One of the objectives of this dissertation research is to conduct rigorous economic and environmental impact analyses for the CO_2-based solid acid alkylation processes developed by CEBC researchers. It is essential to examine the commercial scale process concept early in the research development phase to determine performance

targets for economic viability. Such examination can further help researchers of catalyst, solvent, and reactor designs take important economic drivers into account. In addition, a corresponding environmental impact analysis would help us understand the potential environmental footprint of the alternative processes.

The economic and environmental impact analyses benchmarked the CO_2-based solid acid catalyzed alkylation process using silica-supported Nafion catalyst to the commercial DuPont/STRATCO process, revealing that there are clear environmental benefits (particularly related to acid rain formation) and that the novel process has the potential to be economically competitive, provided that more active and selective catalysts can be developed.

In a parallel investigation spurred by the economic analysis, Sarsani and Subramaniam [Sarsani, 2008] found that both β-zeolite and Y-zeolite show excellent initial activity and C_8 alkylates selectivity, comparable to those attained in the commercial liquid acid based processes. However, both β- and Y-zeolites deactivate rapidly with time-on-stream due to catalyst fouling. Typical experimental results obtained on β-zeolite are depicted in Figure 1-1 [Sarsani, 2008]. Initially, nearly complete butene conversion (99.5%+) is observed. After a certain period of time (5 min to 25 h, depending on operating conditions [deJong, 1996]), butene conversion starts to decrease and finally stabilizes at a certain level. The temporal profile of product selectivity follows the same trend: initially, the product is composed of paraffins exclusively (not shown in Figure 1-1) and the formation of the desired

product (TMPs) is high; almost simultaneously when the butene conversion deteriorates, the product quality begins to worsen, indicated by the drop of overall C_8 selectivity and TMP/C_8 selectivity. In the deteriorating stage, the cracking and oligomerization reactions occur, as evidenced by the onset of olefin formations (see Figure 1-1b). In the later stage, the desired alkylation reaction does not occur anymore, and the catalyst only promotes undesired reactions such as oligomerization and cracking.

(a)

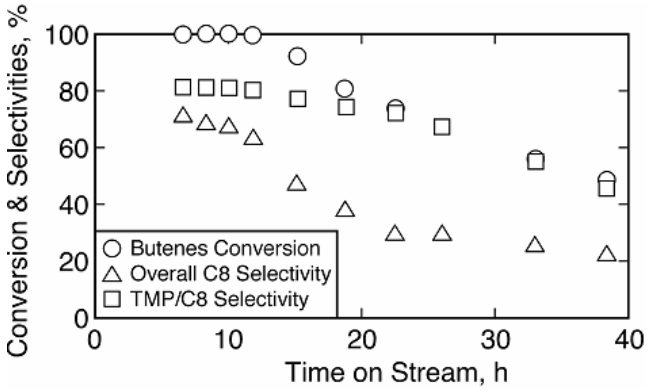

(b)

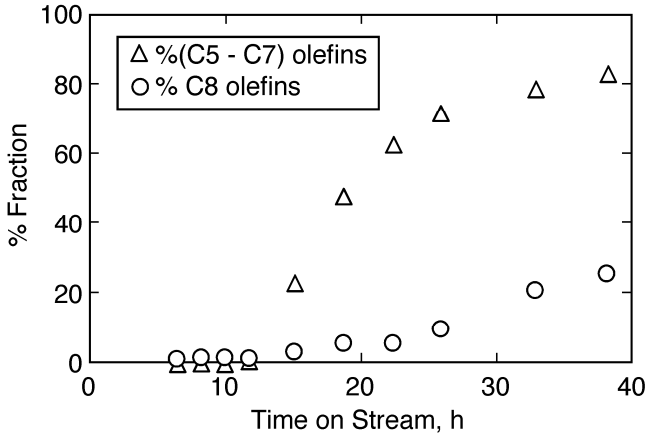

Figure 1-1. Temporal profiles of 1-butene+isobutane alkylation on β-zeolite (348 K, 40 bar, OSV = 0.11 h^{-1}, I/O = 5.0): (a) conversion and selectivity profiles; (b) olefin fraction profiles.

There seems to be a consensus that the slow adsorption/desorption and pore diffusion of the reactants and products (especially the heavy byproducts, such as C_{12} and C_{16}) is one of the crucial causative factors for catalyst deactivation in the solid acid catalyzed alkylation [deJong, 1996; Nivarthy, 1998; Weitkamp, 1999]. During liquid phase alkylation at sub-ambient temperatures, Sarsani and Subramaniam [Sarsani, 2008] have found that, β-zeolite catalyst is deactivated even before the desired products (TMPs) transport out of pores, indicating that the slow pore diffusion of the products plays a crucial role in the deactivation process. Yoo et al. [Yoo, 2001] studied the pore structure effects of different zeolites under mild to relatively severe deactivating conditions (353 K, 300 psig, I/O = 98, olefin WHSV = 0.1-0.5 h^{-1}) and found that the relatively small compounds formed during the reaction and hence the enhanced transport in the pores contribute to the longer catalyst life time observed in β-zeolite and ZSM-12. These results are instructive and clearly point out that a fundamental understanding of the adsorption, desorption and mass transfer rates of the reactants and products in the microporous and mesoporous catalysts is needed to screen potential solid acid catalysts and rationally determine operating conditions.

There are relatively few published reports aimed at investigating the adsorption/desorption and mass transfer phenomena of the reactants and products of alkylation in solid acid catalysts. Employing particles of different sizes (90-230 μm), Simpson and coworkers [Simpson, 1996, 1997] found that the alkylation in the large-

pore zeolite USHY is severely controlled by intraparticle diffusion of butenes under liquid-phase conditions at 373 K. The authors suggested placing the acid sites as a thin shell very close to the external surface of the particles to eliminate the intraparticle diffusion limitation. Albright [Albright, 1997] commented their work and suggested that the transfer steps of C_7-C_9 products should be investigated in addition to the diffusion of butenes (and isobutane), because the diffusivities of C_7-C_9 is relatively small and the accumulated products could possibly cause pore-blocking and further catalyst deactivation. However, such insights are not possible from the fixed bed reactor studies employed by Simpson and coworkers [Simpson, 1996, 1997]. Platon and Thomson [Platon, 2005] used the volumetric method to study butene and isobutane adsorption in β-zeolite, ZSM-5, and sulfated zirconia. They found that the adsorption equilibrium of butene was not attained even after 2 days, while the isobutane adsorption dynamics is relatively fast. These results provided insights into the competitive adsorption of butene and isobutane in solid acid catalysts. However, in Platon's work, the rate-limiting step for the adsorption/desorption of reactants was not identified, and the product adsorption/desorption was not considered.

The TEOM was found to be a valuable tool for fundamental studies of physicochemical behavior within porous catalysts. The catalyst is loaded onto a quartz element in the TEOM. Changes in the oscillation frequency of the element sensitively translate into small changes of the catalyst mass. This unique design prevents flowing gases from creating buoyancy effects and distorting the mass

measurement. The advantages of the TEOM technique have been demonstrated in the investigations of coking kinetics [Chen, 1996; Liu, 1997; Chen, 1999], influence of coke deposition on selectivity [Chen, 1997], combined diffusion, adsorption, reaction and coking [Hershkowitz, 1993; Chen, 1999; van Donk, 2001], adsorption capacity [Zhu, 1998], and adsorption and desorption kinetics [Barrie, 2004; Lee, 2004].

This dissertation research employs the TEOM to elucidate for the first time the adsorption/desorption characteristics of reactants and products in alkylation on large-pore (12-ring) zeolites. Specific objectives are to:

- Experimentally investigate equilibrium adsorption isotherms and adsorption/desorption rates of model compounds (olefins and paraffins) of relevance in 1-butene+isobutane alkylation on zeolites (and other solid acid catalysts), and

- Develop complementary theoretical models to reliably interpret the experimental data and obtain fundamental parameters.

The results generated from this project will aid researchers in rationally designing acid sites and supports. The fundamental adsorption and transport parameters are essential to rational particle engineering and reactor modeling studies.

Chapter 2 of this dissertation addresses the economic and environmental aspects of a conceptual solid acid/CO_2 alkylation process and identifies R&D targets for the solid acid processes to be economically viable. The methodology for the study of

adsorption/desorption of gases/vapors in porous catalysts by the TEOM technique is introduced in Chapter 3. The experimental data and model correlations of the equilibrium adsorption isotherms along with dynamic adsorption/desorption profiles of important alkylation reactants and products in zeolites and mesoporous materials are presented in Chapter 4 and 5. Finally, in Chapter 6, the conclusions of this work and the recommendations for future study are presented.

References

Albright, L. F., (1997). Kinetic analysis of isobutane/butene alkylations over ultrastable H-Y zeolite - Comments. Industrial & Engineering Chemistry Research 36, 2514-2516.

Barrie, P. J., Lee, C. K., Gladden, L. F., (2004). Adsorption and desorption kinetics of hydrocarbons in FCC catalysts studied using a tapered element oscillating microbalance (TEOM). Part 2: numerical simulations. Chemical Engineering Science 59, 1139-1151.

Chen, D., Gronvold, A., Rebo, H. P., Moljord, K., Holmen, A., (1996). Catalyst deactivation studied by conventional and oscillating microbalance reactors. Applied Catalysis A: General 137, L1-L8.

Chen, D., Rebo, H. P., Moljord, K., Holmen, A., (1997). Influence of coke deposition on selectivity in zeolite catalysis. Industrial & Engineering Chemistry Research 36, 3473-3479.

Chen, D., Rebo, H. P., Moljord, K., Holmen, A., (1999). Methanol conversion to light olefins over SAPO-34. Sorption, diffusion, and catalytic reactions. Industrial & Engineering Chemistry Research 38, 4241-4249.

deJong, K. P., Mesters, C. M. A. M., Peferoen, D. G. R., vanBrugge, P. T. M., deGroot, C., (1996). Paraffin alkylation using zeolite catalysts in a slurry reactor: Chemical engineering principles to extend catalyst lifetime. Chemical Engineering Science 51, 2053-2060.

Hershkowitz, F., Madiara, P. D., (1993). Simultaneous measurement of adsorption, reaction, and coke using a pulsed microbalance reactor. Industrial & Engineering Chemistry Research 32, 2969-2974.

Lee, C. K., Ashtekar, S., Gladden, L. F., Barrie, P. J., (2004). Adsorption and desorption kinetics of hydrocarbons in FCC catalysts studied using a tapered element oscillating microbalance (TEOM). Part 1: experimental measurements. Chemical Engineering Science 59, 1131-1138.

Liu, K., Fung, S. C., Ho, T. C., Rumschitzki, D. S., (1997). Kinetics of catalyst coking in heptane reforming over Pt-Re/Al_2O_3. Industrial & Engineering Chemistry Research 36, 3264-3274.

Lyon, C., Subramaniam, B., Pereira, C., (2001). Enhanced isooctane yields for 1-butene/isobutane alkylation on SiO_2-supported Nafion in supercritical carbon dioxide. Catalyst Deactivation 2001, Proceedings 139, 221-228.

Lyon, C. J., Optimization of activity and selectivity by pressure-tuning during solid-acid catalyzed isoparaffin/olefin alkylation in supercritical carbon dioxide, Thesis (Ph. D.), University of Kansas, Chemical and Petroleum Engineering, 2002.

Lyon, C. J., Sarsani, V. S. R., Subramaniam, B., (2004). 1-butene plus isobutane reactions on solid acid catalysts in dense CO_2-based reaction media: Experiments and modeling. Industrial & Engineering Chemistry Research 43, 4809-4814.

Nivarthy, G. S., He, Y. J., Seshan, K., Lercher, J. A., (1998). Elementary mechanistic steps and the influence of process variables in isobutane alkylation over H-BEA. Journal of Catalysis 176, 192-203.

Platon, A., Thomson, W. J., (2005). Solid acid characteristics and isobutane/butene alkylation. Applied Catalysis A: General 282, 93-100.

Sarsani, V. S. R., Subramaniam, B., (2008). Isobutane/butene alkylation on microporous and mesoporous solid acid catalysts: Probing the pore transport effects with liquid and near critical reaction media. Submitted to Green Chemistry.

Simpson, M. F., Wei, J., Sundaresan, S., (1996). Kinetic analysis of isobutane/butene alkylation over ultrastable H-Y zeolite. Industrial & Engineering Chemistry Research 35, 3861-3873.

Simpson, M. F., Wei, J., Sundaresan, S., (1997). Kinetic analysis of isobutane/butene alkylations over ultrastable H-Y zeolite - Rebuttal. Industrial & Engineering Chemistry Research 36, 2517-2520.

van Donk, S., Broersma, A., Gijzeman, O. L. J., van Bokhoven, J. A., Bitter, J. H., de Jong, K. P., (2001). Combined diffusion, adsorption, and reaction studies of *n*-hexane hydroisomerization over Pt/H-mordenite in an oscillating microbalance. Journal of Catalysis 204, 272-280.

Weitkamp, J., Traa, Y., (1999). Isobutane/butene alkylation on solid catalysts. Where do we stand? Catalysis Today 49, 193-199.

Yoo, K., Burckle, E. C., Smirniotis, P. G., (2001). Comparison of protonated zeolites with various dimensionalities for the liquid phase alkylation of *i*-butane with 2-butene. Catalysis Letters 74, 85-90.

Zhu, W., van de Graaf, J. M., van den Broeke, L. J. P., Kapteijn, F., Moulijn, J. A., (1998). TEOM: A unique technique for measuring adsorption properties. Light alkanes in silicalite-1. Industrial & Engineering Chemistry Research 37, 1934-1942.

Chapter 2 Economic and Environmental Impact Analyses of Solid Acid Catalyzed Isoparaffin/Olefin Alkylation in Supercritical Carbon Dioxide

HYSYS-based process simulation was accomplished for a recently reported 1-butene+isobutane alkylation concept that employs SiO_2-supported Nafion catalyst in dense CO_2 media to obtain stable C_8 alkylates production (solid acid/CO_2 process developed by CEBC researchers). Semi-quantitative economic and environmental impact assessments were conducted for this novel process design along with comparative assessments for a conventional sulfuric acid catalyzed alkylation process (at equivalent production capacities). This evaluation illustrates the advantages and shortcomings of the novel process and provides rational research guidance. For example, the analyses established performance targets, such as catalyst activity and operating pressure, for the solid acid/CO_2 process to be commercially viable. The economic and environmental impact analyses shown in this chapter have already been published [Gong, 2008].

2.1. Introduction

Alkylation of isoparaffins by olefins is used commercially to produce

nonaromatic high-octane blending feedstock for gasoline. Conventionally, alkylation units use mineral acids, that is, sulfuric acid (such as those licensed by DuPont/STRATCO and ExxonMobil) or hydrofluoric acid (such as those licensed by ConocoPhillips and UOP), as catalysts. The main characteristics of these processes are described in detail elsewhere [Corma, 1993]. Because of safety and environmental issues associated with the sulfuric acid and hydrofluoric acid based alkylation units, there is a strong driving force for developing effective alkylation processes using solid acid catalysts.

A variety of materials including zeolites, sulfated metal oxides, acidic resins, and heteropoly acids were examined as solid acid catalysts for isoparaffin/olefin alkylation. However, rapid catalyst deactivation (presumably due to heavy hydrocarbon deposition) and declining product quality with time on stream are the main obstacles to commercialization of solid acid based alkylation [Weitkamp, 1999].

Supercritical fluids have been shown to provide an optimal combination of liquid-like (solvent) properties and gas-like (transport) properties to maximize desorption and removal of coke precursors from the solid catalyst pore structure. Recently, steady C_8 alkylate production, lasting up to 2 days in a slurry reactor, was observed by Lyon et al. when using a SiO_2-supported Nafion catalyst for 1-butene+isobutane alkylation in dense CO_2-based reaction mixtures [Lyon, 2004]. It was also observed that high pressure CO_2 (> 130 bar, at a temperature of 368 K) can be used to dissolve and extract retained hydrocarbons from the catalyst pores. After four

alkylation/extraction cycles (the reaction was operated at 79 bar for 24 h followed by a cleaning step with pure CO_2 for 9−12 h), most of the activity and selectivity were maintained. On the basis of these preliminary experiments, a design for a novel solid acid/CO_2 alkylation process was developed. Process simulations were executed by HYSYS [Hyprotech, 2002] to obtain the mass and energy balances for the whole process.

The main purpose of this analysis is to compare the economics and environmental footprint of the solid acid/CO_2 process with those of the sulfuric acid process. Obviously, a credible comparison requires a better than crude qualitative assessment.

Semiquantitative assessments of new processes are commonly performed at various stages of process development. However, literature articles that describe a semiquantitative economic evaluation with an environmental impact assessment are relatively rare and normally test or demonstrate assessment methods [Azapagic, 1999; Chen, 2004]. Among these analyses, the work done by Dunn and Savage [Dunn, 2003] was found to be unique; a novel terephthalic acid process using high-temperature water as an alternative medium was designed and evaluated on the basis of experimental data. More recently, Fang et al. [Fang, 2007] performed a comparative economic and environmental impact analysis of a novel CO_2-based hydroformylation process and a simulated conventional process. Such evaluations provide guidance for future research that addresses both economic and environmental issues. The work presented herein is considered a semi-quantitative evaluation of the

economics as well as a rigorous assessment of the environmental impact for both the solid acid/CO_2 and the sulfuric acid processes. The advantages and shortcomings of the solid acid/CO_2 process are revealed to guide future research directions.

2.2. Methodology

2.2.1. Economic Assessment

2.2.1.1. Process Design

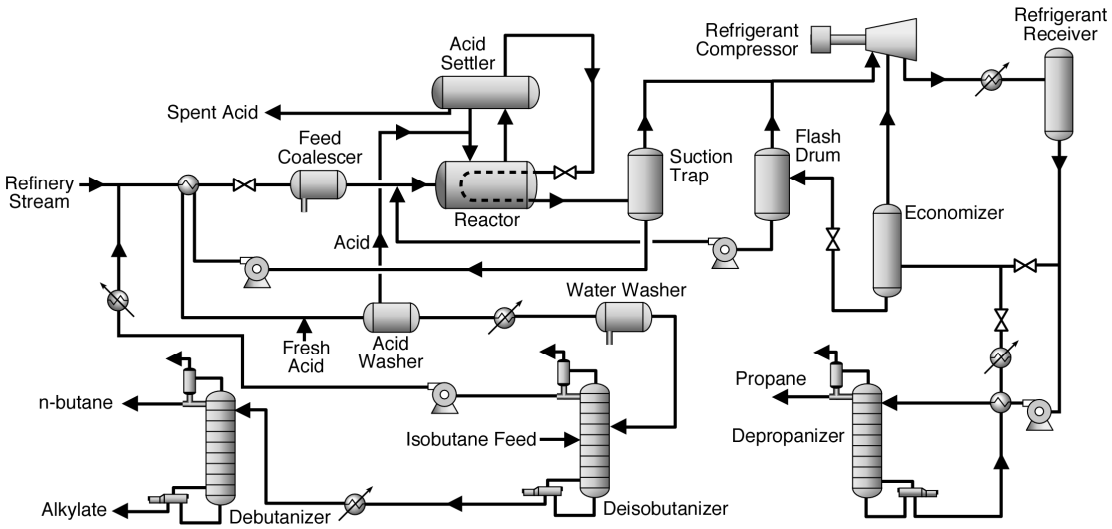

Figure 2-1. Sulfuric acid effluent refrigeration alkylation process.

The sulfuric acid effluent refrigeration alkylation process, as shown in Figure 2-1, was chosen as a reference case [Albright, 1990a, b]. A refinery stream (containing butenes, isobutane, *n*-butane, and others) combined with recycled isobutane is fed into a horizontal contactor, and the hydrocarbons are separated from the acid

emulsion in an acid settler. A suction trap/flash drum is used to flash the hydrocarbons into vapor and liquid phases. The vapor phase goes to the refrigeration section where propane is separated out and isobutane and other components recycle back to the alkylation reactor. The liquid phase is fed into the distillation sections where isobutane, *n*-butane, and alkylates are separated and either recovered or recycled.

An alkylation plant using the novel solid acid/CO_2 process was designed and is shown in Figure 2-2. In this plant, the isobutane and CO_2 recycle streams are fed to four online parallel reactors with three beds in each reactor. Figure 2-2 shows only one of the alkylation reactors, but the design incorporates six reactors, four of which are on line with two undergoing regeneration at any time. Between each catalyst bed, the refinery stream is fed into the side of the reactors to achieve high *I/O* ratios at all times. This reactor configuration was found to be the most economical option to enable reasonable wall thickness and bed height for the reactors. The vapor products exiting the reactors pass though the final stage of the compressor to achieve the desired inlet pressure for each reactor. The liquid products at the bottom of each bed are withdrawn from the reactor and depressurized by feeding into a flash tank. To further separate CO_2 and other components, a second-stage flash tank (operating at a lower pressure) and a distillation column are employed. The vapor products (CO_2-rich) of both flash tanks and the distillation column are fed into the compressor and recycled back to the reactor inlets. Once CO_2 separation is achieved, Figure 2-2

illustrates that the product recovery steps by distillation are similar to the sulfuric acid effluent refrigeration process (Figure 2-1).

Note that the reaction stoichiometries are different for the two processes. In the sulfuric acid process, the product is dominated by C_8 paraffin, and an isobutane makeup stream (containing isobutane, *n*-butane, and others) is introduced. In contrast, in the solid acid/CO_2 process, approximately half of the product is C_8 olefin, which is produced by the dimerization of the butenes; consequently, isobutane in the refinery stream is abundant and extra isobutane is withdrawn from the top of the deisobutanizer as a product.

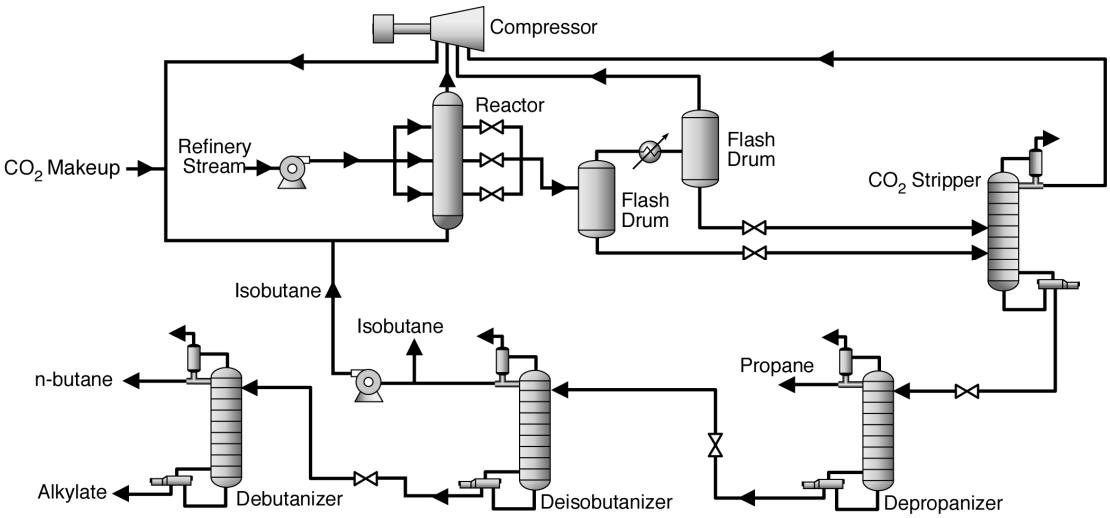

Figure 2-2. Proposed solid acid/CO_2 alkylation process.

2.2.1.2. Simulation Parameters

The same refinery stream compositions [Meyer, 1983] are used for both processes, and the overall alkylates production capacity is assumed to be 3660

bbl/day (at standard conditions) for both processes. The simulation parameters of the sulfuric acid process are obtained from published plant data [Meyer, 1983; Corma, 1993; Branzaru, 2001]. The operating parameters for the reactors in the solid acid/CO_2 process are obtained from the laboratory-scale experiments [Lyon, 2001; Lyon, 2002; Lyon, 2004]. The key operating parameters for the reactors for each process are summarized in Table 2-1.

As stated earlier, solid acid regeneration by CO_2 pressure-tuned technology has been demonstrated [Lyon, 2004]. In the current analysis, regeneration systems are designed and simulated as a part of the whole solid acid/CO_2 process. It is assumed that, during regeneration, CO_2 is fed to the reactor at 140 bar and 368 K for 12 h with a residence time of 3 min [Lyon, 2004]. In contrast, the reaction cycle lasts for 24 h for each reactor [Lyon, 2004].

Table 2-1. Key Operating Parameters of the Reactors for Each Process

operating conditions		sulfuric acid process	solid acid/CO_2 process
reactor type		contactor	fixed-bed
catalyst		H_2SO_4	Nafion
temperature	K	280	368
pressure	bar	5	86
olefin conversion	%, per pass	100	77
alkylate selectivity	%, mass	79	27
olefin space velocity		0.3 h^{-1}	0.05 $g_{olefin}/g_{catalyst}h$
isobutane/olefin ratio		8	5
CO_2 concentration	%, mole	0	70
catalyst fraction	%, volume	50	69

Note that the long-term activity and selectivity by using pressure-tuned technology have not been tested and the true lifetime for the SiO_2-supported Nafion catalyst is still unknown. It is assumed that the catalyst life is two years and the catalyst activity and selectivity can be maintained by using pressure-tuned regeneration.

2.2.1.3. Estimate of Capital Investment

The cost of purchased equipment is treated as the basis of the evaluation for the capital investment. The estimates can vary in accuracy from ±5 to ±30% [Peters, 2003]. The sizes and specifications of the equipment are determined from equipment parameters either assumed or calculated [Walas, 1988; Peters, 2003], using the material and energy balances obtained from process simulator HYSYS [Hyprotech, 2002]. All the purchased equipment costs are estimated on an attribute such as capacity, material used, or surface area [Walas, 1988]. The economic analyses herein were conducted during 2005−2006, and all the costs are adjusted to 2005 dollars using the Chemical Engineering Plant Cost Index (CEPCI) [CEPCI, 2005].

The purchased cost for a compressor or pump is estimated on the basis of the power required. The stages needed for the compressor are constricted by temperature limitations of the lubricating oil and other factors. The compressor for the CO_2 recycling in the solid acid/CO_2 process has three stages with a compression ratio of approximately 2.1 per stage [Walas, 1988]. The compressors are assumed to be

operating with efficiency of 72% [Walas, 1988]. All the compressors and pumps are driven by electric motors.

The sizes of the vessels are estimated on the basis of the holding time, which is assumed to be 5 min for most cases [Walas, 1988]. However, for the acid washer and acid settler in the sulfuric acid process, the holding times are assumed to be 30 and 22.5 min, respectively, because of the slowness of the acid/hydrocarbon separation in both liquid–liquid separators [Branzaru, 2001].

Surface areas needed for heat exchange are used as the basis for the heat-exchanger equipment cost. The ranges of overall heat-transfer coefficients are estimated on the basis of different types of streams used, and the average values are chosen as the overall heat-transfer coefficients for cost estimation [Peters, 2003]. For both processes, 150 psig steam is used for the reboilers of all the distillation columns except the deisobutanizers, which are heated by 50 psig steam [Walas, 1988]. The input and output temperatures of cooling water are set at 305 and 313 K, respectively [Walas, 1988].

The costs of the distillation columns are calculated on the basis of the tray diameters and tray number information. The tray diameters of the distillation columns are sized by HYSYS [Hyprotech, 2002] tray sizing function. The numbers and feed tray positions of the distillation columns are optimized to have the lowest energy consumptions.

The reactor for the sulfuric acid process is assumed to be essentially an acid resistant heat exchanger with multiple tubes inside [Peters, 2003]. For the solid acid/CO_2 process, the fixed bed reactors are designed for pressure and throughput requirements with appropriate wall thickness, diameter, and length [Walas, 1988].

The total installed costs are estimated by multiplying the purchase costs for equipment with an installation factor, which strongly depends upon the type of the equipment and the material used [Walas, 1988].

The fixed capital investment is composed of two types of costs: direct costs and indirect costs. The direct costs include the total installed equipment investments and the costs for buildings, yard improvement, and land usage. Because the capacities of both plants are identical, it is assumed that the costs for buildings, yard improvement, and land are identical, and they are calculated as 0.34 times the purchased equipment costs of the sulfuric acid process [Peters, 2003]. The indirect costs include the costs for supervision, legal expenses, construction expenses, contractor fees, and so forth. In this analysis, the indirect costs for each process are assumed to be 1.51 times the purchased equipment costs [Peters, 2003].

The working capital is assumed to be 18% of the fixed capital investment [Peters, 2003]. The total capital investment is composed of fixed capital and working capital investments.

2.2.1.4. Estimate of Utility and Chemical Costs

The amounts of various utilities (e.g., steam, cooling water, and electricity) consumed in both processes are determined from energy and material balances obtained by HYSYS [Hyprotech, 2002].

In the sulfuric acid process, the acid strength is maintained above 90% by weight for process effectiveness [Meyer, 1983]. The spent acid is regenerated in an off-site sulfuric acid plant. Here, we assume that acid consumption is 30 lb/barrel of alkylate [Meyer, 1983; Gary, 2001]. Also, the caustic consumption is assumed to be 0.2 lb/barrel of alkylate [Gary, 2001]. For the solid acid/CO_2 process, the consumption of solid acid catalyst is estimated on the basis of the assumptions of olefin space velocity (OSV), capacity of the plant, and the catalyst life presented earlier.

2.2.1.5. Estimate of Net Profit

The total production costs include manufacturing costs and general costs. Manufacturing costs include raw material costs, utility costs, operating labor, operating supplies, and so forth. All the items of manufacturing costs are assumed to be identical for both processes except the raw material costs, utility and chemical costs, depreciation, and financing [Peters, 2003]. The operating labor costs are estimated on the basis of the number of principal processing steps and the plant capacity [Peters, 2003]. For both processes, the number of principal processing steps and the plant capacity are essentially identical. Therefore, the operating labor costs

for both processes are estimated to be the same. Depreciation rate is assumed to be 10% for each year, and the financing is assumed to be 5% of the total capital investment [Peters, 2003]. The general expenses include administrative costs, distribution and marketing costs, and research and development costs. It is assumed that the general expenses for both processes are identical and are estimated as 20% of the total production costs for the sulfuric acid process [Peters, 2003]. Gross earnings are the total income less total production cost. The income tax rate is assumed to be 35% of gross earnings, and the net profit is the gross earnings after tax [Peters, 2003].

2.2.2. Environmental Impact Assessment

The environmental impact analysis employed is based on a systematic risk assessment methodology developed by Allen and Shonnard [Allen, 2002].

It is believed that the impact of chemicals on the environment or human health is a function of dose, which actually is a function of concentration, and the concentration is, in turn, a function of emissions. On the basis of this theory, the rigorous environmental impact method employed in this analysis includes four phases.

- Phase 1, Process Simulation: Provides the mass and energy balances via the process simulator HYSYS.

- Phase 2, Emission Estimation: Estimates major unit emissions using industry emission factors [Allen, 2002].

- Phase 3, Chemical Partition Estimation: Estimates concentrations of chemicals in four environments (air, water, soil, and sediment).

- Phase 4, Process Composite Index Estimation: Converts the concentrations to probabilities of harm to the environment and humans.

Phases 2, 3, and 4 are integrated into the module EFRAT (Environmental Fate and Risk Assessment Tool) [Chen, 2003; Chen, 2004], which is programmed to extract information from a HYSYS simulator.

2.2.2.1. Process Simulation

The environmental impact evaluation is based on the process design, stream compositions, and operating conditions. Details for the process simulation using HYSYS were discussed in previous sections.

2.2.2.2. Emission Estimation

After identifying the major sources of emission, we used industry emission factors for chemical process units to calculate emission rates from process units such as distillation columns and compressors. The emission rates from process units are the total mass flow rates of volatile organic compounds in the streams or process units multiplied by the industry emission factors for that type of process unit. The industry emission factors for various process units were summarized elsewhere [Allen, 2002].

The emission sources considered in this evaluation include distillation columns, utilities, fugitive, and so forth.

The distillation columns operate at relatively high pressure (> 5 bar), and emission occurs through the distillation column vents, so the emission factor is assumed to be 0.2 g/kg throughput [Allen, 2002].

Natural gas is chosen as the fuel to produce steam and electricity. Large industrial boilers with low nitrogen oxides emissions are assumed. The emission factors for the gas−electric generating units are listed in *Energy Facts 1992* by the U.S. Department of Energy [DOE, 1992]. The emission factors for sulfur dioxide, nitrogen oxides, and carbon monoxide from natural gas combustion are listed in AP-42 document by the U.S. Environmental Protection Agency (EPA) [EPA, 1995].

For emissions from valves, compressor seals, pump seals, and so forth, the average emission factors for fugitive emissions in the refinery industry are used [EPA, 1995]. For both processes, emissions from all the main pumps, compressors, and pressure-relief valves are considered.

For the conventional process, sulfuric acid emissions have a great impact on the environment. The emissions are divided into two categories: in-site emission that occurs in the alkylation unit and off-site emission that occurs during the transportation, regeneration, and storage external to the alkylation unit (the spent acid is usually regenerated in an off-site sulfuric acid manufacturing plant). In the sulfuric

acid alkylation process, the acid/hydrocarbon emulsion (50% acid) continuously flows to the acid settler. The acid returns to the reactor after it has separated from the hydrocarbon phase. A small amount of fresh acid is continuously charged to the acid settler, and an equivalent amount of spent acid is withdrawn at the same time. For the in-site emission estimation, each step of the acid handling is assumed to have the same SO_2 emission as during a tank car/truck unloading or 0.05 g/kg of sulfuric acid [EPA, 1995]. The off-site emission factors of acid, SO_2, NO_2, and CO_2 for sulfuric acid regeneration, transportation, and storage are listed in the EPA AP-42 document [EPA, 1995].

For the solid acid/CO_2 process, the environmental impact for catalyst regeneration is also considered by calculating the emissions from the regeneration cycle.

2.2.2.3. Chemical Partition Estimation

After the emission rates are calculated, the concentrations of the emitted chemicals in water, air, and other media are estimated. The concentrations in these "compartments" of the environment are dependent on the rates and types of emissions, the locations, and the properties of the chemicals.

A modified "level I" multimedia fugacity model [Mackay, 2001] is used to transform the emissions into environmental concentrations. This model predicts the emission distribution in four compartments (air, surface water, soil, and sediment), assuming constant emissions are released to the environment. For simplification, only

two parameters related to the properties of chemicals (Henry's constant and the octanol–water partition coefficient) are used in the prediction [Allen, 2002]. The parameters are obtained from the CHEMFATE database [SRC, 2005] or estimated from EPIWIN [EPA, 2004].

2.2.2.4. Process Composite Index Estimation

The last part of the environmental impact assessment is to convert the concentration of the chemicals in different environmental compartments to the probability of harm to the environment and humans. A comprehensive listing of impact categories, including global warming, ozone depletion, smog formation, acid rain, inhalation toxicity, ingestion toxicity, inhalation carcinogenicity, ingestion carcinogenicity, and fish aquatic toxicity, is used to evaluate the processes. The process composite index estimation includes three steps.

First, relative risk indices are calculated to estimate the relative environmental impact and toxicity of the chemical of interest to the benchmark compounds. Detailed definitions of relative risk indices were summarized elsewhere [Allen, 2002]. The only needed parameters to calculate the relative risk indices are environmental impact potentials (e.g., acid rain potential ARP) and toxicities (e.g., lethal concentration LC50), which were measured by experiments [Allen, 2002] or estimated by EPIWIN [EPA, 2004].

Second, normalized risk indices for each environmental impact category (e.g., global warming) are calculated using the following equation:

$$I_k^N = \sum_{i=1}^{n} \left(E_i \cdot I_{i,k}^* \right) \Big/ \overline{E}_k \cdot \left\langle I^* \right\rangle_k \tag{2-1}$$

where I_k^N is the normalized risk index for environmental impact category k, E_i is the total emission rate of chemical compound i from all the sources considered in the process, $I_{i,k}^*$ is the relative risk index of chemical compound i for each impact category k, $\overline{E}_k$ is the national, annual emission rate of chemicals for the impact category k, and $\left\langle I^* \right\rangle_k$ is the average relative risk index for chemicals of importance to the national inventory. The values of $\overline{E}_k$ and $\left\langle I^* \right\rangle_k$ are summarized elsewhere [Chen, 2003].

Finally, one single index, a process composite index, which considers the effects of different categories for the whole process is calculated using the following equation:

$$I_{PC} = \sum_k I_k^N \cdot W_k \tag{2-2}$$

where W_k is the impact category k weighting factor from Eco-Indicator 95 [Goedkoop, 1995; Chen, 2003].

2.3. Results and Discussion

2.3.1. Economic Assessment

2.3.1.1. Material Balance, Raw Material Costs, and Product Sales Revenues

Table 2-2. Comparison of Material Balance, Raw Material Costs, and Product Sales Revenues for Sulfuric Acid Alkylation Process and Solid Acid/CO_2 Alkylation Process

Sulfuric Acid Alkylation Process

	refinery stream	isobutane feed	propane product	*n*-butane product	alkylate product
propane (BPSD)[a]	216	2	220		
propene (BPSD)	254				
i-butane (BPSD)	2145	150	4	3	
n-butane (BPSD)	681	108		635	154
butenes (BPSD)	1748				
i-pentane (BPSD)	49	5		10	215
C_{6+} alkylate (BPSD)					3295
total (BPSD)	5093	265	224	647	3664
raw material costs (millions of dollars/year)	−47.0	−1.4			
product sales revenues (millions of dollars/year)			2.2	7.1	110.1

Solid Acid/CO_2 Alkylation Process

	refinery stream	CO_2 feed	propane product	*n*-butane product	isobutane product	alkylate product
propane (BPSD)	328		320		7	
propene (BPSD)	386		2			
i-butane (BPSD)	3256		5	3	2021	
n-butane (BPSD)	1034			791	78	164
butenes (BPSD)	2653			3	21	
i-pentane (BPSD)	74			12		227
CO_2 (BPSD)		4	2			
C_8 olefin (BPSD)						1550
C_{6+} alkylate (BPSD)						1717
total (BPSD)	7730		329	809	2128	3658
raw material costs (millions of dollars/year)	−71.4	−0.1				
product sales revenues (millions of dollars/year)			3.2	8.9	15.0	110.7

[a] BPSD: Barrels per stream day.

Table 2-2 shows the material balances, raw material costs, and product sales revenues for both processes. For the solid acid/CO_2 process, more olefins are required

and more unreacted paraffins are recovered by distillation and sold. This can be explained by the fact that the reaction stoichiometries are different for the two processes (i.e., for the solid acid/CO_2 process, more olefins are consumed to form C_8 olefins), as discussed in Section 2.2.1.1.

2.3.1.2. Capital Investments

The purchased and installed costs for major equipment of both processes are shown in Table 2-3. The total installed costs for the major equipment are estimated to be $15.9 million for the sulfuric acid process and $21.7 million for the solid acid/CO_2 process. The major equipment includes the processing equipment (compressors, pumps, vessels, reactors, heat exchangers, and distillation columns) as well as the storage vessels for raw material and finished products (storage tanks). Meyer and co-workers [Meyer, 1983] estimated the total installed cost of processing equipment for the sulfuric acid alkylation process (with the same capacity) in 1983 dollars. This cost updated to year 2005 using the CEPCI [CEPCI, 2005] was approximately $14.0 million, which is close to our estimate of $14.3 million.

Both processes involve the compression of large recycle streams and require comparable energy input. As a result, the overall costs for compressors and pumps for both processes are similar.

In the solid acid/CO_2 process, no equipment is needed for refrigeration and acid/water treatment, but there are extra costs for some storage tanks. In comparing the two processes, the overall costs for vessels and storage tanks are similar.

Table 2-3. Equipment Costs for the Sulfuric Acid Process and Solid Acid/CO_2 Process, in Millions of Dollars

	sulfuric acid process		solid acid/CO_2 process	
	purchased cost	installed cost	purchased cost	installed cost
compressors and pumps	2.3	3.2	1.9	3.0
vessels and storage tanks	1.5	3.9	1.8	4.9
reactors	2.4	5.2	3.4	7.4
heat exchangers	0.6	1.2	0.7	1.4
distillation columns	0.8	2.3	1.6	4.9
total	7.6	15.9	9.4	21.7

In the sulfuric acid process, because of heat exchange and liquid circulation requirements, the contactor reactor is complicated with multiple tubes inside and an impeller at the end of the reactor shell. As a result, the two reactor vessels are expensive. In the solid acid/CO_2 process, there are six fixed-bed thick-walled reactors (four online and two offline reactors). The two sulfuric acid reactors are estimated to cost 71% as much as the six solid acid reactors.

The distillation equipment costs for the solid acid/CO_2 process are approximately double that of the sulfuric acid process. For the solid acid/CO_2 process, an extra distillation column for the separation of CO_2 from the C_{3+} compounds is needed. In addition, relatively larger columns for the same purposes are required because of higher throughputs in the solid acid/CO_2 process. For example, the deisobutanizer in

the solid acid/CO_2 process has a diameter of 3.05 m and height of 38 m, and the same column in the sulfuric acid process has a diameter of 2.44 m and height of 35 m.

The capital costs for both processes are shown in Table 2-4. The sulfuric acid fixed capital investment is estimated herein as $29.4 million. This is in rough agreement with the $25.6 million estimate (updated to year 2005 dollars) taken from published investment curves (alkylate production vs alkylation unit investment) for a unit with the same capacity [Gary, 2001].

Table 2-4. Capital Investments for the Sulfuric Acid Process and Solid Acid/CO_2 Process, in Millions of Dollars

	sulfuric acid process	solid acid/CO_2 process
direct costs (installed equipment)	15.9	21.7
direct costs (others)	2.6	2.6
indirect costs	10.9	13.6
fixed capital investment	29.4	37.8
working capital	5.2	6.7
total capital investment	34.5	44.5

The total capital investment of the solid acid/CO_2 process is estimated to be 20–30% higher than that of the sulfuric acid process.

2.3.1.3. Utility and Chemical Costs

The utility and chemical costs (variable costs) for both processes are summarized in Table 2-5. The steam, cooling water, and electricity costs estimated by Meyer and co-workers [Meyer, 1983] for the sulfuric acid process with the same capacity are $2.2, 0.22, and 1.23/bbl true alkylate (TA), respectively, after updating to year 2005

values. The electricity price depends upon the location, and that contributes to the large difference in the electricity costs (for our estimation, it is $0.49/bbl TA).

Table 2-5. Utility and Chemical Costs for the Sulfuric Acid Process and Solid Acid/CO_2 Process

	sulfuric acid process		solid acid/CO_2 process	
	consumed/bbl	cost $/bbl	consumed/bbl	cost $/bbl
utilities[a]				
steam, lb	252.18	1.79	382.65	2.72
power, kWh	10.23	0.49	6.61	0.31
cooling water, 1000 gal	2.54	0.23	2.60	0.23
chemicals[b]				
catalyst, lb	30.00	2.40	0.38	5.58
caustic, lb	0.20	0.03		
total		4.94		8.85

[a] Respective utility costs: steam ($7.12/1000 lb), power ($0.05/kWh), cooling water ($0.09/1000 gal).
[b] Respective chemical costs: sulfuric acid ($0.08/lb), caustic ($0.15/lb), solid acid catalyst ($14.80/lb). Price information was provided by River City Engineering, Inc.

The solid acid/CO_2 process requires more steam mainly because of the higher energy requirement of the distillation column reboilers. Costs for power and cooling water are essentially identical for both processes and are only a small part in the total utility costs. Catalyst costs for both processes account for a significant portion in the total variable costs. Here, it is assumed that one batch of solid acid catalyst can be used for two years by using pressure-tuned regeneration, though the viability of repetitive catalyst regenerations has not yet been studied. The solid acid cost comprises more than 60% of the variable costs because of its modest activity; for the sulfuric acid process, catalyst cost is approximately 50% of the variable costs. If the solid acid catalyst price can be reduced by 50% or the catalyst lifetime can be

extended to more than four years, the variable costs for the two processes could be almost identical.

2.3.1.4. Net Profit

Total income, total production costs, gross earnings, and net profit are shown in Table 2-6. The income from the solid acid/CO_2 process is approximately 15% higher than the sulfuric acid process mainly because of the selling of extra isobutane product in the solid acid/CO_2 process as shown in the mass balance section. However, the total production cost for the solid acid/CO_2 process is 29% higher than that of the sulfuric acid process. As a result, the net profit of the solid acid/CO_2 process is only 40–50% of the sulfuric acid process.

Table 2-6. Total Income, Total Production Costs, Gross Earnings, and Net Profit for the Sulfuric Acid Process and Solid Acid/CO_2 Process, in Millions of Dollars/Year

	sulfuric acid process	solid acid/CO_2 process
total income	119.4	137.9
total production costs	101.0	130.1
gross earnings	18.4	7.8
net profit	11.9	5.1

2.3.1.5. Effect of Olefin Space Velocity, Pressure, and Temperature

For the solid acid/CO_2 process, the costs for reactors and catalyst are significantly higher than that of the sulfuric acid process because of the modest activity of the solid acid catalysts. If a higher OSV can be utilized with a commensurately higher activity catalyst, thereby maintaining the per pass feedstock conversions and the quality of the

product, the costs for reactors and catalyst will be reduced (the costs for distillation columns, vessels, storage tanks, etc., are insensitive to OSV), resulting in improvement of process economics. A sensitivity analysis of installed reactor cost, total capital investment, and utility and chemical costs to OSV is shown in Figure 2-3. If the OSV is doubled (from 0.05 to 0.10 $g_{olefin}/g_{catalyst}h$), the installed reactor cost is approximately equal to that of the sulfuric acid process, but the total capital investment is still 10–20% higher than that of the sulfuric acid process mainly because of higher costs of distillation columns, vessels, and storage tanks. If the OSV increases to 0.20 $g_{olefin}/g_{catalyst}h$, the higher costs of distillation columns, vessels, and storage tanks can be offset by the lower costs of reactors. In this scenario, the total capital investment for the solid acid/CO_2 process is \$36.4 million, which is fairly close to the value of the sulfuric acid process (\$34.5 million).

The normal regeneration pressure for the reactor is 140 bar. If this pressure can be reduced to the normal reaction pressure (below 90 bar), the reactor cost can be reduced significantly because of a less-demanding strength requirement. In addition, a separate compressor might not be needed for the regeneration, and less energy will be used to recompress the recycle stream. It is estimated that if the regeneration pressure can be as low as 90 bar, the fixed capital investment will be roughly \$3.7 million less than the base case. If the normal regeneration and reaction pressure is lower than 50 bar, the total capital investment is \$36.8 million, which is comparable with that of the sulfuric acid process; in addition, the total annual operating cost decreases by \$1.1

million, mainly because of the reduced energy demand for compression. The feasibility of lower pressure operation needs to be investigated in further research.

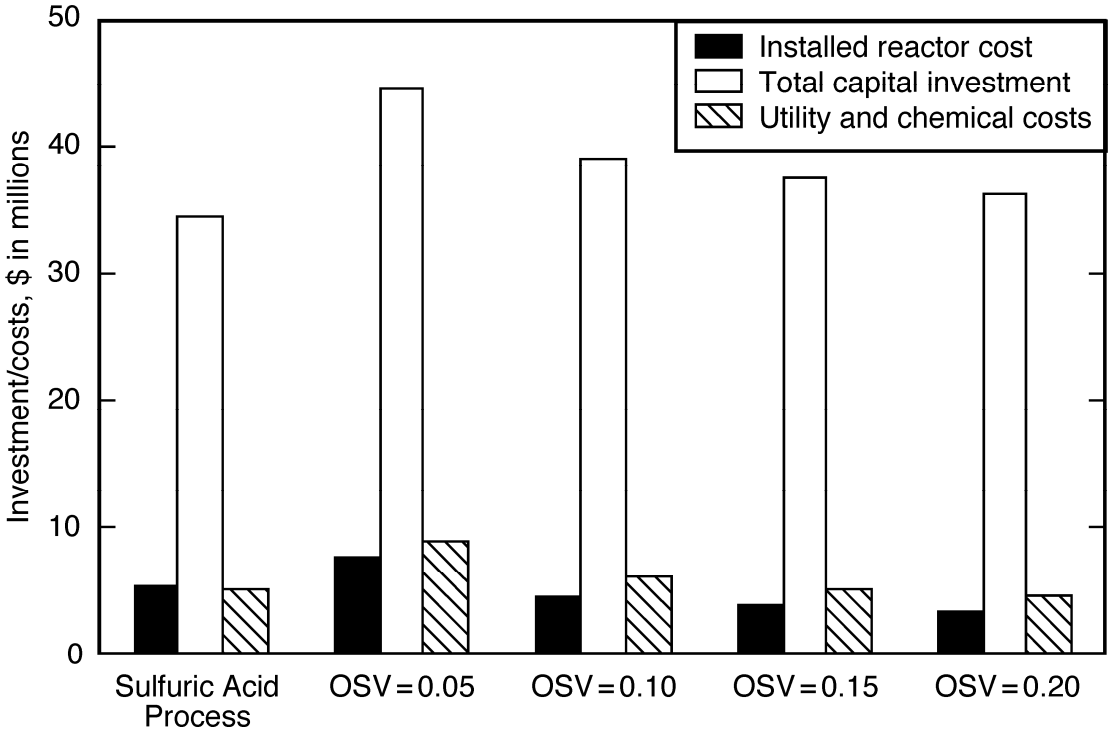

Figure 2-3. Sensitivity analysis of installed reactor cost, total capital investment, and utility and chemical costs to OSV ($g_{olefin}/g_{catalyst}h$).

The operating temperature used in the reaction and regeneration for the solid acid/CO_2 process is around 368 K. The feed olefin can be heated by the heat produced during the alkylation reaction; essentially no heat is needed to maintain the operating temperature. The utilities needed for the plant are mostly for the distillation columns and compressors. Accordingly, the capital investment, the utility and chemical costs, and the net profit are essentially not temperature dependent.

2.3.2. Environmental Impact Assessment

2.3.2.1. Emission Estimation

After the process simulation (Phase 1), the second phase of this rigorous environmental risk assessment is to estimate the emissions of chemicals involved in each process. The emission evaluations for both processes are shown in Table 2-7.

Table 2-7. Potential Emissions of Chemicals from the Sulfuric Acid and Solid Acid/CO_2 Alkylation Processes, 10^3 kg/yr

chemicals	sulfuric acid process	solid acid/CO_2 process
carbon dioxide	27540	36250
nitrogen dioxide	21.7	26.1
sulfur dioxide	758.9	0.2
propane	5.7	3.8
butenes	0.0	1.1
isobutane	63.1	26.2
n-butane	14.5	9.0
isopentane	0.3	0.4
octenes	0.0	1.2
sulfuric acid	22.7	0.0
2,2,4-trimethylpentane	0.5	0.1
2,2,3-trimethylpentane	0.6	0.1
2,3-dimethylhexane	0.2	0.4
others	4.1	3.8
total	28430	36320

In the sulfuric acid process, a large amount of sulfuric acid is used as catalyst in the alkylation unit and the spent acid needs to be regenerated in an off-site sulfuric acid manufacturing plant. The emission factors for SO_2 and sulfuric acid in sulfuric acid regeneration plants are high because of the inefficiency of the emission controls

[EPA, 1995]. As a result, high emissions of sulfur dioxide and sulfuric acid from the sulfuric acid process are shown in Table 2-7. Note that in the solid acid/CO_2 process, the emission of SO_2 comes from combustion of natural gas in the boiler.

Note that carbon dioxide emissions account for 96.8 and 99.8% of the total emissions from the sulfuric acid and solid acid/CO_2 processes, respectively, implying that both processes are energy intensive. Most CO_2 emissions come from the boilers for steam and electricity generation. The higher rates of CO_2 and NO_2 emissions from the solid acid/CO_2 process are due to greater fuel consumption. Note that solvent CO_2 in the solid acid/CO_2 process does not contribute to CO_2 emissions.

Because the products in the sulfuric acid process do not contain C_8 olefin and butenes, there are no emissions of these compounds from the conventional process. The lower emission rate for isobutane from the solid acid/CO_2 process is due to lower recycle rate.

Total potential chemical emissions from the solid acid/CO_2 process are approximately 28% higher than that from the sulfuric acid process. However, higher levels of emissions do not necessarily translate to greater environmental impact. The toxicity and partition properties of the emitted chemicals also must be considered in the overall environmental impact analysis.

2.3.2.2. Chemical Partition Estimation

The predicted partitioning of the emitted chemicals into the four environmental compartments is shown in Table 2-8. Most of the emissions remain in the air compartment creating air pollution problems, and they can affect human health through inhalation. The table indicates that no chemicals remain in the sediment compartment and only small percentages of chemicals remain in the soil.

Interestingly, all the sulfuric acid stays in the water compartment because of the low volatility of the acid. As a result, this analysis indicates that approximately 2.3×10^4 kg/yr of sulfuric acid is released to the water compartment by the sulfuric acid process.

2.3.2.3. Process Composite Index Estimation

Figure 2-4 displays the process composite indices (IPCs) for both processes as well as the contributions to the two IPCs from inhalation toxicity, global warming, and acid rain. The effects of other environmental impact categories are essentially negligible.

For the sulfuric acid process, it is not surprising that the major contributor to the process composite index is acid rain (66%), because sulfuric acid and sulfur dioxide are major emissions from in-site acid leakage and off-site sulfuric acid regeneration, transportation, and storage. Even though the acid rain potential for NO_2 (0.70) is similar to that of SO_2 (1.00), the NO_2 emissions contribution to the acid rain is small,

because of the low NO_2 emission rate. The inhalation toxicity index comprises 32% of the composite index for the sulfuric acid process. Because most of the emitted chemicals remain in the air compartment, there is a high risk of human inhalation. The global warming index comprises less than 2% of the composite index for the sulfuric acid process.

Table 2-8. Partitioning of the Emitted Chemicals into the Environmental Compartments

	percent in			
chemicals	air	sediment	soil	water
carbon dioxide	99.8			0.2
nitrogen dioxide	99.9			0.1
sulfur dioxide	93.1			6.9
propane	100.0			
butenes	100.0			
isobutane	100.0			
n-butane	100.0			
isopentane	100.0			
octenes	99.8		0.2	
sulfuric acid				100.0
2,2,4-trimethylpentane	100.0			
2,2,3-trimethylpentane	99.8		0.2	
2,3-dimethylhexane	100.0			

According to this analysis, the sulfuric acid process has more potential impact on inhalation toxicity (1.5 times) and acid rain (43 times) in comparison to the solid acid/CO_2 process. For global warming, the sulfuric acid process has less (0.77 times) impact mainly because of its lower CO_2 emission rates. Overall, the sulfuric acid process has a much higher (3.9 times) adverse environmental impact potential than does the solid acid/CO_2 process.

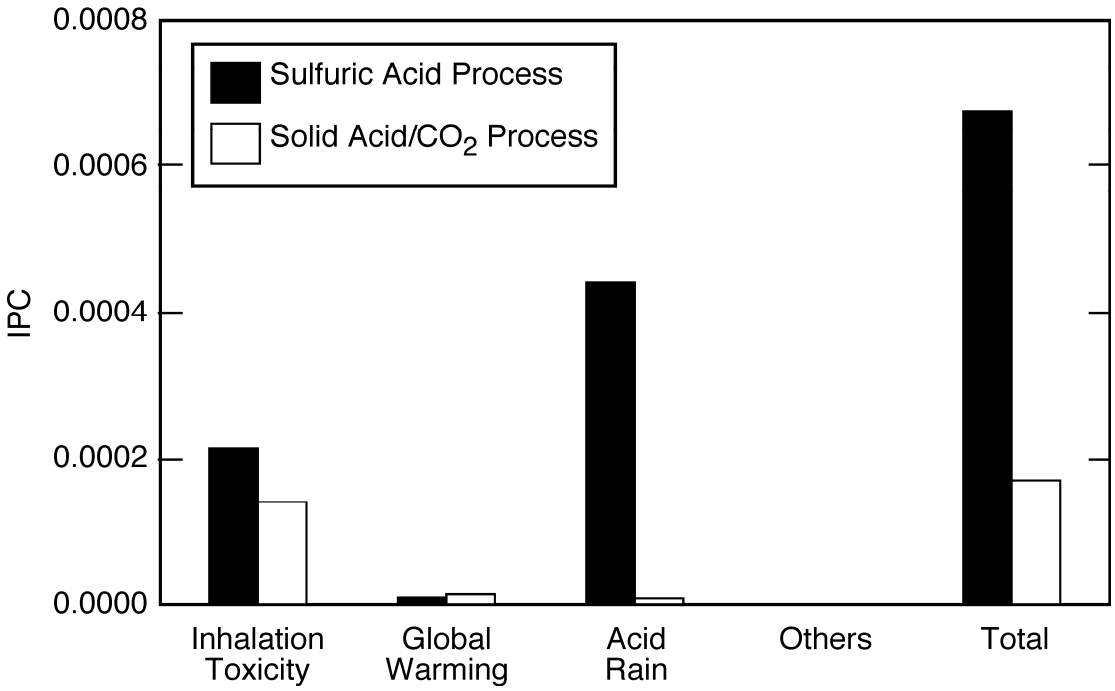

Figure 2-4. IPCs for both processes and the contributions to the two IPCs from various environmental impact categories. (To calculate the contributions to IPC from various environmental impact categories, weighting factors are considered. For example, for the acid rain category, the value shown is $I^{N}_{Acidrain} \cdot W_{Acidrain}$.)

For the solid acid/CO_2 process, the major contributor to composite index is the inhalation toxicity index (83%), followed by the global warming risk index (10%) and acid rain risk index (6%).

Figure 2-5 illustrates the top five pollution sources in both processes, with the sizes of the pie charts reflecting relative total environmental impact potentials.

For the sulfuric acid process, the main pollution sources are SO_2 emission during sulfuric acid regeneration (53%) and acid leakage in the alkylation process (10%).

For the solid acid/CO_2 process, the main pollution sources are fugitive emissions (61%), because the solid acid/CO_2 process operates at relatively high pressure and no sulfuric acid is used in the process.

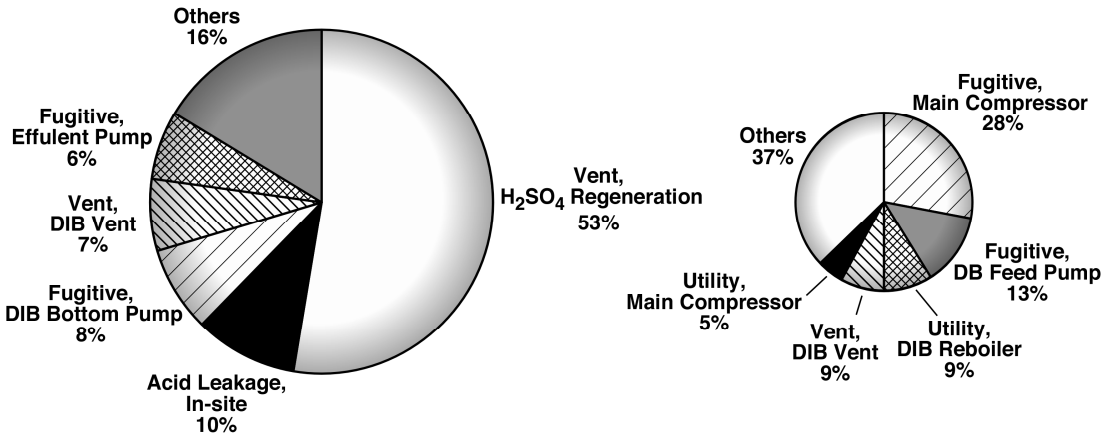

Figure 2-5. Contributions to IPC from different process operating units (the sulfuric acid process is on the left and the solid acid/CO_2 process is on the right).

2.4. Conclusions

Economic and environmental impact assessments of a solid acid/CO_2 alkylation process using SiO_2-supported Nafion catalyst and a conventional sulfuric acid alkylation process (with the same feed refinery stream compositions and the same capacity for alkylate production) have been conducted using plant scale simulations. It is found that for the solid acid/CO_2 process the consumption of the C_4 olefin is higher than that of the sulfuric acid process. For the solid acid/CO_2 process, no

isobutane makeup stream is needed and the extra isobutane is withdrawn from the top of the deisobutanizer as a product.

Capital investment, utility and chemical costs, and net profits are compared for each process. The results show that the total capital investment of the solid acid/CO_2 process is 20–30% higher than that of the sulfuric acid process. For the solid acid/CO_2 process, the utility and chemical costs are 70–80% higher than the sulfuric acid process mainly because of the modest activity of the solid acid catalyst. In addition, it is estimated that the net profit of the solid acid/CO_2 process is 40–50% of the sulfuric acid process. Sensitivity analysis shows that the utility and chemical costs and capital investment decrease as OSV increases for the solid acid/CO_2 process. If the OSV can be increased by a factor of 4 from the base-case value while maintaining the same C_8 alkylate productivity, the total capital investments along with the utility and chemical costs would be nearly the same for both processes.

The environmental impact assessment shows that the emission rate of sulfur dioxide and sulfuric acid is much higher for the sulfuric acid process. A modified "level I" multimedia fugacity model is used to estimate the chemical distribution in multienvironmental compartments, and it is estimated that almost all the sulfuric acid stays in the water compartment while the other chemicals mostly stay in the air compartment.

It is estimated that the sulfuric acid process has a much higher (approximately 3.9 times) adverse environmental impact potential than the solid acid/CO_2 process. For

the sulfuric acid process, the major contributors to the process composite index are acid rain (66%) and inhalation toxicity (32%). For the solid acid/CO_2 process, the major contributors to the process composite index are inhalation toxicity (83%), global warming (10%), and acid rain (6%).

The top pollution sources are also identified for both processes. For the sulfuric acid process, the main pollution comes from the SO_2 emissions during sulfuric acid regeneration (53%) and acid leakage in the alkylation unit (10%). For the solid acid/CO_2 process, the main pollution sources are fugitive emissions.

The current economic and environmental impact analysis shows the advantages and disadvantages of the novel process and provides rational guidance for future research. For example, quantitative performance targets, with respect to catalyst activity and operating pressure, have been proposed to ensure that the newly developed solid acid catalyzed alkylation processes are indeed commercially viable.

References

Albright, L. F., (1990a). Alkylation will be key process in reformulated gasoline era. Oil & Gas Journal 88, 79-92.

Albright, L. F., (1990b). H_2SO_4, HF processes compared, and new technologies revealed. Oil & Gas Journal 88, 70-77.

Allen, D. T., Shonnard, D., (2002) Green engineering: Environmentally conscious design of chemical processes, Prentice Hall: Upper Saddle River, NJ.

Azapagic, A., Clift, R., (1999). The application of life cycle assessment to process optimisation. Computers & Chemical Engineering 23, 1509-1526.

Branzaru, J., (2001). Introduction to sulfuric acid alkylation unit process design. Stratco Inc. Publication.

CEPCI, (2005). Chemical engineering plant cost index. Chemical Engineering, 76.

Chen, H., Shonnard, D. Safety and Chemical Engineering Education (SAChE) faculty workshop, Baton Rouge, LA, 2003.

Chen, H., Shonnard, D. R., (2004). Systematic framework for environmentally conscious chemical process design: Early and detailed design stages. Industrial & Engineering Chemistry Research 43, 535-552.

Corma, A., Martinez, A., (1993). Chemistry, catalysts, and processes for isoparaffin-olefin alkylation - Actual situation and future trends. Catalysis Reviews-Science and Engineering 35, 483-570.

DOE "Energy factors 1992," U.S. Department of Energy, 1992.

Dunn, J. B., Savage, P. E., (2003). Economic and environmental assessment of high-temperature water as a medium for terephthalic acid synthesis. Green Chemistry 5, 649-655.

EPA "Compilation of air pollutant emission factors: Stationary point and area sources," U.S. Environmental Protection Agency, 1995.

EPA; 3.12 ed.; U.S. Environmental Protection Agency, 2004.

Fang, J., Jin, H., Ruddy, T., Pennybaker, K., Fahey, D., Subramaniam, B., (2007). Economic and environmental impact analyses of catalytic olefin hydroformylation in CO_2-expanded liquid (CXL) media. Industrial & Engineering Chemistry Research 46, 8687-8692.

Gary, J. H., Handwerk, G. E., (2001) Petroleum refining: Technology and economics, 4th, Marcel Dekker: New York.

Goedkoop, M. "The Eco-Indicator 95: Weighting method for environmental effects that damage ecosystem or human health on a European scale," Pré Consultants, 1995.

Gong, K., Chafin, S., Pennybaker, K., Fahey, D., Subramaniam, B., (2008). Economic and environmental impact analyses of solid acid catalyzed

isoparaffin/olefin alkylation in supercritical carbon dioxide. Industrial & Engineering Chemistry Research (in press).

Hyprotech; 3.1 ed.; Hyprotech Ltd, 2002.

Lyon, C., Subramaniam, B., Pereira, C., (2001). Enhanced isooctane yields for 1-butene/isobutane alkylation on SiO_2-supported Nafion in supercritical carbon dioxide. Catalyst Deactivation 2001, Proceedings 139, 221-228.

Lyon, C. J., Optimization of activity and selectivity by pressure-tuning during solid-acid catalyzed isoparaffin/olefin alkylation in supercritical carbon dioxide, Thesis (Ph. D.), University of Kansas, Chemical and Petroleum Engineering, 2002.

Lyon, C. J., Sarsani, V. S. R., Subramaniam, B., (2004). 1-butene plus isobutane reactions on solid acid catalysts in dense CO_2-based reaction media: Experiments and modeling. Industrial & Engineering Chemistry Research 43, 4809-4814.

Mackay, D., (2001) Multimedia environmental models: The fugacity approach, 2nd, Lewis Publishers: Boca Raton.

Meyer, D. W., Chapin, L. E., Muir, R. F., (1983). The payoff in pilot plants - Cost-benefits of sulfuric-acid alkylation. Chemical Engineering Progress 79, 59-65.

Peters, M. S., Timmerhaus, K. D., West, R. E., (2003) Plant design and economics for chemical engineers, 5th, McGraw Hill: Boston.

SRC; Syracuse Research Corporation, 2005.

Walas, S. M., (1988) Chemical process equipment: Selection and design, Butterworths: Boston.

Weitkamp, J., Traa, Y., (1999). Isobutane/butene alkylation on solid catalysts. Where do we stand? Catalysis Today 49, 193-199.

Chapter 3 The Application of TEOM to Study Adsorption and Desorption in Porous Catalysts

The TEOM technique was initially designed for *in situ* monitoring of particulate concentrations in the effluents of combustion systems [Patashnick, 1980; Wang, 1980]. The uniquely designed TEOM instruments were capable of measuring a wide range of particulate concentrations (in the range of $\mu g/m^3$ to g/m^3), by monitoring the mass change of a filter cartridge as gas (containing dust) passing through it.

In the early 1990's, the Rupprecht & Patashnick TEOM 1500 PMA was developed for laboratory studies of gas-solid reactions. Since then, the advantages of the TEOM technique have been demonstrated in the investigations of coking kinetics [Chen, 1996; Liu, 1997; Chen, 1999], influence of coke deposition on selectivity [Chen, 1997], combined diffusion, adsorption, reaction and coking [Hershkowitz, 1993; Chen, 1999; van Donk, 2001], adsorption capacity [Zhu, 1998], and adsorption and desorption kinetics [Barrie, 2004; Lee, 2004].

A TEOM (Series 1500 Pulse Mass Analyzer) is used in this work for *in situ* measurements of the transient hydrocarbon adsorption and desorption on zeolites and mesoporous materials. In this chapter, the operating principles of the TEOM technique are introduced in detail. Then a comparison is made between TEOM and other commonly used macroscopic methods for adsorption/desorption equilibrium

and kinetics measurements. In addition, the detailed experimental procedure is described. Finally, the gas density effect is investigated to better understand and quantitatively characterize the systematic errors of the adsorption/desorption measurements.

3.1. Principles

A schematic diagram of a TEOM is shown in Figure 3-1. At the center of the TEOM is a tapered element (TE), which is used to restrain the solid sample in the bed with inert quartz wool, as well as to measure the mass change of the sample. The carrier gas enters the top part of the tapered element, proceeds downward through the hollow section and then passes through the packed bed, where it comes into intimate contact with the solid samples. A purge gas passes down around the tapered element to guide and direct the carrier gas stream as it exits from the tapered element (such a design helps to prevent effluent gas diffusing back into the tapered element). Inside the TEOM, there are two heating zones for the specific need of temperature control. One (preheating zone) controls the gas stream temperature upstream of the tapered element while the other (main heating zone) controls the temperature in the tapered element and the packed bed.

The top of the tapered element is fixed, so that the whole element can oscillate in a clamped-free mode. A detailed introduction of the oscillating mechanism of the

TEOM technique can be found elsewhere [Zhu, 2001a]. The natural oscillating frequency of the tapered element increases when the mass of the solid in the packed bed decreases, and *vice versa*. The system obtains accurate and time resolved values of mass change, by simply comparing the measured natural oscillating frequency to the one recorded at the beginning of the experiment. The system measures the mass change between two time points "0" and "1" obeying the following equation:

$$\Delta m = K_o \left[\frac{1}{f_1^2} - \frac{1}{f_0^2} \right] \tag{3-1}$$

where Δm is the mass change, K_o is the spring constant of the tapered element, f_o is the natural oscillating frequency at time "0", and f_1 is the natural oscillating frequency at time "1". This instrument provides excellent sensitivity, allowing mass changes as little as 1 μg to be detected.

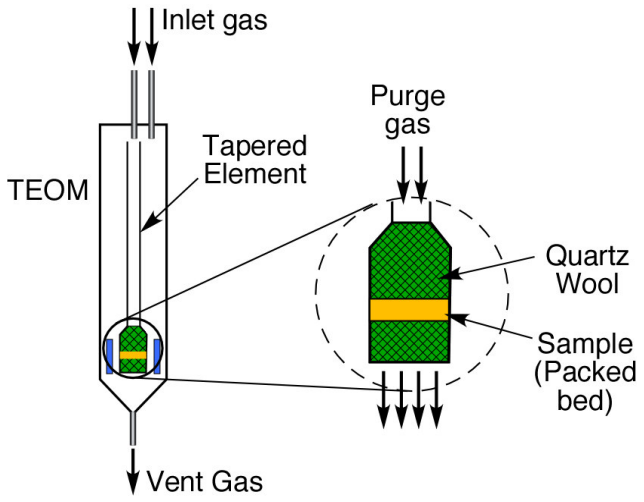

Figure 3-1. Schematic diagram of a TEOM.

3.2. Comparison with other Macroscopic Methods

To study adsorption/desorption and transport diffusion of gases/vapors in porous materials, the so-called macroscopic methods are usually employed. The aggregate properties (such as concentration, pressure, and mass) measured by macroscopic methods can be related to the diffusional time constant (and hence the diffusivity). It is possible that both the local concentration and flux can be directly measured in some macroscopic experiments and the diffusivity can therefore be directly calculated from the measured quantities. Such measurements are considered as direct methods of determining diffusivity. For the direct measurement, there's an excellent review in literature [Kärger, 1992]. The measurements more relevant to the TEOM technique (and more widely used) are the indirect measurements, which include batch methods (e.g., gravimetric and volumetric) and flow methods (e.g., chromatographic and zero length column). A comparison between TEOM and some important indirect macroscopic methods is presented here.

3.2.1. Comparison with Batch Methods

The most widely used batch method is the gravimetric method. By employing a sensitive gravimetric microbalance, this method monitors the weight change profile of a sample pile after the system is subjected to a step change of adsorbate

concentration in the bulk phase. In principle, the gravimetric microbalance technique has similar sensitivity as TEOM (~ 1 μg).

However, as a consequence of its unique measurement principle and well-designed gas flow pattern, the TEOM technique provides several significant advantages for the studies of adsorption/desorption kinetics over conventional microbalances, including:

- The carrier gas is forced to flow through the packed bed (in the tapered element) at a high flow rate (up to 2000 cc/min at STP conditions [Zhu, 2001a]). The forced convection around the particles significantly enhances the external mass and heat transfer rates for solid samples.

- The mass resolution of TEOM (indicated by its system standard deviation) is not significantly affected by the flow rate, temperature, and pressure. Such properties allow TEOM to be implemented under a relatively wide range of operating conditions.

- Very fast response (0.1 s) can be achieved in a TEOM and the short response time is important for measuring fast kinetics of adsorption/desorption.

A detailed comparison of the TEOM with the conventional microbalance technique is summarized in Table 3-1.

3.2.2. Comparison with Flow Methods

By passing carrier gas through the packed bed (chromatographic column) with a relatively high flow rate, the chromatographic method can more easily minimize the external mass and heat transfer limitations than a commonly used batch method does. However, the chromatographic measurement is often disguised by axial dispersion, especially when the intraparticle diffusion is rapid.

Table 3-1. Comparison of the TEOM and Conventional Microbalance Techniques [Zhu, 2001a]

	TEOM	Conventional Microbalance
Gas flow pattern	Flow through packed bed	Flow around and over sample pile
Gas flow impact	No impact up to 2000 sccm	Flow rates >100 sccm can cause noise
Mass resolution at high temperature	No reduction	Significant reduction
Response time (s)	0.1	10-30
Temperature (K)	298-973	298-1273
Pressure (Pa)	$0\text{-}6\times10^{6}$	$0\text{-}10^{5}$
Sensitivity (μg)	~ 1	~ 1
Static electricity impact	No	Yes
Buoyancy effect	No	Yes
Temperature programming	Yes[a]	Yes

[a] Updated from the manufacturer [R&P, 2000].

The zero length column (ZLC) method was developed to eliminate the drawbacks caused by axial dispersion in the conventional chromatographic method. To measure the intracrystalline diffusivity in zeolites, it appears that there are a few similarities between ZLC and TEOM techniques, including:

- Both methods use a small amount of sample (a thin layer in a packed bed) to minimize the bed-length effect. Consequently, the major limitation of the chromatographic method is eliminated.

- Both methods maintain a relatively high carrier gas flow rate to minimize the external mass and heat transfer resistances. Therefore, the major limitation of the batch/static methods is eliminated, as mentioned above.

- Both methods are capable of measuring relatively high diffusivity ($D/R^2 > 0.01\ s^{-1}$).

- To measure the desorption kinetics, the procedures are similar for both methods: initially the sample is equilibrated at a certain adsorbate partial pressure, and then desorbed in an inert gas with relatively high flow rate.

However, the ZLC technique requires the concentration of the effluent gas mixture to be accurately determined. At long desorption time, the measurement of the low concentration could become a critical issue. The sensitivity of the concentration measurement also depends on the types of adsorbate. In addition, ZLC method is mainly used in the linear isotherm region (Henry's Law range) [Zhu, 2001b], and the adsorption kinetics are not measurable by ZLC method.

For the TEOM technique, the key quantity measured is the mass change of the sample bed instead of the concentration of the effluent gas. Both the adsorption and desorption profiles can be monitored, and the measurement sensitivity is not

influenced by the adsorbate types. Additionally, the measurement can be easily performed under a relatively wide range of adsorbate partial pressures, both in the linear and non-linear isotherm regions.

3.3. Procedure

A schematic diagram of the experimental setup is shown in Figure 3-2 (a photograph of the apparatus is shown in Figure 3-3). The following procedure is employed to obtain the adsorption capacity and the rates of adsorption/desorption.

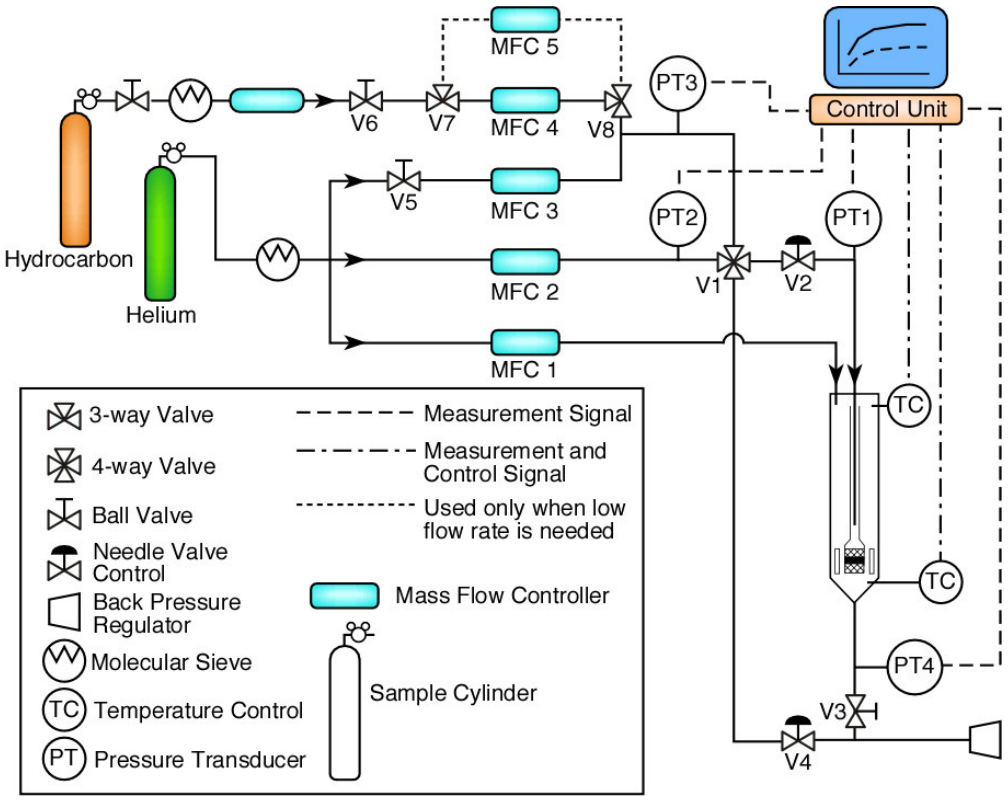

Figure 3-2. Schematic diagram of the experimental setup.

Prior to the experiments, zeolite crystals or mesoporous materials are packed firmly by quartz wool in the tapered element and the samples are heated at 10 K/min in flowing zero grade air at 100 sccm to the desired pre-treating temperature of 773 K, which is maintained for 5 h. Then the sample is cooled to the temperature of interest in a helium flow of 400 sccm. Another stream carrying hydrocarbon gas/vapor is directly connected with vent outlet without flowing through the tapered element.

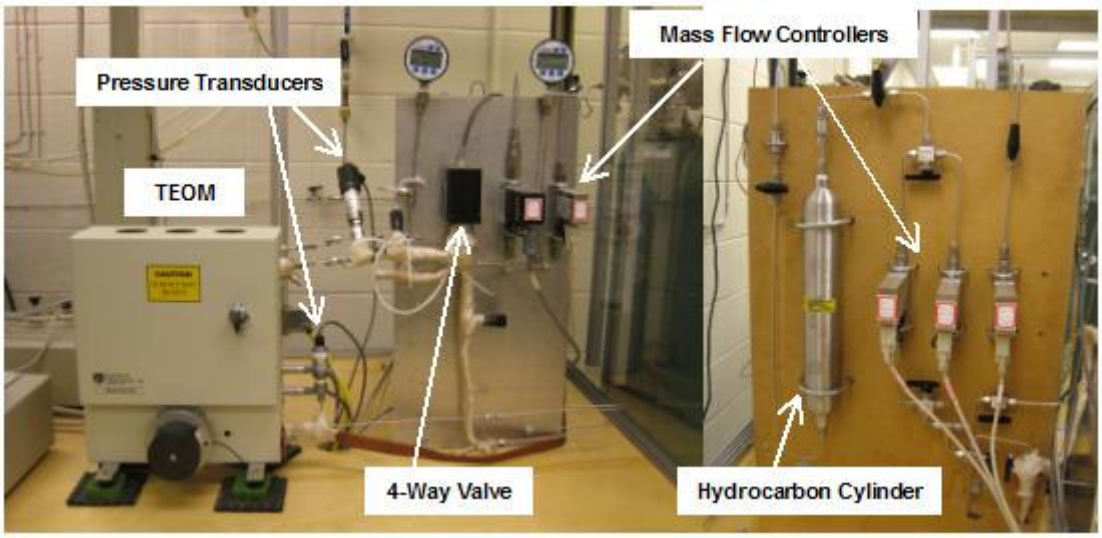

Figure 3-3. Experimental apparatus.

After a stable mass baseline is obtained, the 4-way injection valve (valve 1) is switched to make the stream containing hydrocarbon gas/vapor flow through the tapered element, while the pure helium stream is connected to the vent outlet without reaching the samples. It is very important to ensure that no pressure imbalance in the system occurs when value 1 is switched. The problem of pressure imbalance when

switching 4-way valve has been discussed in detail elsewhere [Zhu, 2001b; Lee, 2004]. The needle valves 2 and 4 are used to equalize the flow resistances downstream of the switching valve 1 such that the flow rate and the pressure drop in each carrier gas steam are not disturbed when the valve 1 is switched. The pressure transducers at the entrance and the exit of the tapered element are used to continuously monitor the pressure change. It is found that through careful tuning of the needle valves, the pressures are stable when the valve 1 is switched. Once the adsorption equilibrium has been attained after a certain period of time (usually 100 s), the valve 1 is switched back to its initial position and desorption commences. By this procedure, the total mass change is measured following a step change (either increase or decrease) in hydrocarbon concentration for a certain loading of catalysts.

In addition, the extent of mass change caused by the gas density variation in the void space within the tapered element and due to surface adsorption is determined in a blank run performed with non-porous quartz particles (identical in size and amount as the substrates of interest) at identical operating conditions. Blank runs have been demonstrated to be crucial to obtain the intrinsic mass change profiles using TEOM in other studies [Zhu, 1998; Chen, 1999; van Donk, 2001]. The intrinsic mass change due to adsorption is determined by subtracting the total mass change from the mass change due to gas density variation and surface adsorption, as shown in Figure 3-4a. Similar experiments were performed under different adsorbate partial pressures at the same temperature with quartz particles and zeolites (or mesoporous materials). The

intrinsic equilibrium adsorption isotherm was obtained through subtraction, as shown in Figure 3-4b.

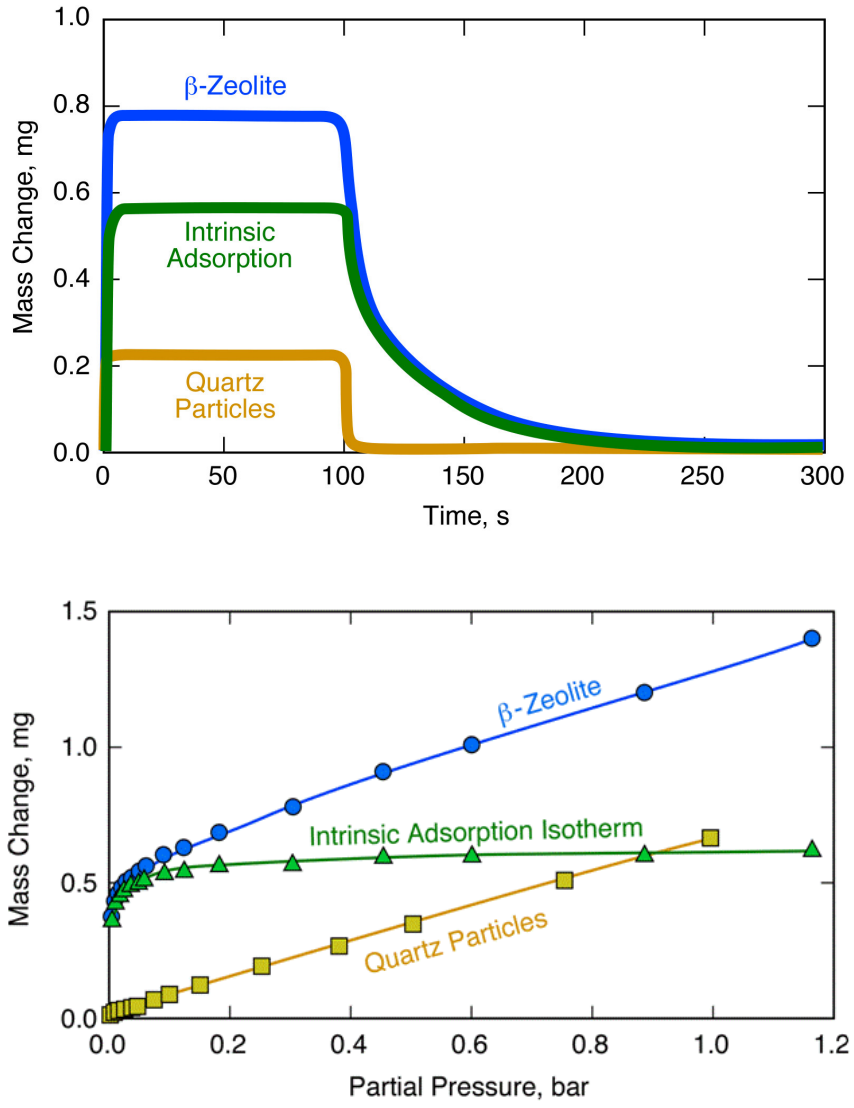

Figure 3-4. Procedures for the measurement of intrinsic adsorption/desorption profiles and intrinsic equilibrium adsorption isotherms: (a) Intrinsic adsorption/desorption profiles of isobutane on β-zeolite (T = 323 K; P_{iC4} = 0.304 bar; P = 1.4 bar; β-zeolite loading = 6.4 mg); (b) Intrinsic isobutane adsorption isotherm on β-zeolite (T = 323 K; P = 1-1.5 bar; β-zeolite loading = 6.4 mg).

The partial pressure of hydrocarbon is controlled by setting either the gas flow rates for the light hydrocarbon gases or the temperature of the gas saturator in the case of hydrocarbons that are liquids under ambient conditions (TMP, for example). Helium is used as both the purge and carrier gas. The gas flow rates are controlled by OMEGA FMA-700 series mass flow controllers. The carrier gas flow rates are each set at 400 sccm (unless otherwise mentioned) and the purge gas flow rate is maintained at 50 sccm. The pressures at the inlet and outlet of the tapered element are carefully monitored to avoid significant pressure drop ($\Delta P \leq 0.1$ bar) along the sample bed. The temperature of interest in the TEOM sample bed is in the range of 303-473 K. The pressures, temperatures, gas flow rates and mass changes of the sample are recorded continuously during the experiment. The time interval to measure the natural oscillating frequency is approximately 0.8 s and such a high time resolution makes TEOM capable of measuring relatively fast adsorption/desorption kinetics.

3.4. Gas Density Effect

When a step input of tracer is introduced in a typical TEOM experiment as mentioned above, there are two effects possibly contributing to the mass change of the tapered element, in addition to the intrinsic adsorption/desorption in the catalyst particles. One is the density shift caused by the switching between helium and the hydrocarbon gases, and the other is the adsorption on the surface of the tapered element and quartz wool packing. The latter contribution is usually negligible because

the surface adsorption is weaker, and the area for surface adsorption is relatively small in comparison with the internal area in the catalyst particles. To reliably obtain the intrinsic adsorption/desorption equilibria and rates, the extent of mass change caused by the gas density variation within the void space of the tapered element (and by the surface adsorption) must be properly accounted for.

The impact of the gas density variations on the mass change measurements by TEOM is often neglected or underestimated in previously reported studies. Alpay et al. [Alpay, 2003] used a TEOM to measure the uptake and desorption rates of *n*-hexane and *n*-heptane on fluid catalytic cracking (FCC) catalyst and silicalite adsorbent. In their work, the significant void space in the hollow tube of the tapered element above the packed bed and the void in the quartz wool packing section are neglected. No blank runs were performed to quantify the extent of mass gain due to density variations.

Lee et al. [Lee, 2004] used a TEOM to measure the rates of adsorption and desorption of *p*-xylene in FCC catalysts. In their experiments, blank runs were performed. Under the operating conditions investigated, it was found that the mass adsorbed was far greater than the mass change in the blank runs. But they treated the mass change in the blank runs as the mass change in the interparticle space without considering the void space in the hollow tube of the tapered element above the packed bed and the void in the quartz wool packing section.

In other similar reported TEOM investigations, blank runs were conducted and the results were properly explained [Hershkowitz, 1993; Zhu, 1998; van Donk, 2001]; however, the contributions of the mass change (in the blank run) from different parts of the tapered element were not systematically investigated and a deeper understanding of these contributions is essential to reliably design TEOM experiments and interpret the results.

In this work, blank runs using quartz particles are performed to account for the mass change due to gas/vapor density variations and surface adsorption. The operating conditions for the blank runs and for the corresponding adsorption/desorption experiments are identical. Ideally, the non-porous quartz particles used in the blank runs should have the same particle size as the zeolites (or the mesoporous materials), so that the void space and external surface area in the tapered element are identical.

Additionally, blanks runs with different loadings of quartz particles are performed under 224-TMP partial pressure 0-0.15 bar at 323 K, as shown in Figure 3-5. Under these conditions, the mass change due to gas density shift (that occurs when the pure helium carrier gas is replaced by the 224-TMP-laden helium gas phase) vs 224-TMP partial pressure shows good linearity for different sample sizes. The difference in mass change among these blank runs is negligible (especially when the total mass change is considered, as shown in Figure 3-5b), implying that the change in the void space of the sample holder (i.e., the bottom part of tapered element with relatively

large diameter, where the quartz wool and samples are packed) does not significantly affect the total void volume in the tapered element. In other words, the majority of the mass change (in a blank run) is due to the gas density shift within the narrow tube of the tapered element.

(a)

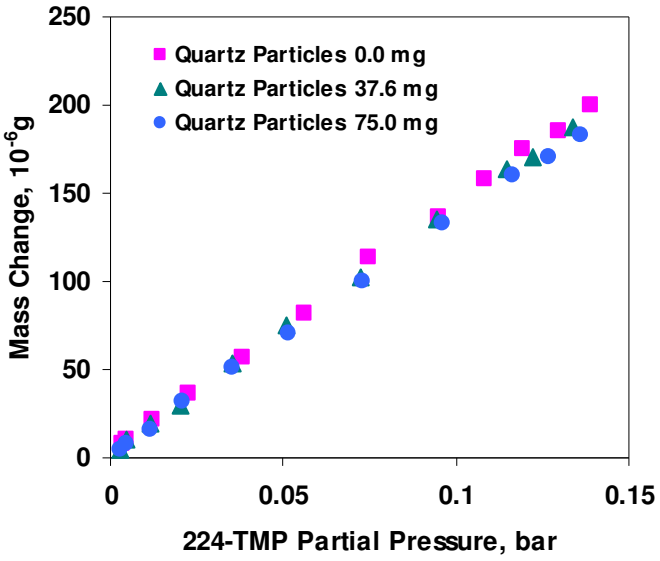

(b)

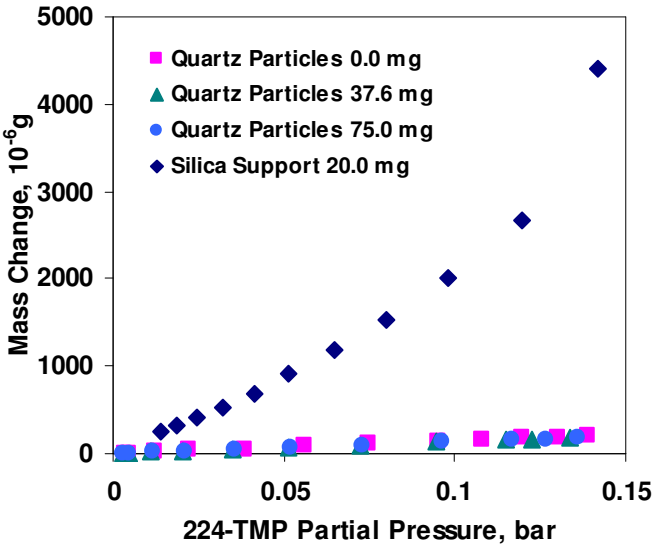

(c)

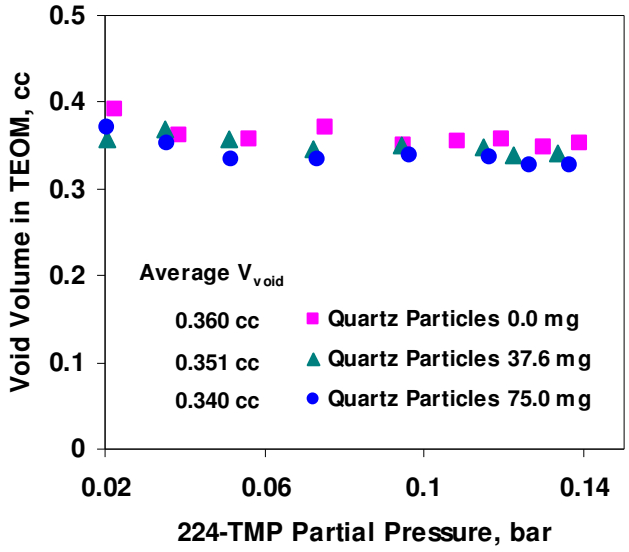

Figure 3-5. The impact of quartz particle loading on the measured mass change in blank runs, and the estimated void volume in the corresponding experiments (T = 323 K, P = 1-1.3 bar, carrier gas He flow rate = 200 sccm, quartz particles size is 50-53 µm): (a) mass change due to gas density change at various 224-TMP partial pressures; (b) total mass change (adsorbent is 20.0 mg silica support Davicat SI 1301) and mass change due to gas density change at various 224-TMP partial pressures; (c) the estimated void volume in the corresponding blank runs.

Assuming that the mass change due to surface adsorption is negligible, and that the vapor phase follows ideal gas behavior, the void volume in the tapered element can be estimated by the equation:

$$V_{void} = \frac{\Delta M \times R_g T}{P_{TMP}(Mw_{TMP} - Mw_{He})} \tag{3-2}$$

where ΔM is the mass change measured at the equilibrium state in a blank run, R_g is gas constant, T is the temperature, P_{TMP} is the partial pressure of 224-TMP, and Mw_{TMP} and Mw_{He} are the molecular weights of 224-TMP and helium, respectively.

The estimated void volumes in the corresponding blank runs are shown in Figure 3-5c. As expected, the void volume decreases at higher loading of quartz particles. The estimated total void volume is in the range of 0.340-0.360 cc at quartz particle loadings of 0-75 mg.

The approximate void volume of the sample bed was also estimated. Assuming that the packing void fraction is 40% and given that the total volume of the packed bed space is typically in the range of 0.01-0.08 cc, it follows that the void space in the packed bed is 0.004-0.032 cc. The percentage of the void space in the packed bed relative to the total void volume is therefore in the range of 1-10%, confirming that the main contribution of the gas density shift comes from the void space in the narrow tube above the packed bed.

The ratios of mass change due to the gas density shift and surface adsorption to the total mass change are shown in Figure 3-6 for a wide range of operating conditions. It can be seen that the mass change caused by gas density shift and surface adsorption is significant and could account for 50% or more of the total mass change, especially at low levels of adsorption (i.e. at 398 K and partial pressure lower than 0.03 bar). The ratio increases with temperature, and decreases with 224-TMP partial pressure. This is explained by the fact that mass change due to the density shift is less sensitive to pressure and temperature than that due to the intrinsic adsorption.

Clearly, the measurement of intrinsic equilibrium isotherms could be subject to significant errors if density shift effects are not quantitatively accounted for. Such

errors can propagate in the later analyses (e.g., adsorption energy calculation and uptake curve fitting).

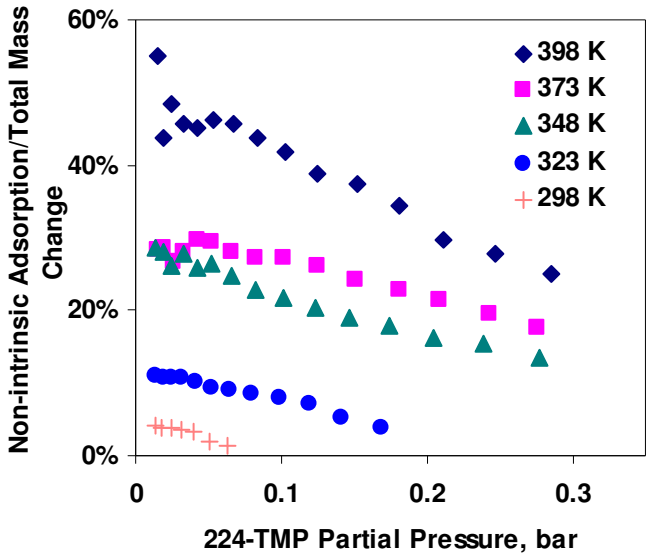

Figure 3-6. TEOM mass change contributions from gas density shift and surface adsorption effects during 224-TMP adsorption in 20.0 mg Davicat SI 1301 silica support.

References

Alpay, E., Chadwick, D., Kershenbaum, L. S., Barrie, P. J., Sivadinarayana, C., Gladden, L. F., (2003). TEOM analysis of the equilibria and kinetics of *n*-hexane and *n*-heptane adsorption on FCC catalyst/silicalite. Chemical Engineering Science 58, 2777-2784.

Barrie, P. J., Lee, C. K., Gladden, L. F., (2004). Adsorption and desorption kinetics of hydrocarbons in FCC catalysts studied using a tapered element oscillating microbalance (TEOM). Part 2: numerical simulations. Chemical Engineering Science 59, 1139-1151.

Chen, D., Gronvold, A., Rebo, H. P., Moljord, K., Holmen, A., (1996). Catalyst deactivation studied by conventional and oscillating microbalance reactors. Applied Catalysis A: General 137, L1-L8.

Chen, D., Rebo, H. P., Moljord, K., Holmen, A., (1997). Influence of coke deposition on selectivity in zeolite catalysis. Industrial & Engineering Chemistry Research 36, 3473-3479.

Chen, D., Rebo, H. P., Moljord, K., Holmen, A., (1999). Methanol conversion to light olefins over SAPO-34. Sorption, diffusion, and catalytic reactions. Industrial & Engineering Chemistry Research 38, 4241-4249.

Hershkowitz, F., Madiara, P. D., (1993). Simultaneous measurement of adsorption, reaction, and coke using a pulsed microbalance reactor. Industrial & Engineering Chemistry Research 32, 2969-2974.

Kärger, J., Ruthven, D. M., (1992) Diffusion in zeolites and other microporous solids, Wiley: New York.

Lee, C. K., Ashtekar, S., Gladden, L. F., Barrie, P. J., (2004). Adsorption and desorption kinetics of hydrocarbons in FCC catalysts studied using a tapered element oscillating microbalance (TEOM). Part 1: experimental measurements. Chemical Engineering Science 59, 1131-1138.

Liu, K., Fung, S. C., Ho, T. C., Rumschitzki, D. S., (1997). Kinetics of catalyst coking in heptane reforming over Pt-Re/Al_2O_3. Industrial & Engineering Chemistry Research 36, 3264-3274.

Patashnick, H., Rupprecht, G., (1980). New real-time monitoring instrument for suspended particulate mass concentration - TEOM. Abstracts of Papers of the American Chemical Society 179, 51-Petr.

R&P, (2000) Operating manual: TEOM series 1500 pulse mass analyzer. Rupprecht & Patashnick Co., Inc.: Albany, NY.

van Donk, S., Broersma, A., Gijzeman, O. L. J., van Bokhoven, J. A., Bitter, J. H., de Jong, K. P., (2001). Combined diffusion, adsorption, and reaction studies of *n*-hexane hydroisomerization over Pt/H-mordenite in an oscillating microbalance. Journal of Catalysis 204, 272-280.

Wang, J. C. F., Patashnick, H., Rupprecht, G., (1980). A new real-time isokinetic dust mass monitoring system. Journal of the Air Pollution Control Association 30, 1018-1021.

Zhu, W., Adsorption and diffusion in microporous materials: An experimental study with the TEOM, Ph.D Dissertation, Delft University of Technology, 2001a.

Zhu, W., Kapteijn, F., Moulijn, J. A., (2001b). Diffusion of linear and branched C_6 alkanes in silicalite-1 studied by the tapered element oscillating microbalance. Microporous and Mesoporous Materials 47, 157-171.

Zhu, W., van de Graaf, J. M., van den Broeke, L. J. P., Kapteijn, F., Moulijn, J. A., (1998). TEOM: A unique technique for measuring adsorption properties. Light alkanes in silicalite-1. Industrial & Engineering Chemistry Research 37, 1934-1942.

Chapter 4 Equilibrium Adsorption Isotherms of Model Alkylation Compounds on Microporous and Mesoporous Catalysts

In general, it is necessary to measure the equilibrium adsorption isotherms of pure compounds for investigations of adsorption/desorption equilibria and kinetics of pure components and multicomponent systems. The information (e.g., adsorption affinity, mechanism, and saturation capacity) obtained from the equilibrium adsorption isotherms helps us to understand the adsorption and mass transport phenomena at a macroscopic scale.

In this dissertation, a TEOM is employed to investigate the equilibrium adsorption isotherms of model compounds of relevance in 1-butene+isobutane alkylation on zeolites and other mesoporous materials. The detailed methodology was introduced in Chapter 3.

At the beginning of this chapter, the empirical models used in this work for describing the equilibrium adsorption isotherms are introduced. Then, the results of physical characterization for the zeolites and mesoporous materials are shown. Experimental data and empirical correlation of the equilibrium adsorption isotherms of propane, isobutane, *n*-butane, and CO_2 on β- and USY-zeolites are presented. The results of a Grand Canonical Monte Carlo (GCMC) molecular simulation are

incorporated in order to bridge the gap between the molecular-level structure and observable macroscopic properties. Finally, the experimental data and corresponding model correlation of the equilibrium adsorption isotherms of 224-TMP on β-zeolite, mesoporous silica supports, and MCM-41 are presented.

4.1. Mathematical Modeling of Equilibrium Adsorption Isotherms

For microporous materials, such as zeolites, the Langmuir model usually provides reasonably good description of the measured equilibrium adsorption isotherms. This model is developed on the basis of the following assumptions: (a) there is no surface heterogeneity; (b) only localized adsorption occurs, and there is no interaction between the adsorbed molecules; and (c) each site can be occupied by only one molecule. The Langmuir model is defined as:

$$q = \frac{q_s bp}{1 + bp} \tag{4-1}$$

where q is the concentration in the adsorbed phase, q_s is the saturation concentration in the adsorbed phase, b is Langmuir equilibrium constant, and p is the partial pressure of adsorbate.

When there exists two different (homogeneous) types of adsorption sites in the microporous materials, the dual-site Langmuir model usually leads to a better description [Zhu, 1998; Barcia, 2006]. The dual-site Langmuir model is defined as:

$$q = \frac{q_{s1} b_1 p}{1 + b_1 p} + \frac{q_{s2} b_2 p}{1 + b_2 p} \tag{4-2}$$

where q_{s1} and q_{s2} are the saturation concentrations in each type of adsorption site, b_1 and b_2 are Langmuir equilibrium constants for each sorption site.

In mesoporous materials, multi-layer adsorption takes place and liquid starts to form at sufficiently high pressure due to capillary condensation. Brunauer model was demonstrated to suffice to describe capillary condensation and finite pore volume filling in the mesoporous adsorbents, and it is defined as [Duong, 1998]:

$$\frac{q}{q_m} = \frac{Cx}{1-x} \frac{1 + (ng/2 - n)x^{n-1} - (ng - n + 1)x^n + (ng/2)x^{n+1}}{1 + (C-1)x + (Cg/2 - C)x^n - (Cg/2)x^{n+1}} \tag{4-3}$$

where,

$$g = \exp(Q / R_g T) \tag{4-4}$$

$$x = p / p_0 \tag{4-5}$$

Q is the heat of adsorption, p_0 is the reference pressure, q_m is the amount of gas adsorbed to fill a monolayer, C is the constant that indicates the interaction of adsorbate and adsorbent at low pressure, and n is the maximum number of layer in one wall.

A numerical routine ("fminsearch" function in Matlab) was used to search for the equilibrium isotherm parameters that minimize the value of the objective function given below:

$$S_{TG} = \sum_{i=1}^{n} \left(m_i^{\exp} - m_i^{calc} \right)^2 \tag{4-6}$$

where $m^{\exp}$ is the adsorbed amount that is measured in the experiments, m^{cal} is the adsorbed amount that is calculated with a given set of parameters. Subscript i denotes the discrete value corresponding to each partial pressure, and n is the total number of discrete data points (i.e., partial pressures) employed in the evaluation.

4.2. Characterization of Adsorbents and Adsorbates

4.2.1. Zeolites

The β-zeolite (SMR 5-9858-01062, Si/Al ratio = 13.3) and USY-zeolite (SMR 5-9858-01061, Si/Al ratio = 2.9) were supplied by GRACE Davison. Table 4-1 summarizes the key properties of the samples.

SEM images of the samples were taken in the Microscopy Laboratory at the University of Kansas (shown in Figure 4-1 and 4-2). The results show that both types of materials have very small crystal size (average crystal diameter < 1 μm). The crystals tend to form small particles (diameter 4-30 μm) through self-aggregation.

N_2 BET area and pore volume characterizations of zeolites were performed at DuPont by a Micromeritics ASAP 2405N automatic sorption analyzer and the results for β-zeolite are shown in Figure 4-3 (USY-zeolite shows similar pore volume distribution). The surface areas in micro/zeolitic pores (pore diameter < 2 nm) account for 89.5% and 91.7% of the total surface areas for β-zeolite and USY-zeolite, respectively. The pore volumes in mesopores/macropores (pore diameter > 2 nm) contribute to 22.3% and 19.6% of the total pore volumes for β-zeolite and USY-zeolite, respectively. In the mesopores/macropores range, it is found that 42.7% and 54.6% of the pore volumes come from 2-5 nm pore size region for β-zeolite and USY-zeolite, respectively, implying that the mesopores/macropores have relatively small average diameter through aggregation.

Table 4-1. Properties of β-zeolite and USY-zeolite

Properties	**β-zeolite**	**USY-zeolite**
Si/Al ratio[a] (mol/mol)	13.3	2.9
Average crystal size[a] (μm)	< 1	< 1
Agglomerate size, intergrown[a] (μm)	4-30	4-30
Total surface area[b] (m^2/g)	605.9	665.2
Surface area with pores < 2 nm[b] (m^2/g)	542.0	610.3
Surface area with pores > 2 nm[b] (m^2/g)	63.9	54.9
Total pore volume[b] (cc/g)	0.286	0.312
Pore volume with pores < 2 nm[b] (cc/g)	0.222	0.251
Pore volume with pores > 2 nm[b] (cc/g)	0.064	0.061
Acidity[c] (μmole NH_3/g catalyst)	291.2	466.0

[a] Provide by manufacturer (GRACE Davison)

[b] Provide by DuPont using BET

[c] Provide by ConocoPhillips using TPD

(a)

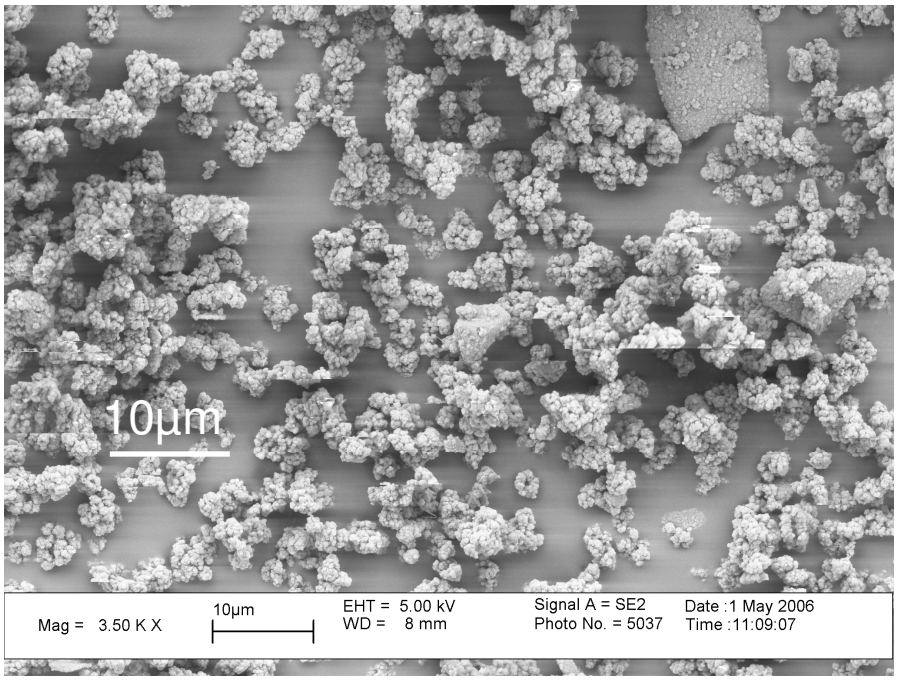

(b)

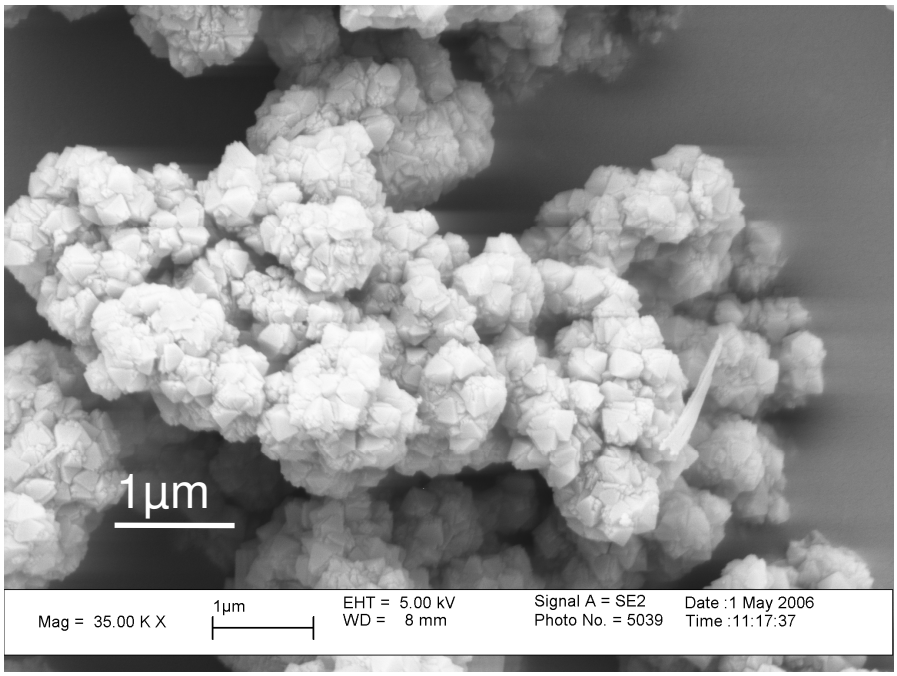

Figure 4-1. SEM images of β-zeolite.

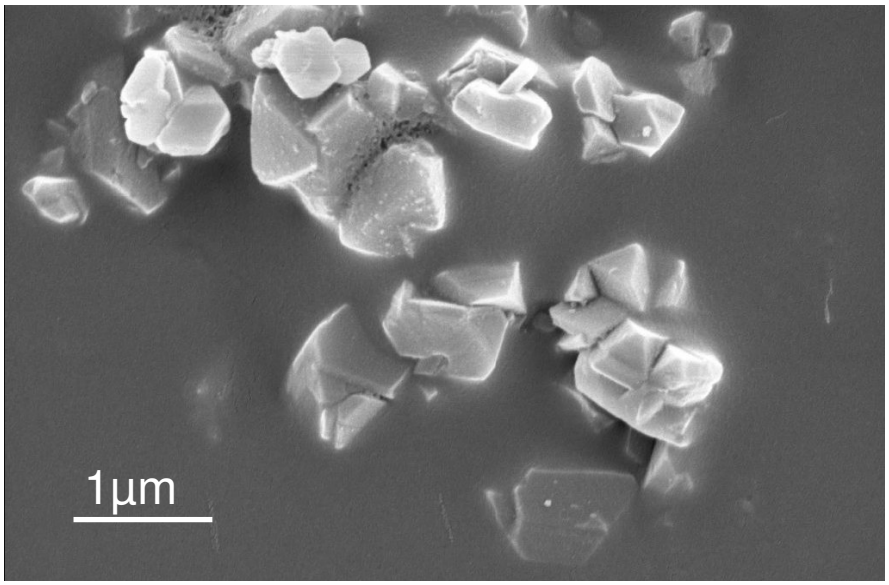

Figure 4-2. SEM image of USY-zeolite.

Accordingly, zeolites in this study are treated as particles with bimodal pore size distribution. In addition to the intracrystalline diffusion resistance, the extracrystalline mass transfer resistances in the self-aggregated particles and in the packed bed (similar to the self-aggregation) are considered.

To determine the acidity values of β-zeolite and USY-zeolite, the ammonia temperature-programmed desorption (TPD) experiments were conducted at ConocoPhillips using a Micromeritics ASAP 2910 sorption analyzer equipped with a thermal conductivity detector (TCD), and the results are listed in Table 4-1.

Experiments of 224-TMP adsorption/desorption in both acidic β-zeolite and Na-form β-zeolite were conducted under identical conditions in order to better understand the effect of acidity on the transient adsorption/desorption profiles (see

Section 5.3). A cation exchange was performed to convert the acidic β-zeolite to its sodium form. First, approximately 0.2 g of acidic β-zeolite sample was contacted with 5 cc aqueous solution containing 0.6 g of NH_4NO_3•$9H_20$ at ambient temperature for 12 h with stirring. The mixture was then decanted and washed with 5 cc water. Then another cation exchange was performed by contacting sample with 10 cc aqueous solution containing 1 g of NaCl at ambient temperature for days with stirring. Finally, the mixture was filtered, and the solid was dried in vacuum (0.1 torr) at 333 K for 5 h, and then at 353 K for 6 h.

A DuPont-Q500 thermal gravimetric analyzer (TGA) in the Department of Pharmaceutical Chemistry at University of Kansas was used to measure the non-structural water content in β-zeolite. The sample was heated at 10 K/min to 473 K in a flow of argon and it is found that the water content in β-zeolite is 10-13 wt%, as shown in Figure 4-4. Similar measurements were performed by Platon et al. [Platon, 2005] and they observed that the water content in two β-zeolite samples is in the range of 8-10 wt%, when the samples were heated at 10 K/min to 523 K in a purging argon environment.

Such results indicate that zeolite samples contain a significant amount of non-structural water. Therefore, in the adsorption/desorption experiments, the adsorbent is weighed after being dried at 383 K for 5 h in an oven with a purging argon environment. All the reported adsorbent weights in this study are on a dry weight basis.

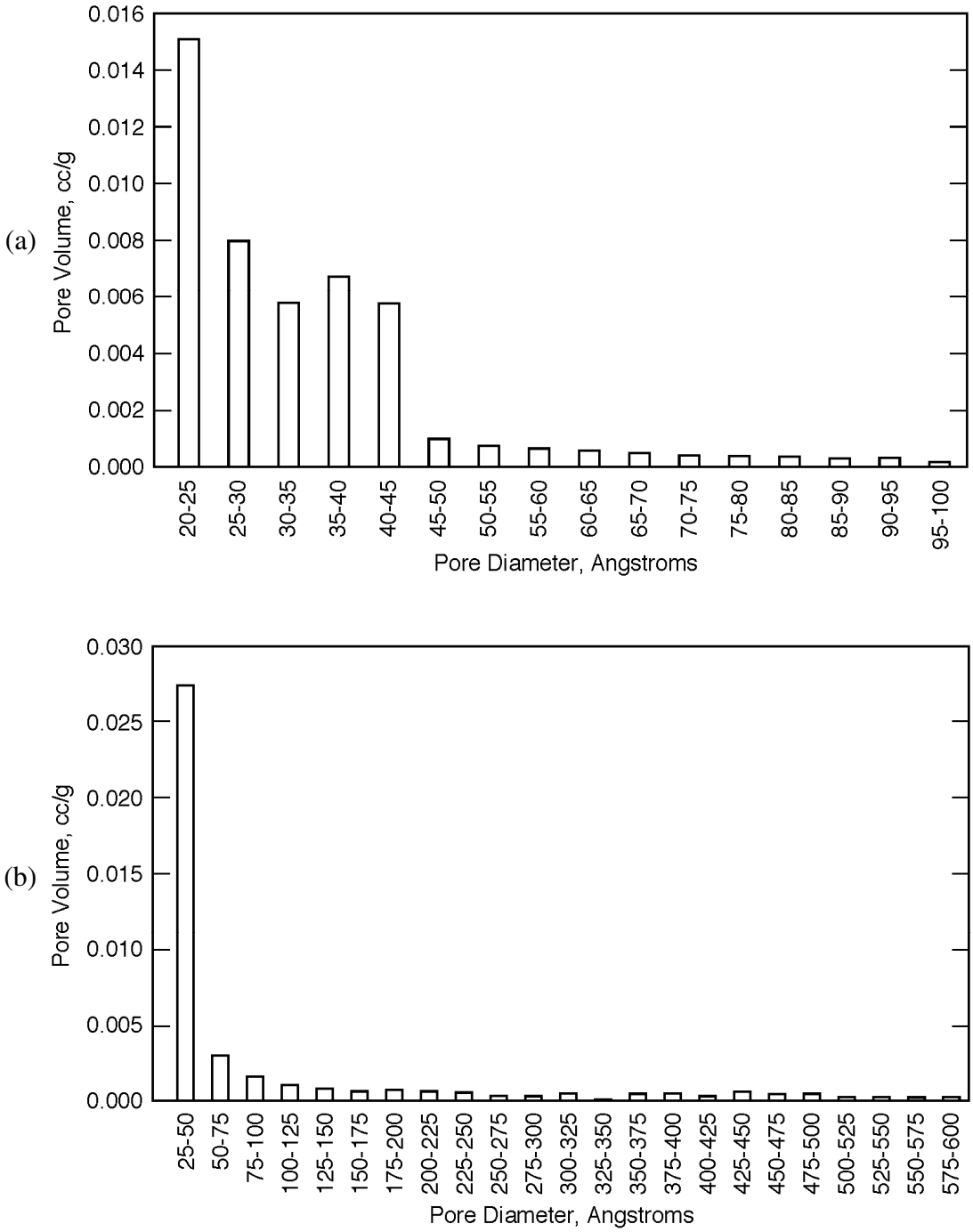

Figure 4-3. Pore volume distribution of β-zeolite: (a) pore sizes 2-10 nm; (b) pore sizes > 2.5 nm.

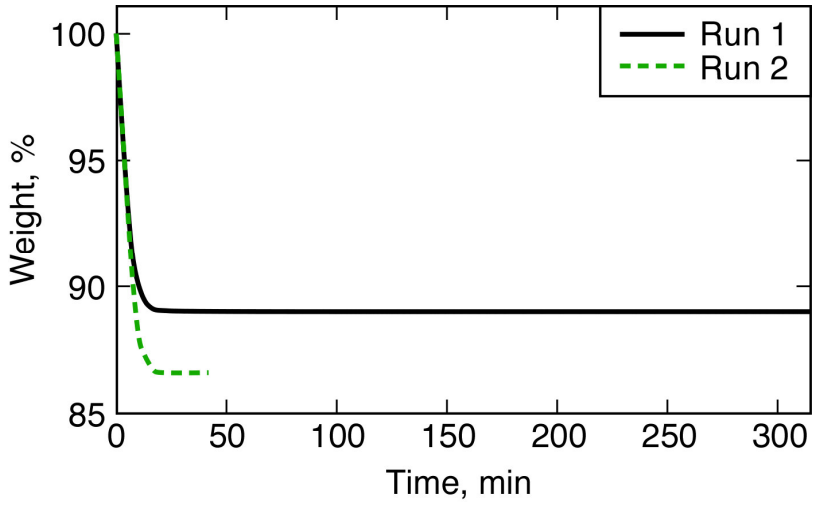

Figure 4-4. The weight change profile of β-zeolite in TGA (heating method: ramp temperature at 10 K/min to 473 K, then maintain isothermal till the end of the experiment).

4.2.2. Mesoporous Materials

Silica supports Davicat SI 1301 and 1401 were supplied by GRACE Davison, and the MCM-41 sample was purchased from Sigma-Aldrich. Table 4-2 summarizes the characterization of the samples. These data were provided by the corresponding manufacturers.

Table 4-2. Properties of the Mesoporous Materials Investigated in this Work

Sample	**Davicat SI 1301**	**Davicat SI 1401**	**MCM-41**
Mean pore diameter (nm)	14	2.3	2.8
Particle size (μm)	35-70	35-70	N/A
Total surface area (m^2/g)	312	750	970
Total pore volume (cc/g)	1.2	0.4	N/A
Si/Al ratio (mol/mol)	N/A	N/A	40

It can be seen that the total pore volume and the pore diameter of SI 1301 are much higher than those of SI 1401. Note that the pore size of SI 1401 is fairly close to those of the large pore zeolites (e.g., β- and USY-zeolites). Hence, one may expect SI 1401 to exhibit similar adsorption/desorption and transport properties as the large pore zeolites. However, the zeolites show tunable acidities which could also affect the adsorption/desorption equilibria and dynamics.

4.2.3. Chemicals

Ultra high purity helium (purity > 99.999%, Airgas) is used as carrier gas and purge gas. The gas adsorbates employed are research grade (isobutane purity > 99.995%, *n*-butane purity > 99.98%, and propane purity > 99.993%) from Matheson Tri-gas. The liquid adsorbate 224-TMP was purchased from Sigma-Aldrich with 99.8% purity.

4.3. Equilibrium Adsorption Isotherms of *n*-Butane, Isobutane, and Propane on β-zeolite and USY-zeolite

Experiments of *n*-butane, isobutane, and propane adsorption/desorption on β-zeolite and USY-zeolite were performed under adsorbate partial pressure 0-1.2 bar at temperature 303-398 K, and the corresponding equilibrium adsorption isotherms (the amounts adsorbed are normalized to the weight of adsorbent) are shown in Figure 4-5, 4-6, and 4-7. In this study, *n*-butane and propane were used as proxies for 1-butene

and propene, respectively, to avoid oligomerization of olefins in the zeolites [Chen, 1999; Platon, 2005].

(a)

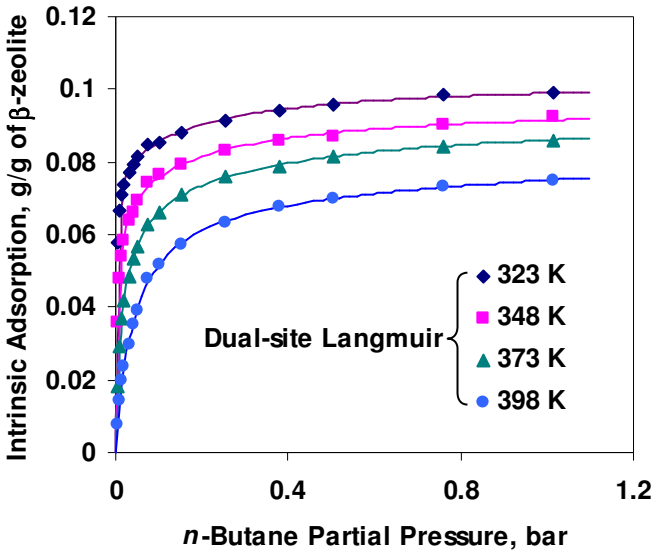

(b)

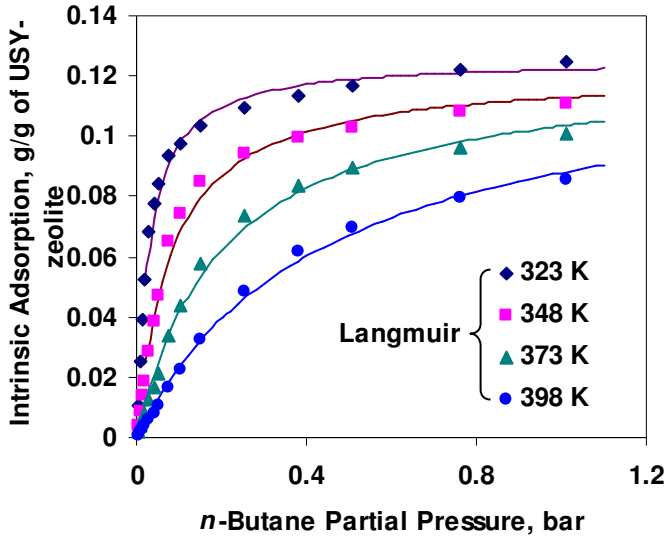

Figure 4-5. Intrinsic adsorption equilibrium isotherms of *n*-butane in zeolites: (a) in β-zeolite; (b) in USY-zeolite.

(a)

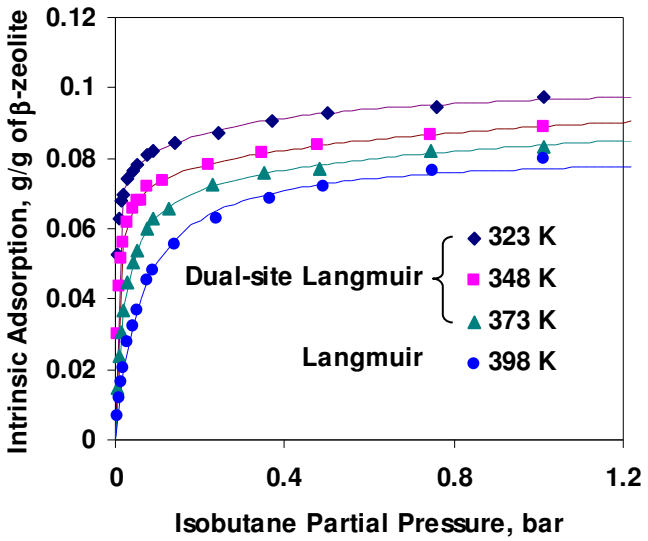

(b)

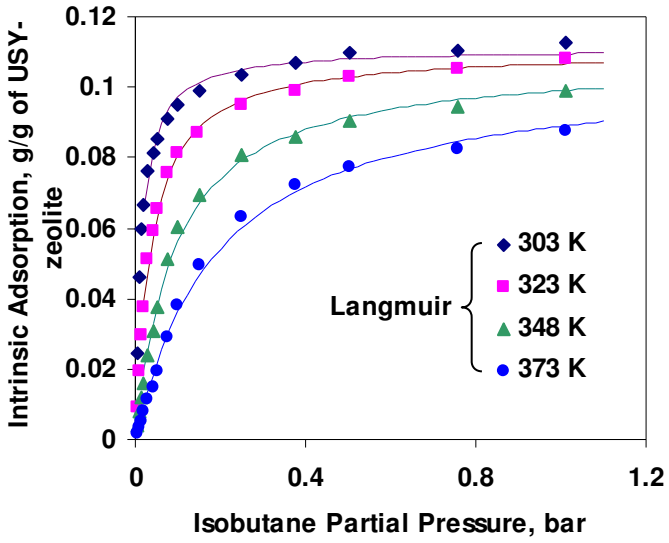

Figure 4-6. Intrinsic equilibrium adsorption isotherms of isobutane in zeolites: (a) in β-zeolite; (b) in USY-zeolite.

(a)

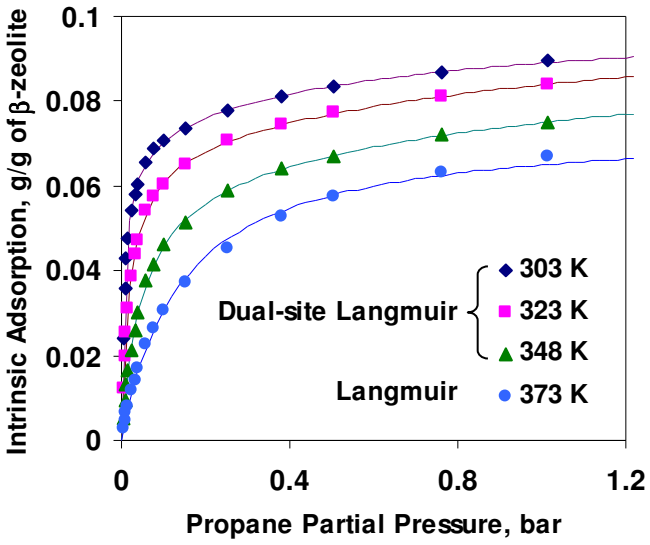

(b)

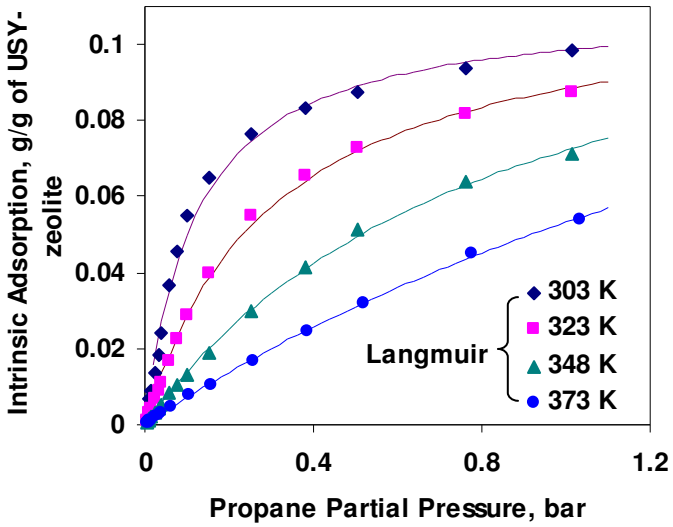

Figure 4-7. Intrinsic equilibrium adsorption isotherms of propane in zeolites: (a) in β-zeolite; (b) in USY-zeolite.

Under the operating conditions studied, the equilibrium adsorption isotherms of *n*-butane, isobutane, and propane in both β-zeolite and USY-zeolite exhibit type I shape

in the Brunauer classification. At sufficiently low partial pressures, the isotherms are in the linear region (Henry's law region), which is also confirmed by nearly identical adsorption and desorption rates in the corresponding adsorption/desorption profiles. At sufficiently high partial pressures, the equilibrium adsorption isotherms approach saturation. This type of equilibrium isotherm is typical for adsorption in microporous materials (e.g., zeolites and charcoals), and a monolayer coverage is postulated at equilibrium [Duong, 1998].

There are a few empirical models that are commonly used to fit type I equilibrium adsorption isotherms, including Langmuir, Toth, and Unilan models. Among these, the simplest and most widely used one is the Langmuir model. In the present study, it is found that either Langmuir or dual-site Langmuir model leads to good descriptions for the equilibrium adsorption isotherms of C_3-C_4 alkanes in β- and USY-zeolites. In addition, both the Langmuir and dual-site Langmuir models provide somewhat simplified and straightforward physical interpretations for the adsorption phenomena observed.

It is found that the equilibrium adsorption isotherms of *n*-butane, isobutane, and propane in USY-zeolite are fitted well by Langmuir model. However, simple Langmuir model does not provide good descriptions for the equilibrium isotherms of these light alkanes in β-zeolite at relatively low temperatures. Instead, a good agreement with the experimental results is achieved by using dual-site Langmuir model, suggesting the existence of two types of adsorption sites in β-zeolite. Dual-site

Langmuir models have been widely used by other researchers to account for the adsorption on two distinctly different adsorption sites. For example, Zhu and his coworkers [Zhu, 1998] found that the dual-site Langmuir model provides excellent description of the equilibrium adsorption isotherms of propane, isobutane, and *n*-butane in silicalite-1 at low temperatures (< 373 K); Barcia et al. [Barcia, 2006] demonstrated that the dual-site Langmuir model is suitable for the correlation of equilibrium adsorption isotherms of hexane isomers in β-zeolite pellets.

The fitted results of the equilibrium adsorption isotherms of *n*-butane, isobutane, and propane in β-zeolite and USY-zeolite are shown in Table 4-3. It is found that the saturation capacities of these systems are in the range of 0.07-0.14 g/g of adsorbent. Such values are in good agreement with the published data on the similar systems. For example, the measured saturation capacities of isobutane in large-pore 13X zeolite by the static volumetric method are in the range of 0.08-0.11 g/g of adsorbent at 298-373 K [Hyun, 1982]; and the measured saturation capacities of propane in 13X zeolite are in the range of 0.09-0.10 g/g of adsorbent at 279-308 K [Costa, 1991]. The saturation capacity of USY-zeolite is 5-30% greater than that of β-zeolite, and this finding is in reasonably good agreement with the BET characterization results (i.e., the total surface area of USY-zeolite is approximately 10% higher than that of β-zeolite). Under the same conditions, the Langmuir constant on β-zeolite is greater than that on USY-zeolite, implying that pore size possibly has a significant effect on the adsorption affinity in the microporous materials. In this study, the zeolite pore

sizes are comparable to the adsorbate molecule sizes (the kinetic diameters of *n*-butane, isobutane, and propane are in the range of 0.4-0.5 nm, while the pore diameters of β-zeolite and USY-zeolite are in the range of 0.5-1.2 nm). Under such conditions, adsorption occurs by attractive force from the pore wall [Suzuki, 1990].

In the investigation of equilibrium adsorption isotherms of light alkanes (including *n*-butane, isobutane, and propane) in silicalite-1, Zhu et al. [Zhu, 1998] found that the saturation capacities of silicalite-1 decrease when temperature increases. However, such a trend was not observed in our study. Instead, the results of our work are in good agreement with the findings by Lee and coworkers [Lee, 2004]. They found that the adsorption saturation capacities of hydrocarbons in Y-zeolite are essentially independent of temperature in the 373-473 K range.

The adsorption affinity of the butane isomers is much stronger than that of propane under the same conditions, indicating that the molecule size has a significant impact on the adsorption affinity. The effect is confirmed to be significant in later analysis, where the Langmuir constants of CO_2, propane, butane isomers, and 224-TMP in β-zeolite are compared together.

In addition, the influence of branching is studied by comparing the fitted parameters of equilibrium isotherms between the butane isomers. The adsorption affinity of *n*-butane is greater than that of isobutane. A similar trend was observed by other researchers. For example, Barcia et al. [Barcia, 2006] found that *n*-hexane has the strongest adsorption strength in β-zeolite among hexane isomers, followed by

monobranched and dibranched isomers. Such results show that a larger kinetic diameter (the kinetic diameter of isobutane is larger than that of *n*-butane) does not necessarily correspond to a higher adsorption affinity under the same conditions.

Table 4-3. Summary of the Parameters Obtained from the Analysis of Equilibrium Adsorption Isotherms

Adsorbate	Catalyst	T (K)	q_{max1} (g/g)	b_1 (1/bar)	q_{max2} (g/g)	b_2 (1/bar)	$-\Delta H_{ads1}$ (kJ/mol)	$-\Delta H_{ads2}$ (kJ/mol)
propane	USY-zeolite	303	0.111	8.3			37±4	
		323	0.115	3.3				
		348	0.136	1.1				
isobutane	USY-zeolite	303	0.111	70.9			35±4	
		323	0.111	27.0				
		348	0.108	10.9				
		373	0.106	5.2				
n-butane	USY-zeolite	303	0.127	102.3			39±4	
		323	0.126	34.3				
		348	0.122	12.4				
		373	0.124	5.1				
		398	0.127	2.3				
propane	β-zeolite	303	0.071	128.2	0.029	1.8	38±4	19±4
		323	0.069	51.5	0.035	0.8		
		348	0.064	21.3	0.035	0.7		
		373	0.074	7.0				
isobutane	β-zeolite	323	0.077	444.9	0.025	3.6	47±4	33±4
		348	0.075	143.4	0.027	1.1		
		373	0.075	48.5	0.026	0.7		
		398	0.082	16.2				
n-butane	β-zeolite	323	0.079	498.5	0.024	5.0	44±4	39±4
		348	0.072	182.3	0.024	4.4		
		373	0.070	66.8	0.023	2.7		
		398	0.072	23.6	0.023	0.3		
224-TMP	β-zeolite	348	0.096	308924	0.017	560.5	86±4	73±4
		373	0.084	101025	0.022	444.3		
		398	0.074	26229	0.027	221.5		
		473	0.090	144.1				
224-TMP	Silica 1401	298	0.159	936.2			52±4	
		323	0.153	163.5				
		348	0.153	43.1				
		373	0.131	13.9				

Heat of adsorption is calculated by correlating the Langmuir constants with the Arrhenius equation. In this study, the heat of adsorption possesses noticeable uncertainty (as large as ±4 kJ/mol) and similar uncertainties were observed by Lee and his coworkers [Lee, 2004]. These results indicate that TEOM is probably not suitable for identifying the subtle differences in the adsorption heat among alkane isomers or alkanes with very close carbon numbers, when very small amount of sample is used in the experiments to minimize the impact of the concentration gradient down the packed bed (see Chapter 5). To eliminate this limitation, larger amounts of sample should be used to minimize the impact of gas density change and hence minimize the systematic errors (as discussed in Chapter 3). However, in this study, the main goal is to investigate the adsorption/desorption rates of hydrocarbons in zeolites and mesoporous materials, and it requires that very small sample sizes should be used.

To better understand the relationship between the molecular-level structure and observable macroscopic properties of the adsorption systems studied in this work, a Grand Canonical Monte Carlo (GCMC) simulation program was developed in the Department of Chemistry at the University of Kansas [Houndonougbo, 2008]. In this study, four unit cells were used and the simulation box dimension for β-zeolite and USY-zeolite were a = 2.532 nm, b = 2.532 nm, and c = 2.641 nm.

A comparison of the equilibrium isotherm obtained by GCMC simulation with experimental equilibrium isotherm obtained from TEOM is shown in Figure 4-8. It

can be seen that a reasonably good fit is achieved for the equilibrium adsorption isotherm of isobutane in β-zeolite at 348 K. The simulation extends the isobutane pressure to a much wider range (10^{-5}-10^{3} bar). The equilibrium value at 100 bar is only slightly greater than that at 1 bar, indicating that the pores are already filled up by isobutane at 1 bar. The bulk pressure could possibly affect the pore filling, resulting in tighter packing in the micropores under higher pressures. Such analysis helps us to understand the adsorption/desorption of isobutane under the real conditions of the alkylation reactions (the solid acid alkylation is usually carried out in the liquid phase, but the measurement by the TEOM technique is limited in the gas phase).

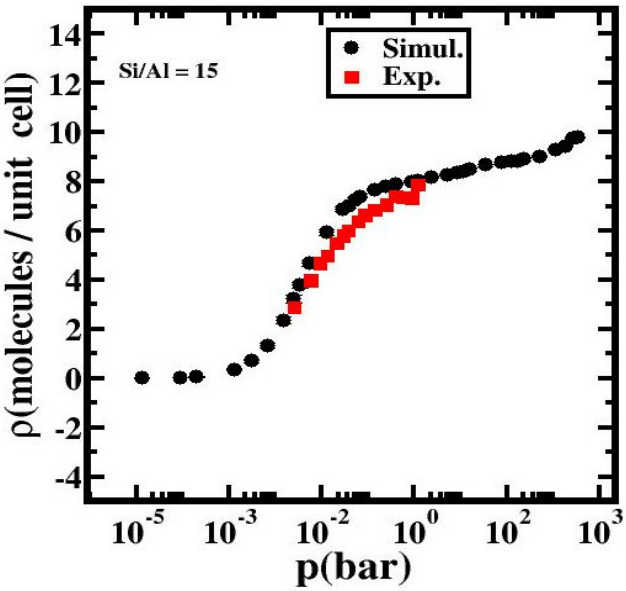

Figure 4-8. Comparison of equilibrium isotherm obtained by GCMC simulation with experimental equilibrium isotherm obtained from TEOM (isobutane on β-zeolite at T = 348 K).

4.4. Equilibrium Adsorption Isotherms of CO_2 on β-zeolite and USY-zeolite

In recent years, CEBC researchers have demonstrated that the liquid-like densities and better-than-liquid transport properties of CO_2-based reaction media may be exploited to enhance desorption of reaction products from porous solid-acid catalysts, significantly improving pore-accessibility and catalyst stability [Clark, 1998; Lyon, 2002; Lyon, 2004]. A fundamental understanding of the adsorption/desorption and mass transfer phenomena occurring in the catalyst exposed to CO_2-enhanced media is essential to rationally develop solid-acid catalyzed processes for industrial application. In this work, a preliminary investigation of CO_2 adsorption/desorption in zeolites was carried out.

Experiments of CO_2 adsorption/desorption on β-zeolite and USY-zeolite were performed under CO_2 partial pressure 0-1.4 bar at temperature 303-373 K (Figure 4-9). The key results are that at all temperatures investigated, (1) saturation adsorption is not achieved even up to 1.4 bar; (2) the shapes of adsorption isotherms are identical (nearly linear behavior) for both zeolites; and (3) adsorption capacities under the same conditions are similar for both zeolites.

(a)

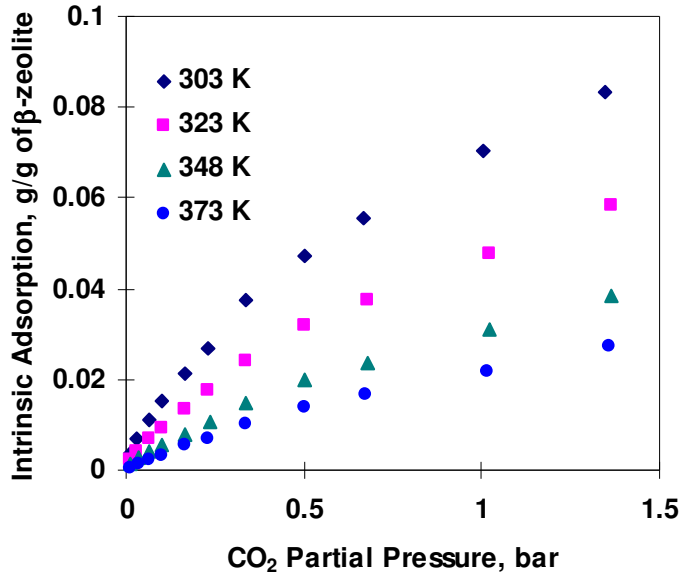

(b)

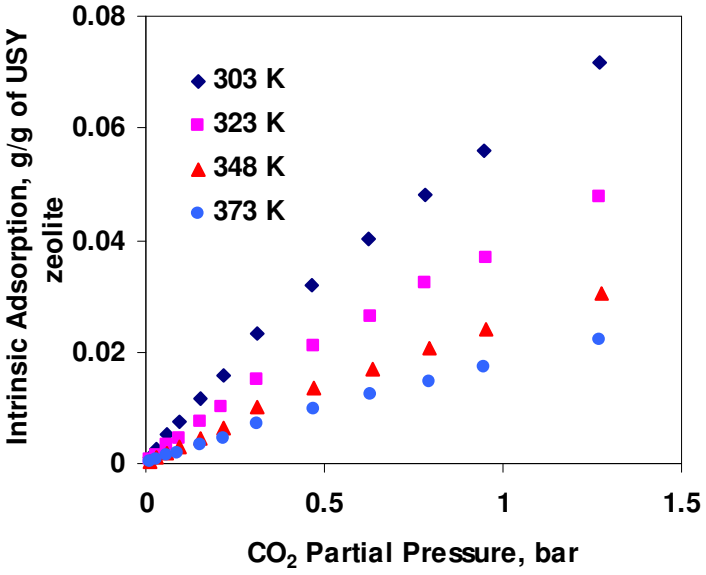

Figure 4-9. Intrinsic equilibrium adsorption isotherms of CO_2 in zeolites: (a) in β-zeolite; (b) in USY-zeolite.

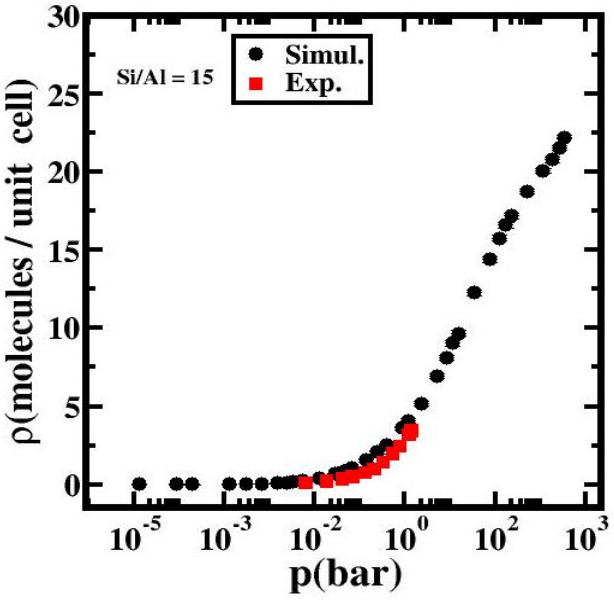

Figure 4-10. Comparison of equilibrium isotherm obtained by GCMC simulation with experimental equilibrium isotherm obtained from TEOM (CO_2 on β-zeolite at T = 348 K).

A comparison of equilibrium isotherm obtained by GCMC simulation with experimental equilibrium isotherm measured by a TEOM is shown in Figure 4-10. It can be seen that a good fit is achieved for the equilibrium adsorption isotherm of CO_2 in β-zeolite at 348 K. The molecular simulation predicts that the adsorption capacity of CO_2 under supercritical condition at 348 K is higher than 15 molecules/unit cell, which is at least 4-5 times of the adsorption capacity under 1 bar at 348 K. Such analysis provides insight into the adsorption/desorption of CO_2 in the CO_2-based reaction media.

4.5. Equilibrium Adsorption Isotherms of 224-TMP on β-zeolite

Experiments of 224-TMP adsorption/desorption on β-zeolite were performed under adsorbate partial pressure in the 0-0.06 bar range and at temperatures in the 348-473 K range. The equilibrium adsorption isotherms were measured under small incremental step changes of 224-TMP partial pressure. Similar experiments were performed in a gravimetric microbalance by Ruthven and Lee to measure the equilibrium adsorption isotherms of 224-TMP in 13X zeolite crystals [Ruthven, 1981].

As shown in Figure 4-11, the equilibrium adsorption isotherms of 224-TMP in β-zeolite at low temperatures (348-398 K) can be well described by the dual-site Langmuir model, while, at 473 K, the Langmuir model provides a good description. Similar trends were found for the equilibrium adsorption isotherms of isobutane and *n*-butane in β-zeolite as mentioned above. The fitted results of the equilibrium isotherms of 224-TMP in β-zeolite are listed in Table 4-3.

The adsorption capacity of 224-TMP in β-zeolite is 0.09-0.11 g/g of catalyst, almost identical to that of *n*-butane or isobutane in β-zeolite. Nonetheless, in β-zeolite, the adsorption affinity of 224-TMP is much greater than that of isobutane or *n*-butane, indicating that adsorbate size has a significant impact on the adsorption affinity.

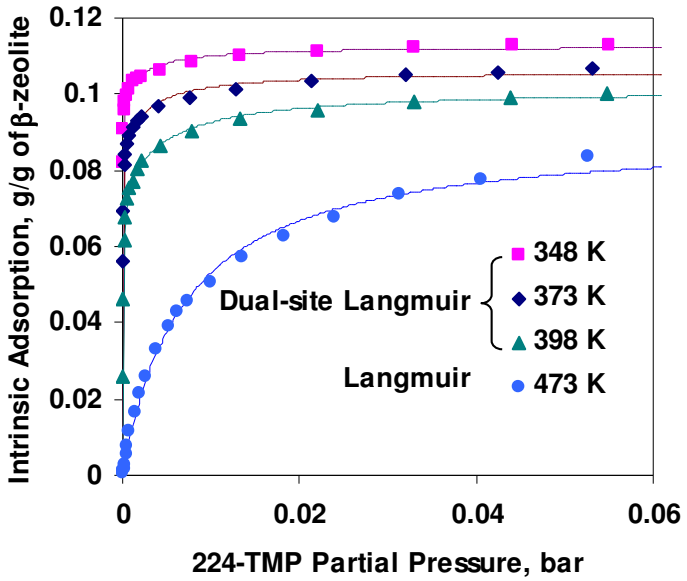

Figure 4-11. Intrinsic equilibrium adsorption isotherms of 224-TMP in β-zeolite.

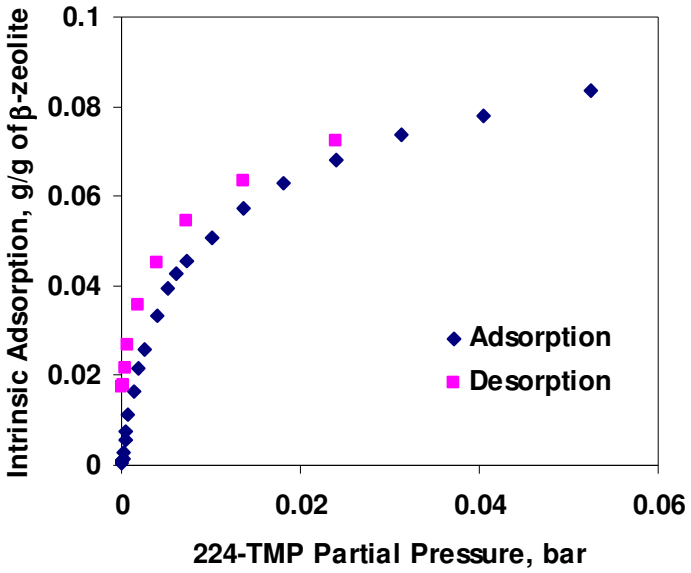

Figure 4-12. The adsorption and desorption equilibrium isotherms of 224-TMP in β-zeolite (T = 473 K).

In addition, the reversibility of the equilibrium adsorption isotherms was investigated. At temperatures lower than 473 K, it is almost impossible to study the reversibility because of the extremely slow desorption (see Chapter 5). Therefore, the investigation was carried out at 473 K, and the results are shown in Figure 4-12. It can be seen that the equilibrium adsorption isotherm is not completely reversible under the conditions studied.

4.6. Equilibrium Adsorption Isotherms of 224-TMP on Mesoporous Materials

Intrinsic 224-TMP equilibrium adsorption isotherms on Davicat SI 1301 silica support were obtained with a TEOM (T = 298-348 K, $P_{224\text{-TMP}}$ = 0-0.3 bar), as shown in Figure 4-13. At relative pressure (P/Po) less than 0.6, the isotherms are almost linear, while the slopes becomes much steeper at higher pressure (P/Po > 0.6). The steep slopes are caused by capillary condensation of 224-TMP in the mesopores [Duong, 1998]. In addition, the finite limit of adsorption capacity as P → Po is observed in this work. Assuming that the pores are filled with liquid 224-TMP (density = 0.69 g/cc) at P = Po and given that the pore volume of SI 1301 silica support is 1.15 cc/g, the maximum adsorption capacity of 224-TMP in SI 1301 is estimated to be 0.79 g/g of silica support, which is nearly close to the measured values (approximately 0.7 g/g of silica support).

The Brunauer model was demonstrated to be useful for the description of the equilibrium isotherms featured with capillary condensation and finite limit of adsorption saturation capacity [Duong, 1998]. Therefore, this model was used in this study to fit the equilibrium adsorption isotherms of 224-TMP in SI 1301. As shown in Figure 4-13, a good agreement between the experimental results and the fitted model was achieved.

Intrinsic equilibrium adsorption isotherms of 224-TMP on Davicat SI 1401 silica support were obtained with a TEOM (T = 298-373 K, $P_{224\text{-TMP}}$ = 0-0.25 bar). The equilibrium isotherms were fitted well by the Langmuir model as shown in Figure 4-14, and the fitted results are listed in Table 4-3. These results demonstrate the similarity (e.g., monolayer coverage in pores) between the zeolite pores and the micropores in SI 1401 silica support.

The saturation capacity of 224-TMP in SI 1401 silica support is approximately 36% higher than that of β-zeolite, and this finding correlates well with the BET characterization results (i.e., the total surface area of SI 1401 silica support is approximately 38% higher than that of β-zeolite).

The adsorption strength of 224-TMP in SI 1401 silica support is much weaker than that in β-zeolite possibly because the pore size of SI 1401 silica support is much larger. The effect of the acid sites is unclear and could also have a significant contribution to the stronger adsorption forces in the acidic zeolites used in this study.

(a)

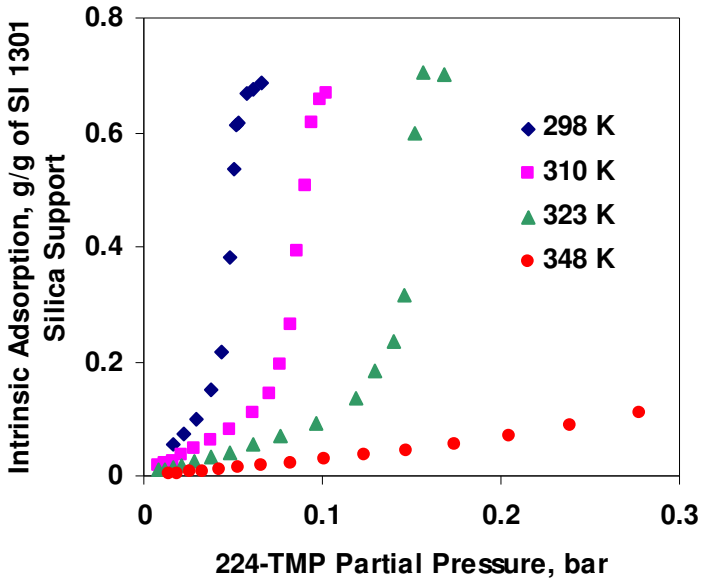

(b)

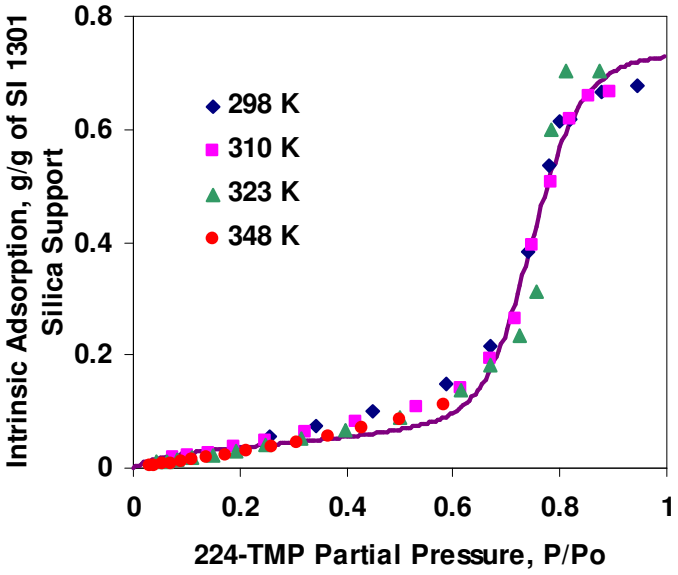

Figure 4-13. Equilibrium adsorption isotherms of 224-TMP in Davicat SI 1301 silica support (Brunauer model with fitting parameter: $v_m = 0.036$, c = 16.5, n = 20.4, and g = 1785.1).

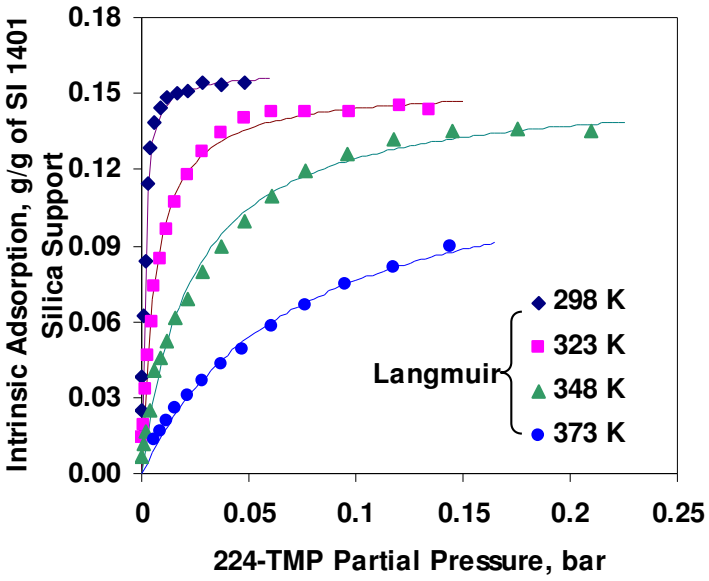

Figure 4-14. Equilibrium adsorption isotherms of 224-TMP in Davicat SI 1401 silica support.

The dramatic difference in the shapes of equilibrium isotherms between SI 1301 and 1401 indicates that the pore size has a significant effect on the adsorption/desorption behavior (the influence of acid sites is eliminated because both materials are non-acidic). The SI 1401 silica support with average pore size of 2.3 nm exhibits behaviors typical of microporous materials. Therefore, similar silica supports can possibly serve as good materials for the micropore adsorption/desorption study without the influence of various cations such as Na^+ and H^+. The SI 1301 silica support with average pore size of 14 nm exhibits behaviors typical of mesoporous materials and one can expect that the general adsorption and diffusion behaviors in mesoporous catalysts are similar to those in SI 1301 silica support when the impact of the acid site is assumed to be negligible.

Additionally, some preliminary experiments of 224-TMP adsorption/desorption in MCM-41 (with average pore size of 2.8 nm) were conducted under 224-TMP partial pressure 0-0.04 bar at temperature 295-323 K. It is found that the equilibrium adsorption isotherms of 224-TMP in MCM-41 (as shown in Figure 4-15) are similar to those in SI 1301 silica support. Liquid 224-TMP forms in the MCM-41 pores due to capillary condensation, when the relative pressure is higher than approximately 0.1.

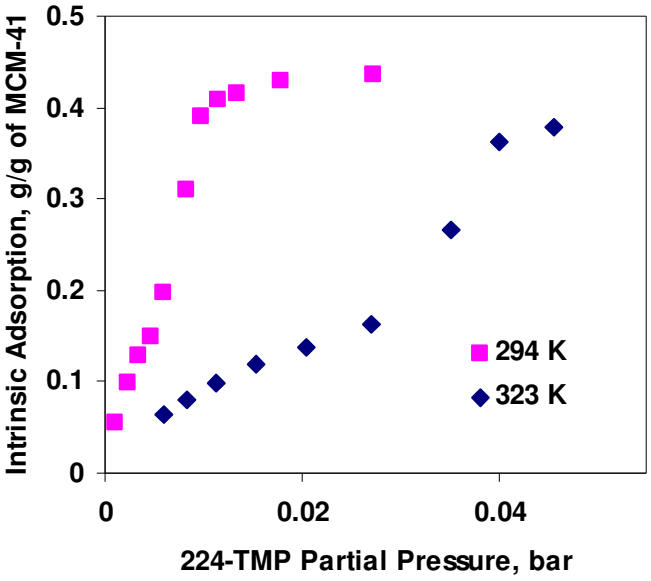

Figure 4-15. Equilibrium adsorption isotherms of 224-TMP in MCM-41.

4.7. Summary

A TEOM was successfully employed to obtain equilibrium adsorption isotherms for alkylation components in a variety of porous materials. The dual-site Langmuir

model provides good descriptions for the equilibrium isotherms of light alkanes and 224-TMP in β-zeolite at low temperatures, indicating the existence of two types of adsorption sites in β-zeolite. The reactants show facile adsorption/desorption in micro and mesoporous substrates, but the molecules of the most desired product (i.e., 224-TMP) are retained in micropores. The dramatic difference in the shapes of equilibrium isotherms between SI 1301 and 1401 silica supports indicates that the pore size has a significant effect on the adsorption/desorption behavior.

References

Barcia, P. S., Silva, J. A. C., Rodrigues, A. E., (2006). Separation by fixed-bed adsorption of hexane isomers in zeolite BETA pellets. Industrial & Engineering Chemistry Research 45, 4316-4328.

Chen, D., Rebo, H. P., Moljord, K., Holmen, A., (1999). Methanol conversion to light olefins over SAPO-34. Sorption, diffusion, and catalytic reactions. Industrial & Engineering Chemistry Research 38, 4241-4249.

Clark, M. C., Subramaniam, B., (1998). Extended alkylate production activity during fixed-bed supercritical 1-butene/isobutane alkylation on solid acid catalysts using carbon dioxide as a diluent. Industrial & Engineering Chemistry Research 37, 1243-1250.

Costa, E., Galleja, G., Jimenez, A., Pau, J., (1991). Adsorption equilibrium of ethylene, propane, propylene, carbon dioxide, and their mixtures on 13X zeolite. Journal of Chemical and Engineering Data 36, 218-224.

Duong, D. D., (1998) Adsorption analysis: Equilibria and kinetics, Imperial College Press: London, River Edge, NJ.

Houndonougbo, Y., Laird, B., (2008). unpublished results.

Hyun, H. S., Danner, P. R., (1982). Equilibrium adsorption of ethane, ethylene, isobutane, carbon dioxide, and their binary mixtures on 13X molecular sieves. Journal of Chemical and Engineering Data 27, 196-200.

Lee, C. K., Ashtekar, S., Gladden, L. F., Barrie, P. J., (2004). Adsorption and desorption kinetics of hydrocarbons in FCC catalysts studied using a tapered element oscillating microbalance (TEOM). Part 1: experimental measurements. Chemical Engineering Science 59, 1131-1138.

Lyon, C. J., Optimization of activity and selectivity by pressure-tuning during solid-acid catalyzed isoparaffin/olefin alkylation in supercritical carbon dioxide, Thesis (Ph. D.), University of Kansas, Chemical and Petroleum Engineering, 2002.

Lyon, C. J., Sarsani, V. S. R., Subramaniam, B., (2004). 1-butene plus isobutane reactions on solid acid catalysts in dense CO_2-based reaction media: Experiments and modeling. Industrial & Engineering Chemistry Research 43, 4809-4814.

Platon, A., Thomson, W. J., (2005). Solid acid characteristics and isobutane/butene alkylation. Applied Catalysis A: General 282, 93-100.

Ruthven, D. M., Lee, L. K., (1981). Kinetics of non-isothermal sorption - Systems with bed diffusion control. AIChE Journal 27, 654-663.

Suzuki, M., (1990) Adsorption engineering, Kodansha; Elsevier: Tokyo.

Zhu, W., van de Graaf, J. M., van den Broeke, L. J. P., Kapteijn, F., Moulijn, J. A., (1998). TEOM: A unique technique for measuring adsorption properties. Light alkanes in silicalite-1. Industrial & Engineering Chemistry Research 37, 1934-1942.

Chapter 5 Adsorption/Desorption Dynamics of Model Alkylation Compounds in Microporous and Mesoporous Catalysts

For solid acid catalyzed alkylation, understanding the fundamentals of the adsorption, desorption, and mass transfer rates of reactants and products in the most promising catalysts is key to screen potential solid acid catalysts and rationally determine operating conditions. The present work uses a TEOM to elucidate for the first time the adsorption/desorption characteristics of model compounds of relevance in 1-butene+isobutane alkylation on large-pore (12-ring) zeolites (and mesoporous materials). The specific objectives of the adsorption/desorption dynamics investigation in this dissertation are to:

(a) Investigate the ability of TEOM as a tool to measure micropore and macropore diffusivities for commercially available large-pore zeolites with small crystal sizes (< 1 μm) and gain a deeper understanding of the applicability or limitations of this instrument for diffusivity measurement

(b) Experimentally investigate adsorption/desorption rates of model compounds of relevance in 1-butene+isobutane alkylation on zeolites (and mesoporous materials)

(c) Develop complementary theoretical models to reliably interpret the experimental data and obtain fundamental parameters

In this chapter, the mathematical models used to describe the adsorption/desorption dynamics of the model alkylation compounds in zeolite crystals and particles are first presented. The second part of this chapter discuss some of the limitations of the TEOM technique for measuring intrinsic diffusivities in large-pore zeolites with small crystal sizes. Then, the adsorption/desorption kinetics of 224-TMP in β-zeolite are presented, and detailed follow-up investigations performed to better understand the extremely slow desorption kinetics of 224-TMP from β-zeolite are described. Finally, investigations into the pore accessibility of 224-TMP in some mesoporous materials are presented.

5.1. Mathematical Modeling of Adsorption/Desorption Dynamics

As mentioned earlier, the zeolite crystals employed in this work form small particles through self-aggregation. The particle diameter (4-30 μm) is measured with a SEM by spreading the sample particles on a smooth metal surface. When packed in the TEOM, larger particles can be formed through compaction and aggregation. To investigate the effects of such aggregation on adsorption/desorption dynamics and diffusivity measurements, controlled-size cylindrical pellets of the zeolite samples were formed with a high pressure press and systematically studied in the TEOM. As

shown in Figure 5-1, the above-mentioned particles and pellets will exhibit a bimodal pore size distribution, with the smaller mean pore size representing the micropores (pore size < 2 nm) of the zeolite crystals and the larger mean pore representing the mesopores (2 nm < pore size < 50 nm) or macropores (pore size > 50 nm) formed by the aggregation of the crystals.

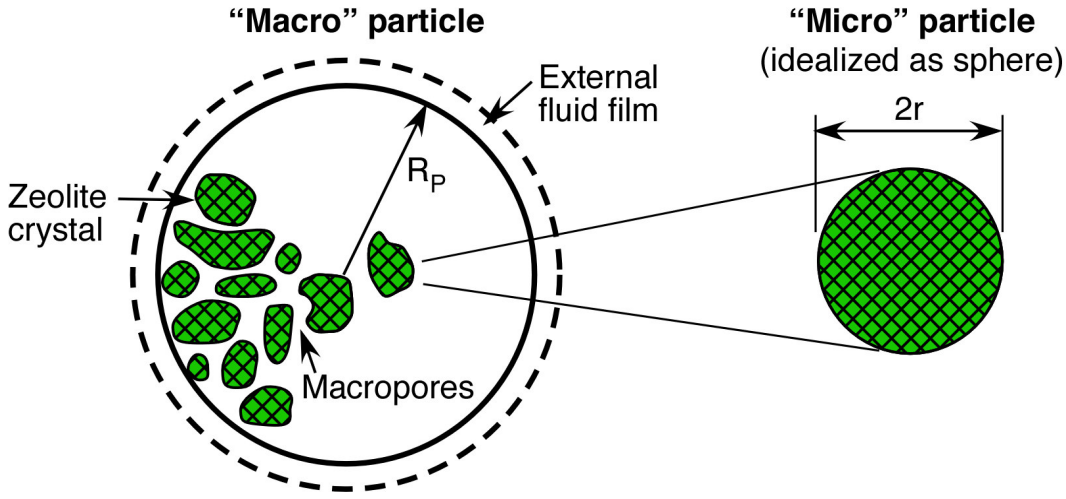

Figure 5-1. Schematic diagram of a zeolite particle.

In the present work, the bed-length effect was found to be negligible when sufficiently small sample sizes and sufficiently high carrier gas flow rates are used in the experiments (discussed in Section 5.2). Only in such a case is it justifiable to employ a single particle model to adequately describe the observed adsorption/desorption dynamics. In the single particle model, the external fluid film resistance may also be assumed to be negligible at relatively high carrier gas flow rates.

5.1.1. Micropore Diffusion Control

If the diffusion through extracrystalline space in the aggregated particles and the transport at the crystal surface are rapid, then the rate of adsorption/desorption will be controlled by intracrystalline diffusion.

When sufficiently small step changes are introduced in the experiments, it is reasonable to assume that, over each step change, the equilibrium adsorption isotherm is linear and the diffusivity is constant. Assuming that the crystals can be adequately represented by a spherical micro-particle, the analytical solution for sorption dynamics is as follows [Kärger, 1992]:

$$\frac{m_t}{m_\infty} = 1 - \frac{6}{\pi^2}\sum_{n=1}^{\infty}\frac{1}{n^2}\exp\left(-\frac{n^2\pi^2 D_c t}{r_c^2}\right) \tag{5-1}$$

where m_t is the mass adsorbed at time t, m_∞ is the mass adsorbed at $t \to \infty$, D_c is the intracrystalline diffusivity, and r_c is the radius of zeolite crystal.

When the adsorption/desorption profiles are measured over large step changes of adsorbate concentration, the non-linearity of the equilibrium adsorption isotherm should be considered, and the assumption of constant diffusivity is usually not valid. Assuming that the equilibrium adsorption isotherm is described well by a Langmuir-type equation, the intracrystalline diffusivity can be written in the form [Kärger, 1992]:

$$D_c = \frac{D_0}{1 - q/q_s} \tag{5-2}$$

where D_0 is the corrected intracrystalline diffusivity. Accordingly, the transient mass balance in a spherical micro-particle is as follows:

$$\frac{\partial q}{\partial t} = \frac{D_0}{r^2}\frac{\partial}{\partial r}\left(\frac{r^2}{1 - q/q_s}\frac{\partial q}{\partial r}\right) \tag{5-3}$$

where r is the radial distance in zeolite crystal. The relevant initial and boundary conditions are:

$$t < 0, \quad c = c_0, \quad q = q_0 \tag{5-4a}$$

$$t \geq 0, \quad c = c_\infty, \quad q(r_c, t) \to q_\infty \tag{5-4b}$$

$$t \to \infty, \quad c = c_\infty, \quad q(r, t) \to q_\infty \tag{5-4c}$$

$$\left.\frac{\partial q}{\partial t}\right|_{r=0} = 0 \quad \textit{for all } t \tag{5-4d}$$

where c is the concentration in external fluid phase, c_0 is the initial value of c, c_∞ is the value of c as $t \to \infty$, q_0 is the initial value of q, and q_∞ is the value of q as $t \to \infty$.

The diffusivity is obtained by fitting the transient experimental data to either the analytical solution (Equation 5-1) or the numerical solution of Equations 5-3 and 5-4.

5.1.2. Mesopore/Macropore Diffusion Control

If the intracrystalline diffusion is rapid, the adsorption/desorption rate will be controlled by diffusion through the mesopores/macropores of the aggregated particles.

A mathematical model was developed to describe the diffusion in the cylindrical pellets over a small concentration step. The key assumptions include: (a) the intracrystalline diffusion is rapid; (b) the external transport resistances are negligible; (c) the pellets are isothermal; and (d) the equilibrium adsorption isotherm is linear with concentration under differential concentration steps. The transient intra-pellet mass balance equation is:

$$\frac{\partial c}{\partial t} = D_e\left(\frac{1}{R}\frac{\partial}{\partial R}\left(R\frac{\partial c}{\partial R}\right)+\frac{\partial}{\partial Z}\left(\frac{\partial c}{\partial Z}\right)\right) \tag{5-5}$$

and the relevant initial and boundary conditions are:

$$c(Z,R,0) = c_0 \tag{5-6a}$$

$$c(Z,R_p,t) = c_\infty \tag{5-6b}$$

$$c(Z_{\pm 0.5L},R,t) = c_\infty \tag{5-6c}$$

where D_e is the effective mesopore/macropore diffusivity, R is the radial coordinate in the pellet, Z is the distance coordinate, R_p is the pellet radius, and L is the cylinder

length. The effective mesopore/macropore diffusivity may be written as [Kärger, 1992]:

$$D_e = \frac{\varepsilon_p D_p}{\varepsilon_p + (1-\varepsilon_p)(dq^*/dc)} \tag{5-7}$$

where D_p is the pore diffusivity, ε_p is the porosity of the pellet, q^* is the equilibrium adsorbed phase concentration, and dq^*/dc is the slope of the equilibrium adsorption isotherm.

When large step changes are employed in the experiments, the dependence of the diffusivity on the concentration in the adsorbed phase must also be considered in the kinetic modeling. The previous model was therefore modified to describe the diffusion in the cylindrical pellets over a large concentration step. Assuming that the equilibrium adsorption isotherm can be adequately represented by the Langmuir equation, the intra-pellet mass balance equation is as follows [Kärger, 1992]:

$$\frac{\partial q}{\partial t} = D_{e0}\left(\frac{1}{R}\frac{\partial}{\partial R}\left(\frac{R}{(1-q/q_s)^2}\frac{\partial q}{\partial R}\right)+\frac{\partial}{\partial Z}\left(\frac{1}{(1-q/q_s)^2}\frac{\partial q}{\partial Z}\right)\right) \tag{5-8}$$

and the relevant initial and boundary conditions are:

$$q(Z,R,0) = q_0 \tag{5-9a}$$

$$q(Z,R_p,t) = q_\infty \tag{5-9b}$$

$$q(Z_{\pm 0.5L}, R, t) = q_{\infty} \tag{5-9c}$$

where D_{e0} is the limiting effective mesopore/macropore diffusivity as $q \to 0$, and may be expressed as [Kärger, 1992]:

$$D_{e0} = \frac{\varepsilon_p D_p}{(1-\varepsilon_p) b q_s} \tag{5-10}$$

The partial differential equations along with the initial and boundary conditions were solved in Femlab [COMSOL, 2004] that employs a finite element method. The experimental adsorption/desorption profiles were regressed with the model solution to obtain the effective mesopore/macropore diffusivities.

5.2. Adsorption/Desorption Dynamics of Isobutane, *n*-Butane, and Propane in β-zeolite and USY-zeolite

5.2.1. Effects of Bed-length and Film Mass Transfer Resistance

In order to properly identify the dominant mass transfer resistance in the TEOM experiments, systematic investigations of the adsorption/desorption dynamics were undertaken under carefully controlled conditions. The bed-length effect on the overall adsorption/desorption dynamics was tested by varying both the packing length and, at each bed length, the carrier gas flow rate as well. In the study of hydrocarbon adsorption/desorption in a commercial FCC catalyst and a pure rare-earth exchanged

zeolite Y sample using a TEOM, Lee et al. [Lee, 2004] varied the carrier gas flow rate at a fixed bed length and concluded that the concentration gradient down the fixed bed is negligible beyond the carrier gas flow rate at which the dynamic profiles became invariant. Based on this assumption, the environment surrounding each catalyst particle in the fixed bed was considered to be identical. Clearly, this assumption is valid only below a certain bed length ("differential" operation).

Indeed, further experimental investigation into the same system reported by Lee et al. (*p*-xylene in FCC catalyst) indicates that the invariance of the adsorption/desorption dynamics on carrier gas flow rate does not necessarily imply that the concentration gradient down the packed bed is negligible. For a certain sample size ($\leq$ ~ 64 mg), the transient adsorption/desorption profiles at 373 K and *p*-xylene partial pressure of 0.006 bar overlap with each other when carrier gas flow rate is $\geq$ 400 sccm. However, at the carrier gas flow rate of 400 sccm, the adsorption/desorption dynamics are strongly influenced by sample size, as shown in Figure 5-2. The adsorption/desorption rates for smaller sample sizes are higher under otherwise identical conditions, clearly demonstrating the significance of bed-length effect on the observed dynamics during TEOM experiments. In other words, the invariance of the adsorption/desorption dynamics on both the carrier gas flow rate and the sample size must be experimentally confirmed for reliable interpretation of the data and the rate determining steps.

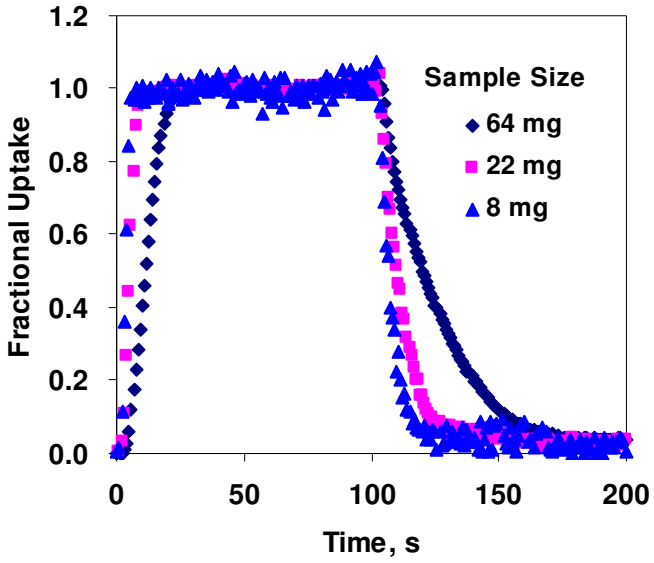

Figure 5-2. Effect of sample size on sorption profiles for *p*-xylene in FCC catalyst (T = 373 K, carrier gas is helium flowing at 400 sccm, P_{total} = 1.01 bar, $P_{p\text{-xylene}}$ = 0.006 bar).

The transient adsorption/desorption profiles of isobutane, *n*-butane, and propane in β- and USY-zeolite crystals were measured under adsorbate partial pressure 0-1.1 bar at temperature 303-398 K. The effects of carrier gas flow rate and sample size on adsorption/desorption profiles were investigated (Figure 5-3 and 5-4). At 323 K, isobutane partial pressure of 0.015 bar and a sample size of 7.4 mg, the adsorption/desorption profiles become invariant with flow beyond 333 sccm (Figure 5-3). However, further experiments with decreased sample size clearly demonstrate that sample size effects are significant even at the highest carrier gas flow rate of 400 sccm (Figure 5-4). These results reinforce the fact that the absence of bed-length effects in TEOM studies must be confirmed by varying both the flow rates as well as the sample size.

(a)

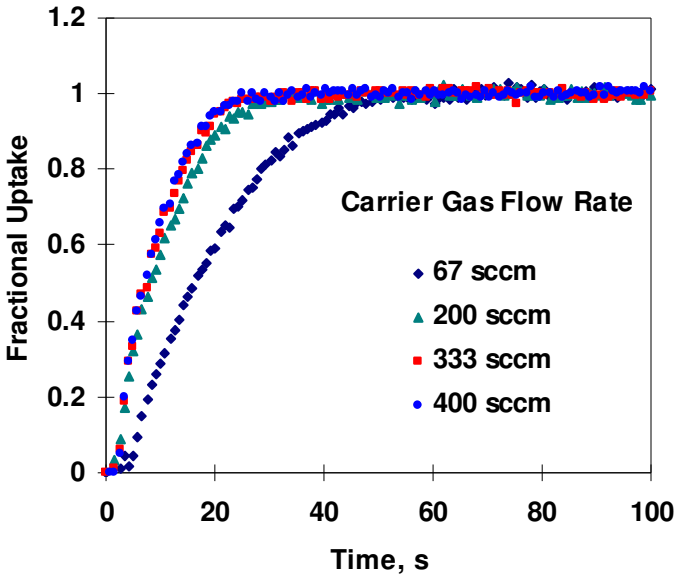

(b)

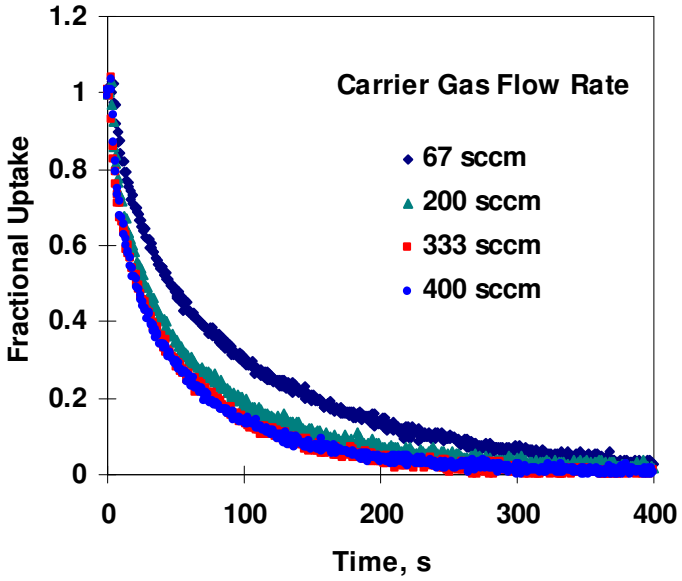

Figure 5-3. Effect of carrier gas (He) flow rate on sorption profiles for isobutane in β-zeolite (T = 323 K, P_{iC4} = 0.015 bar, P_{total} = 1.01 bar, sample size = 7.4 mg): (a) adsorption profiles; (b) desorption profiles.

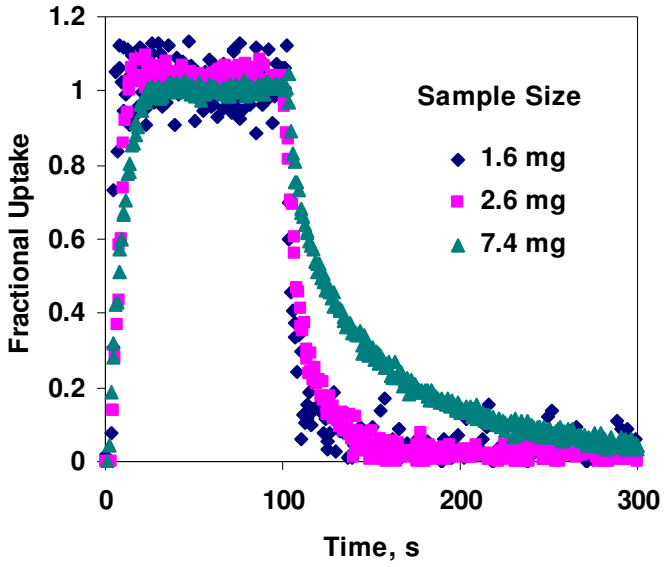

Figure 5-4. Effect of sample size on sorption profiles for isobutane in β-zeolite (T = 323 K, carrier gas is helium flowing at 400 sccm, P_{iC4} = 0.015 bar, P_{total} = 1.01 bar).

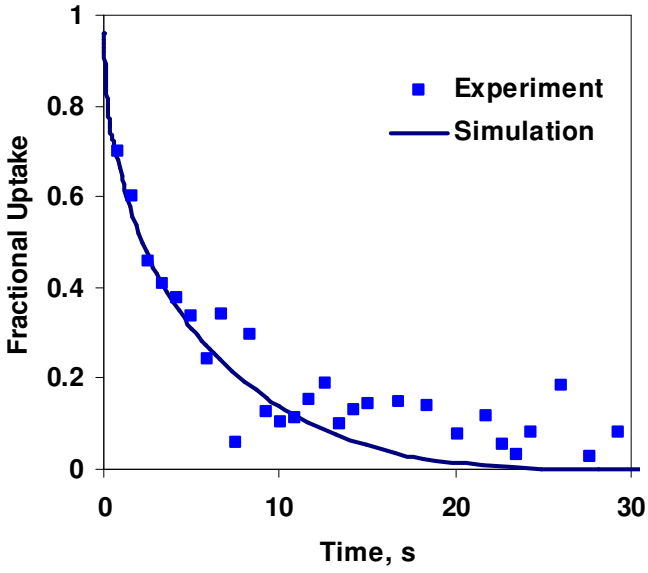

Figure 5-5. Experimental and simulated desorption profiles for isobutane in β-zeolite (T = 323 K, carrier gas is helium flowing at 400 sccm, P_{total} = 1.01 bar, P_{iC4} = 0.015-0 bar).

The mathematical model for intracrystalline diffusion control (described in Section 5.1.1) was used to fit the isobutane sorption profiles in β-zeolite with sample size of 1.6 mg at helium flow rate of 400 sccm at 323 K, conditions under which the bed-length effect and external film resistance are minimized. As shown in Figure 5-5, the model represents the experimental profile reasonably well, with the corrected intracrystalline diffusivity (D_0) of 8×10^{-12} cm^2/s. In sharp contrast, the intracrystalline diffusivity of *n*-butane in large-pore (12-ring) zeolites measured by other techniques using large crystals [Kärger, 1992] are 3-4 orders of magnitude higher than the value obtained in this study, implying that an additional mass transfer resistance, rather than intracrystalline diffusion alone, is likely dominant in our measurements. Notice that the samples employed in this work are aggregated crystals, and the agglomeration of crystals could possibly impose a significant extracrystalline mass transfer limitation. Such a possibility is investigated in the following section.

5.2.2. Effect of Crystal Agglomeration

To study the effect of crystal agglomeration on the sorption dynamics, pelleted zeolite samples were employed. The pellets were formed by pressing the powder-form zeolites under ~ 7 MPa pressure into 3.5-mm-thick, 3.5-mm-diameter cylinders. The transient sorption profiles of isobutane, *n*-butane, and propane were each investigated in pelletized β- and USY-zeolite samples under adsorbate partial pressures in the 0-1.1 bar range and at temperatures in the 303-398 K range. The

adsorption/desorption profiles were measured over small concentration steps, such that the rates of desorption and adsorption are identical.

(a)

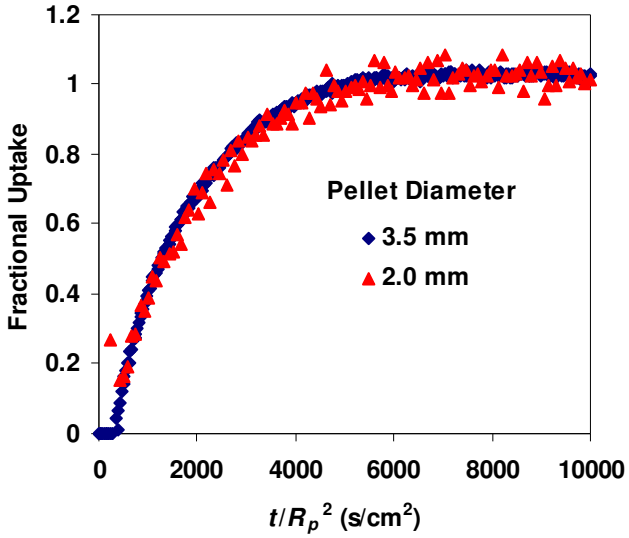

(b)

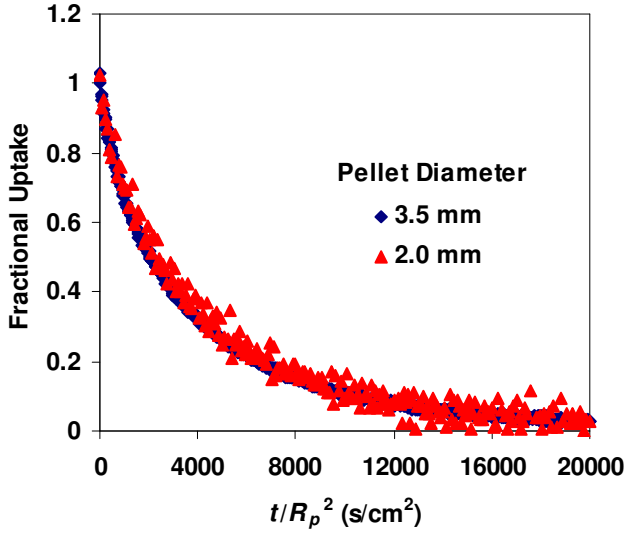

Figure 5-6. Effect of pellet size on sorption profiles for isobutane in β-zeolite (T = 323 K, carrier gas is helium flowing at 400 sccm, P_{total} = 1.01 bar, P_{iC4} = 0.005 bar): (a) adsorption profiles; (b) desorption profiles.

It is found that the sorption curves merge with each other when plotted versus t/R_p^2 (Figure 5-6). This implies that mesopore/macropore diffusion resistance, introduced by the pelletization step, is dominant [Kärger, 1992; Duong, 1998]. Similar investigations have been reported in the literature to study the effect of crystal agglomeration on observed kinetics. For example, Ruthven and Xu [Ruthven, 1993] confirmed that the mesopore/macropore diffusion is the rate-limiting step for oxygen and nitrogen adsorption/desorption in commercial 0.5 nm pellets using different particle size fractions by the ZLC method. Using a conventional electrobalance, Youngquist et al. [Youngquist, 1971] investigated butylene adsorption/desorption in calcium microtraps of different sizes and found that the extracrystalline transport is rate limiting.

The adsorption/desorption profiles were regressed with model solution (Section 5.1.2) to obtain effective mesopore/macropore diffusivities. The model fits the sorption curves reasonably well, as shown in Figure 5-7. The concentration dependence of effective diffusivity under the conditions of mesopore/macropore diffusion control is shown in Figure 5-8. At a given temperature, the effective mesopore/macropore diffusivity increases with adsorbate loading, mainly due to the decreasing slope of the equilibrium adsorption isotherm (dq^*/dc) [Kärger, 1992]. The pore diffusivities (D_p) can be calculated from the effective mesopore/macropore diffusivities using the values of ε_p (obtained from porosimetry) and dq^*/dc (derived

from the equilibrium adsorption isotherms). The dependence of pore diffusivities on adsorbate concentration or pressure may be further studied [Kärger, 1992].

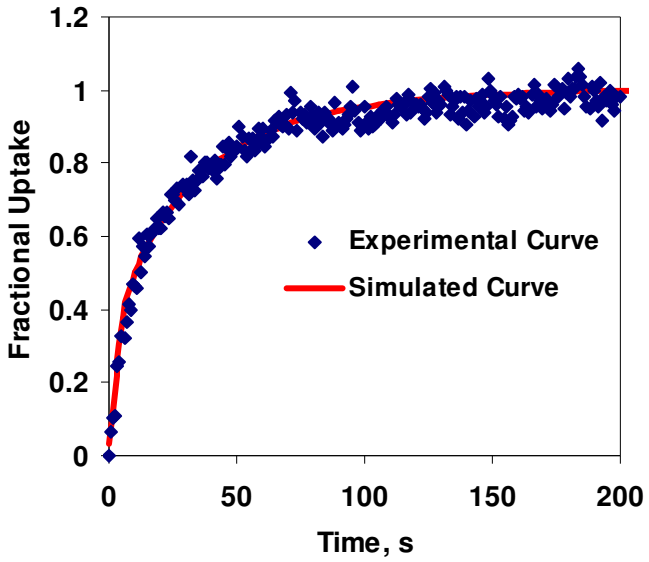

Figure 5-7. Experimental and simulated uptake curves for isobutane in β-zeolite pellets (T = 348 K, carrier gas is helium flowing at 400 sccm, P_{total} = 1.01 bar, P_{iC4} = 0.005-0.0075 bar).

(a)

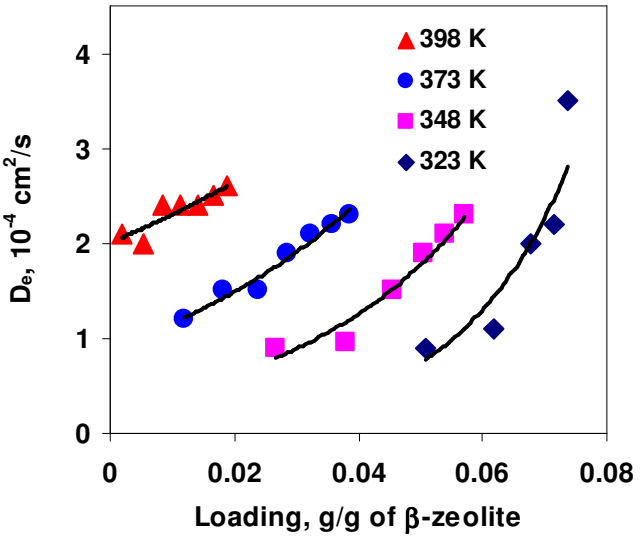

(b)

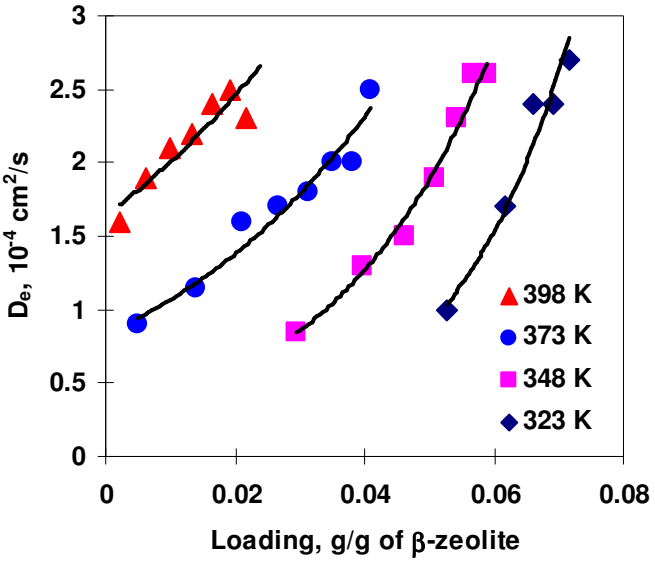

(c)

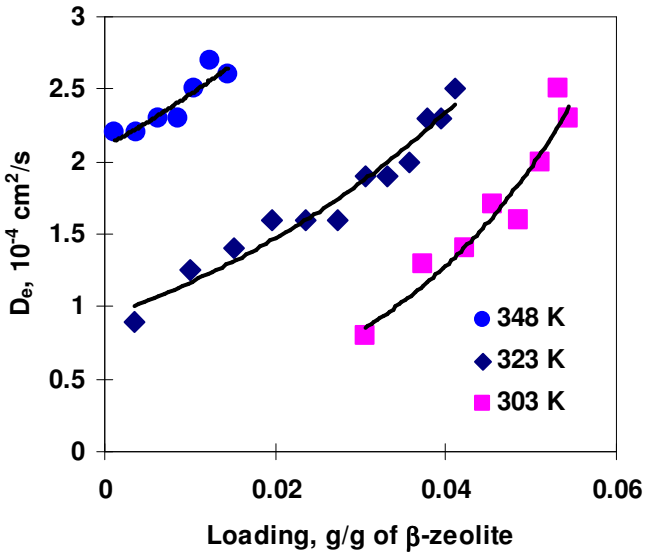

Figure 5-8. Concentration dependence of effective mesopore/macropore diffusivity (carrier gas is helium flowing at 400 sccm, P_{total} = 1.01 bar): (a) isobutane in β-zeolite pellets; (b) *n*-butane in β-zeolite pellets; (c) propane in β-zeolite pellets.

5.2.3. Limitations of the TEOM Technique for Diffusivity Measurement

In principle, there is an upper limit of the diffusional time constant (D/R^2) that the TEOM technique can measure. Above the limit, the diffusion is too rapid, and the contribution from the inevitable mixing and time delay due to dead volume in the system becomes dominant, rendering it impossible to obtain reliable diffusion dynamics data.

When there is negligible adsorption (as when using nonporous quartz particles), the response curve is fairly close to an ideal step due to the small dead volume in the system. The new equilibrium state is obtained within 2-4 s after a step change reaches the packed bed in a TEOM [Lee, 2004]. Therefore, the sorption time scale should be at least 20 s so that the dead volume effects can be considered insignificant. Such a time frame corresponds to an approximate value of $D/R^2 = 0.02\ s^{-1}$ for a spherical particle [Duong, 1998]. Consequently, a reasonable criterion for reliable measurement of diffusional time constant by the TEOM technique is: $D/R^2 < 0.02\ s^{-1}$. An almost identical criterion has been used by Kärger and Ruthven [Kärger, 1992] for the ZLC technique, and it has been demonstrated to be useful for properly choosing the operating conditions in the diffusivity measurements.

At 298-373 K, the intracrystalline diffusivity of *n*-butane in large-pore (12-ring) NaX zeolites with large crystals is determined to be of order $10^{-7}\ cm^2/s$ by classic macroscopic methods (e.g., the ZLC and gravimetric methods) [Kärger, 1992]. Assuming that *n*-butane has similar diffusivities in the commercial β-zeolite and

USY-zeolite crystals (< 1 μm), the diffusion time scale will be of order 2.5×10^{-2} s, which is not measurable by the TEOM technique. Only when the crystal size of these zeolites is larger than 44 μm, the intracrystalline diffusivity can be reliably extracted from the transient measurements by the TEOM technique.

In our studies of isobutane, *n*-butane, and propane adsorption/desorption in pelleted zeolite samples, the measured effective mesopore/macropore diffusivity is on the order of 10^{-4} cm^2/s, and the diffusion time scale for the 2 mm pellet is on the order of 100 s. When the pellet diameter is less than 1.4 mm, the diffusivity measurements using the TEOM become unreliable.

5.3. Adsorption/Desorption Dynamics of 224-TMP in β-zeolite

Intrinsic 224-TMP adsorption/desorption profiles on β-zeolite in response to step input changes were obtained with a TEOM (T = 298-473 K, $P_{224\text{-}TMP}$ = 0-0.3 bar). The impact of sample size on the measured kinetics was investigated to determine whether the bed-length effect is significant under the conditions investigated. For measuring the intrinsic 224-TMP adsorption/desorption profiles in β-zeolite, a carrier gas flow rate of 400 sccm is used since all the previous experiments have shown that external film resistance is eliminated when the gas flow rate is greater than 333 sccm.

(a)

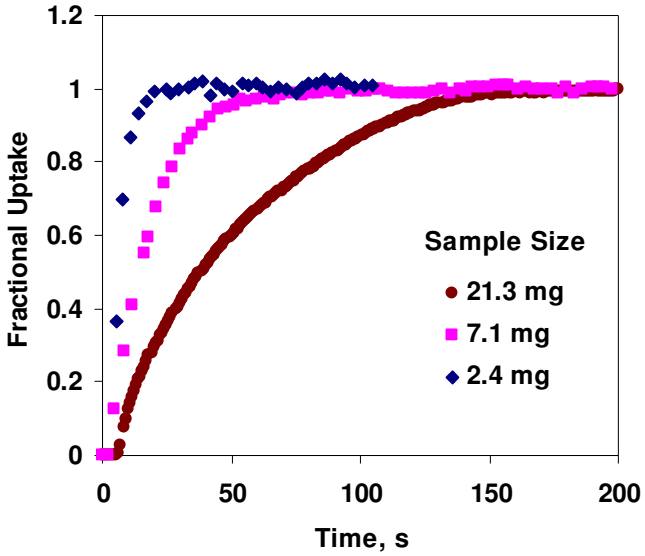

(b)

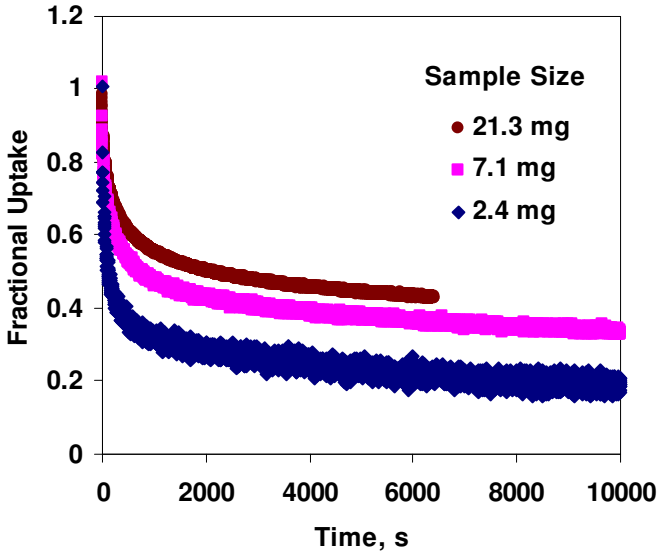

Figure 5-9. TEOM profiles on β-zeolite following 224-TMP step input and 224-TMP desorption by helium purging (T = 373 K, carrier gas is helium flowing at 400 sccm, P_{total} = 1.1 bar, $P_{224\text{-}TMP}$ = 0.006 bar): (a) adsorption profiles; (b) desorption profiles.

The qualitative trends are similar to those observed in the cases of *n*-butane, isobutane, and propane adsorption/desorption in β-zeolite and USY-zeolite (Section

5.2). As shown in Figure 5-9, the sample size imposes a strong influence on the transient sorption profiles, implying that the bed-length effect is significant under the conditions studied. The adsorption (or desorption) of 224-TMP preferentially occurs at the top of the bed during the early stages of adsorption (or desorption) when the bed-length effect is significant. Under such conditions, a fixed-bed model, rather than a single particle model, should be employed to properly describe the adsorption/desorption kinetics. Further, using small zeolite crystals usually results in unreliable measurement of intracrystalline diffusivity because of very short diffusion time in the crystals relative to measurement sensitivity. Even though the TEOM experiments aimed to measure the intracrystalline diffusivity using small commercially available crystals were demonstrated to be difficult and sometimes impossible, the TEOM technique is nevertheless useful to identify the rate-limiting step and to obtain useful data such as mesopore/macropore diffusivity and intrinsic adsorption capacities under carefully controlled conditions. These results are essential for the rational design of catalyst pellets and supports.

As shown in Figure 5-9b, the desorption rates of 224-TMP from β-zeolite by helium purging are extremely slow. More interestingly, each desorption profile is discontinuous in nature, with a rapid initial drop in mass followed by a much longer transience. These trends imply that there are possibly two distinct rate-limiting steps for the desorption dynamics.

(a)

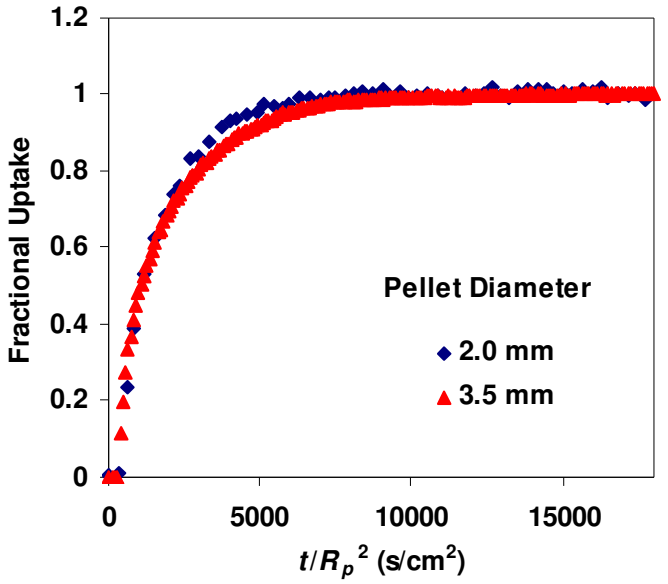

(b)

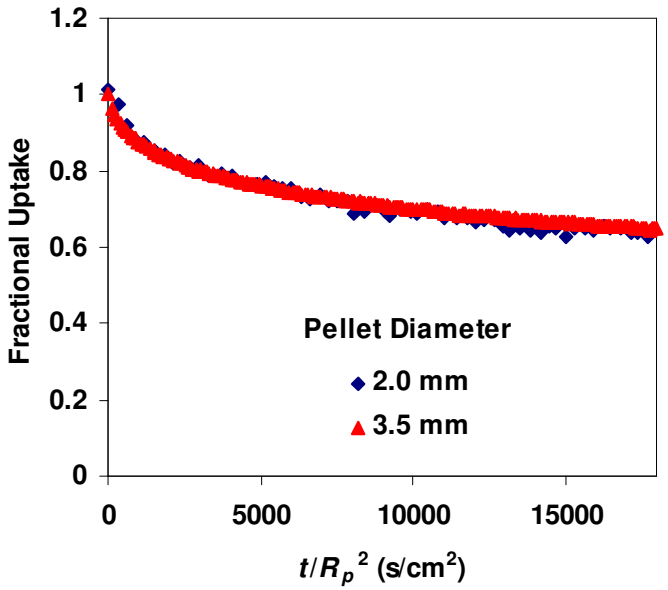

Figure 5-10. TEOM profiles on β-zeolite pellets with different diameters following 224-TMP step input and 224-TMP desorption by helium purging (T = 373 K, carrier gas is helium flowing at 400 sccm, P_{total} = 1.1 bar, $P_{224\text{-TMP}}$ = 0.006 bar): (a) adsorption profiles; (b) desorption profiles (initial rapid desorption phase).

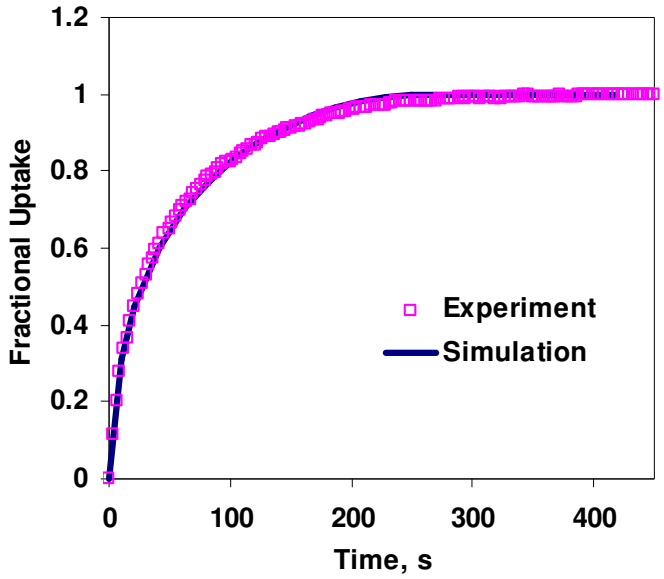

Figure 5-11. Experimental and simulated adsorption profiles for 224-TMP in β-zeolite pellet (T = 373 K, carrier gas is helium flowing at 400 sccm, P_{total} = 1.1 bar, $P_{224\text{-}TMP}$ = 0.006 bar, pellet diameter is 3.5 mm).

Alpay et al. [Alpay, 2003] observed similar dual-stage desorption behavior in measuring the desorption rate of hexane from silicalite at 373 K using a TEOM. They explained the duality in desorption as a result of condensation in the mesoporous pockets or of other hindrance (e.g., pore blocking). However, no further experiment was performed in their work to clarify the mechanisms for the observed duality of desorption rates.

In this study, Kelvin's capillary condensation theory suggests that capillary condensation cannot occur at a high temperature of 373 K and a low 224-TMP partial pressure of 0.006 bar. A possible speculation for the rate-limiting step is macropore diffusion, which was investigated by varying the pellet size.

As shown in Figure 5-10, the transient curves corresponding to adsorption and the initial rapid desorption step scale with t/R_p^2, implying that the adsorption and initial stage of desorption are controlled by macropore diffusion. As shown in Figure 5-11, the adsorption profile is described well by the macropore diffusion model presented in Section 5.1.2, and the limiting effective diffusivity as $q \to 0$ (D_{e0}) for the illustrated curve is approximately 1.2×10^{-6} cm^2/s. In contrast, the desorption curves corresponding to the long transiences do not scale with t/R_p^2, implying that the second stage of desorption is not controlled by macropore diffusion resistance.

It is possible that the strong chemisorption of the probe molecules in the acidic (protonated) β-zeolite contributes to the extremely slow desorption kinetics. This possibility was studied by comparing the experimental results using acidic β-zeolite and sodium-form β-zeolite under identical conditions (the detailed procedure of cation exchange was described in Section 4.2.1). The experimental results are compared in Figure 5-12. The adsorption capacities are identical for both types of β-zeolite (results are not shown in Figure 5-12) under the operating conditions investigated, indicating that the acidity imposes little influence on the overall adsorption capacity in β-zeolite. Additionally, identical adsorption profiles and identical initial desorption profiles were observed on sodium-form and H-form β-zeolites. Such results are in excellent agreement with the finding that the adsorption and the initial stage of desorption are controlled by macropore diffusion. Because the cation exchange only affects the adsorption/desorption and diffusion phenomena in

the microporous structure, it is reasonable to expect that extracrystalline diffusion in the mesopores/macropores would be unaffected in acid and neutral forms of the β-zeolite. Note from Figure 5-12 that the second-stage desorption rate of 224-TMP from H-form zeolite is significantly slower than that from Na-form zeolite: it takes approximately 1.5 h to approach complete desorption in the Na-form zeolite, but for the H-form zeolite, desorption is not complete even after 10 h of He purging. Such results indicate that chemisorption possibly occurs in the H-form β-zeolite because of the strong interaction between 224-TMP and H^+.

The significant buildup of 224-TMP can impose significant mass transport limitations inside β-zeolite pores (even in Na-form β-zeolite pores). The accumulation of 224-TMP and other heavy compounds inside the pores will therefore result in catalyst deactivation as observed in the many studies reviewed earlier [deJong, 1996; Nivarthy, 1998; Weitkamp, 1999].

(a)

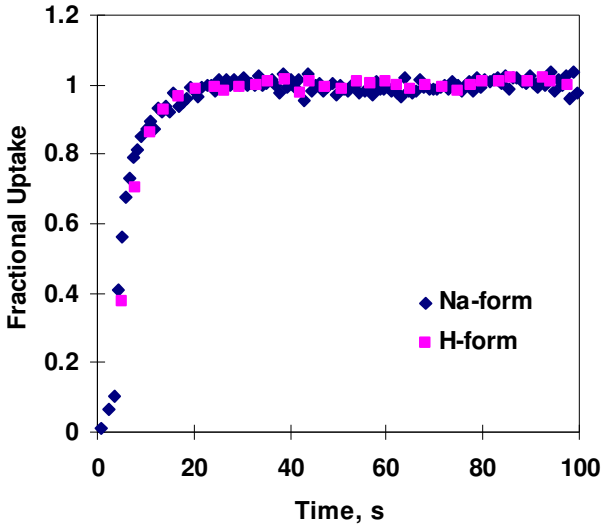

(b)

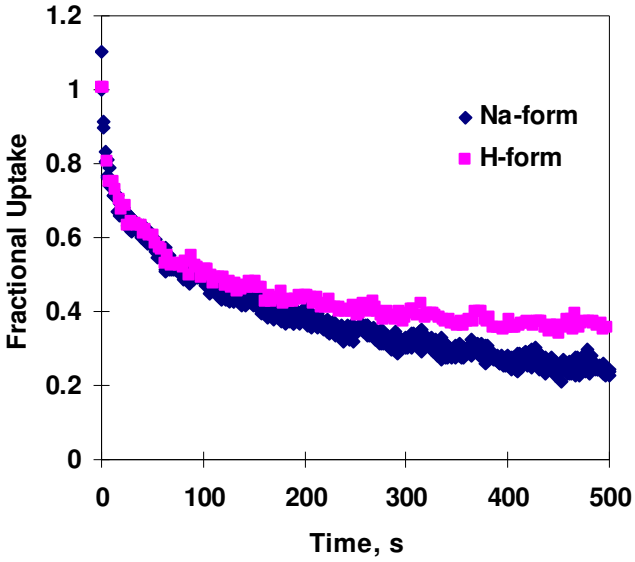

(c)

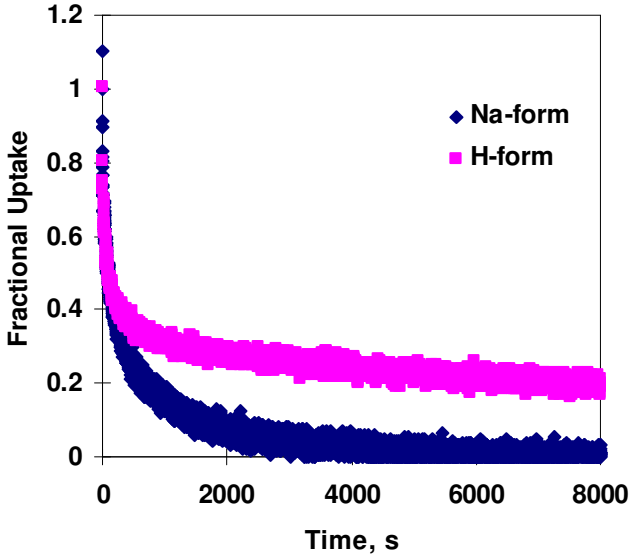

Figure 5-12. TEOM profiles on H-form β-zeolite (with sample size of 2.4 mg) and Na-form β-zeolite (with sample size of 2.3 mg) following 224-TMP step input and 224-TMP desorption by helium purging (T = 373 K, carrier gas is helium flowing at 400 sccm, P_{total} = 1.1 bar, $P_{224\text{-TMP}}$ = 0.006 bar): (a) adsorption profiles; (b, c) desorption profiles.

In addition, the impact of temperature on the desorption kinetics of 224-TMP from H-form β-zeolite was investigated. The desorption dynamics are extremely slow at the ambient temperatures preferred for alkylation. The rate of desorption increases with temperature; however, even at 473 K, the total desorption time is more than 50 h, and the tailing effect is significant, as shown in Figure 5-13. The effective micropore diffusivity is estimated to be 4.9×10^{-19} m^2/s in the second desorption stage, assuming the effect diffusivity is constant in the micropores. This diffusivity is at least 7-8 orders of magnitude lower than that of the similar systems [Kärger, 1992], and the discrepancy might be due to the chemisorption in the acidic β-zeolite as mentioned above.

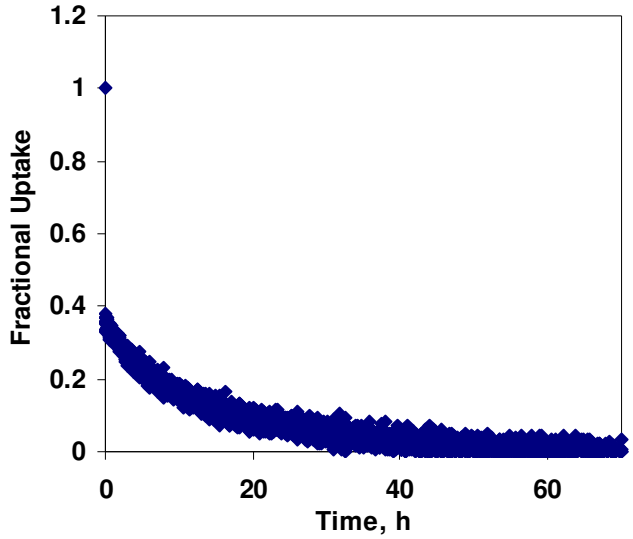

Figure 5-13. TEOM profiles of 224-TMP desorption from β-zeolite by helium purging (T = 473 K, carrier gas is helium flowing at 200 sccm, P_{total} = 1.24 bar, $P_{224\text{-}TMP}$ = 0.007-0 bar).

The effectiveness of regeneration by oxidative burning in air was also tested. As shown in Figure 5-14, the adsorption/desorption dynamics of 224-TMP in β-zeolite are almost identical before and after the regeneration, which was carried out at 773 K in air for approximately 2 h, implying that the oxidative burning is effective to recover the catalyst adsorption/desorption properties (and probably the reaction activity as well).

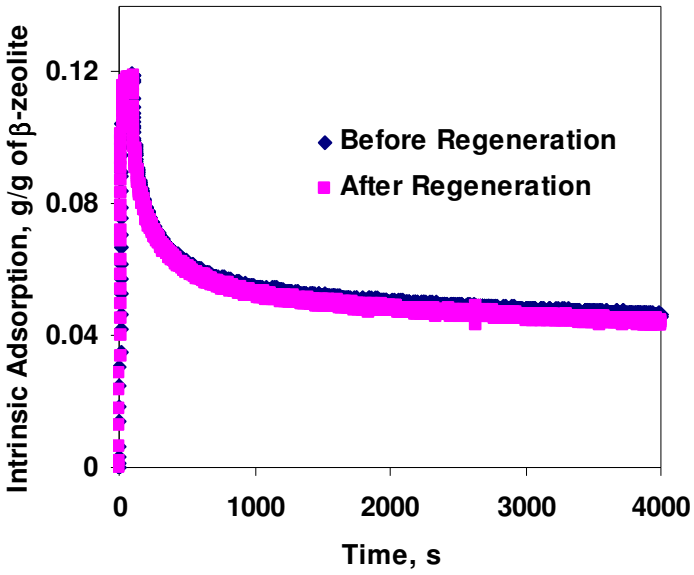

Figure 5-14. The effectiveness of the regeneration by oxidative burning in air (TEOM profiles on β-zeolite following 224-TMP step input and 224-TMP desorption by helium purging, T = 373 K, carrier gas is helium flowing at 200 sccm, P_{total} = 1.3 bar, $P_{224\text{-}TMP}$ = 0.009 bar).

5.4. Adsorption/Desorption Dynamics of 224-TMP in Mesoporous Materials

Intrinsic 224-TMP adsorption/desorption profiles on silica supports Davicat SI 1301 and 1401 (in response to step input changes) were obtained with a TEOM (T = 298-348 K, $P_{224\text{-TMP}}$ = 0-0.3 bar).

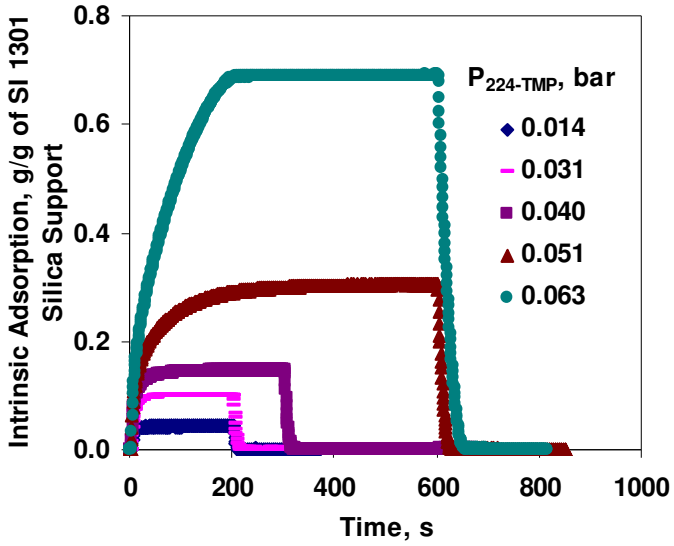

Figure 5-15. TEOM profiles on Davicat SI 1301 silica support following 224-TMP step input and 224-TMP desorption by helium purging (T = 298 K, carrier gas is helium flowing at 200 sccm, P_{total} = 1.2 bar).

Figure 5-15 illustrates the dynamic profiles of 224-TMP adsorption/desorption in Davicat SI 1301 silica support at 298 K under various 224-TMP partial pressures. At 298 K under 224-TMP partial pressure in excess of 0.031 bar, the uptake curves exhibit a two-stage behavior or so-called tailing effect [Ahn, 2004] because of capillary condensation governed by the Kelvin equation. It is observed that capillary

condensation does not occur until the adsorption amount is over 0.1 g/g of silica support at 298 K. These results are in good agreement with the conclusions derived from the equilibrium adsorption isotherms in Chapter 4.

As shown in Figure 5-15, the adsorption profile corresponding to 224-TMP partial pressure of 0.063 bar flattens abruptly at approximately 200 s, indicating that the finite volume in the mesopores is eventually filled up by the adsorbate. As mentioned in Chapter 4, the maximum adsorption capacity is estimated to be 0.79 g/g of silica support, which is fairly close to the measured value (0.69 g/g of silica support).

Under all the operating conditions investigated, desorption of 224-TMP from SI 1301 silica support are facile and complete, indicating excellent pore accessibility of SI 1301 silica support (average pore size 14 nm) for alkylates. Such results could possibly explain the longer catalyst life time observed by Lyon et al. [Lyon, 2004] in silica-supported Nafion catalyst (with mean pore size 9.5 nm).

In the case of 224-TMP adsorption/desorption in Davicat SI 1401 silica support, capillary condensation was not observed under the similar conditions, as shown in Figure 5-16. With such small pores (average pore diameter of 2.3 nm), the SI 1401 silica support has similar adsorption/desorption properties as the microporous materials (e.g., zeolites). In the linear region of equilibrium adsorption isotherm, the rates of adsorption and desorption are identical. In the non-linear region of the equilibrium isotherm, the desorption rate is slower than the adsorption rate. Similar

adsorption/desorption behavior was observed in the study of isobutane, *n*-butane, propane, and CO_2 adsorption/desorption in β-zeolite and USY-zeolite.

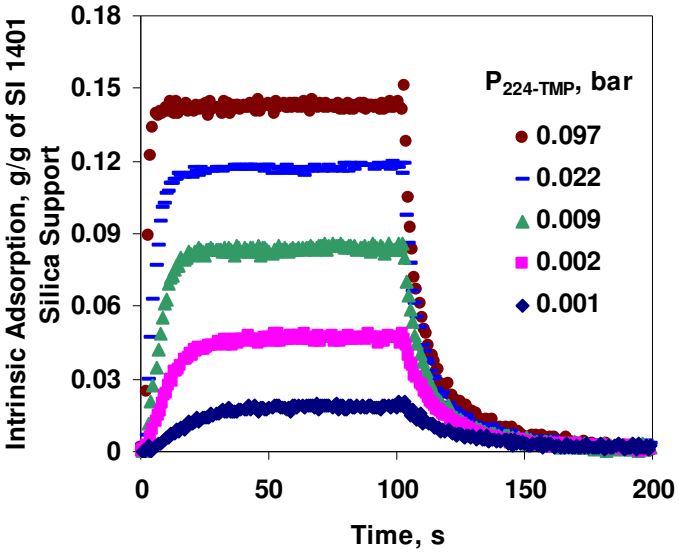

Figure 5-16. TEOM profiles on Davicat SI 1401 silica support following 224-TMP step input and 224-TMP desorption by helium purging (T = 323 K, carrier gas is helium flowing at 200 sccm, P_{total} = 1.04 bar).

The rate of 224-TMP desorption from SI 1401 silica support is much faster than that from β-zeolite, indicating good pore accessibility of SI 1401 silica support for 224-TMP.

Additionally, some preliminary experiments of 224-TMP adsorption/desorption in MCM-41 (with average pore size of 2.8 nm) were also conducted under 224-TMP partial pressure 0-0.04 bar at temperature 295-323 K. It is found that this mesoporous material also provides good pore accessibility for large alkylate molecules such as 224-TMP. At 323 K, when the partial pressure of 224-TMP is higher than 0.027 bar,

the uptake curves show tailing effect, indicating that capillary condensation takes place in the mesopores (Figure 5-17). These results imply that even subtle pore diameter changes (e.g., from 2.3 nm to 2.8 nm) can result in significantly different adsorption/desorption mechanisms.

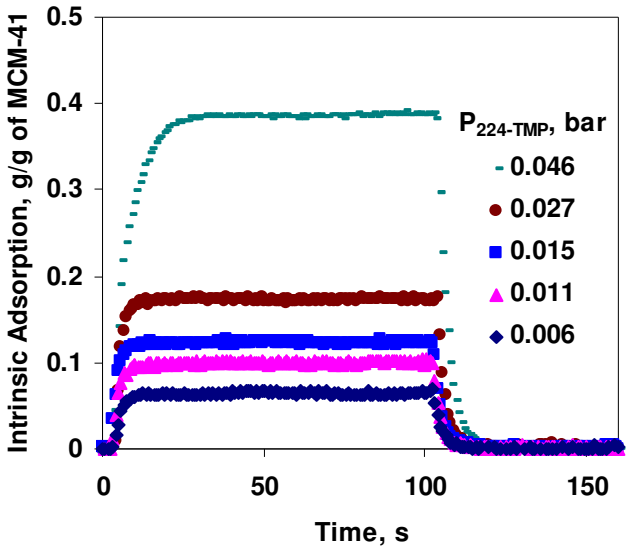

Figure 5-17. TEOM profiles on MCM-41 following 224-TMP step input and 224-TMP desorption by helium purging (T = 323 K, carrier gas is helium flowing at 400 sccm, P_{total} = 1.10 bar).

This study represents the first systematic assessment of the ease of the desired product (224-TMP) desorption from micropores and mesopores. Note that the mesoporous materials employed in this study are neutral (i.e., do not possess any acid site). Under the normal reaction conditions using protonated solid acid catalysts, irreversible chemisorption may occur resulting in slow desorption as observed in the case of 224-TMP in protonated β-zeolite. Therefore, investigations on acidic

mesoporous materials should be carried out in the future to better understand the adsorption/desorption of the desired products (and other compounds) under practically relevant conditions.

References

Ahn, H., Lee, C. H., (2004). Effects of capillary condensation on adsorption and thermal desorption dynamics of water in zeolite 13X and layered beds Chemical Engineering Science 59, 2727-2743.

Alpay, E., Chadwick, D., Kershenbaum, L. S., Barrie, P. J., Sivadinarayana, C., Gladden, L. F., (2003). TEOM analysis of the equilibria and kinetics of *n*-hexane and *n*-heptane adsorption on FCC catalyst/silicalite. Chemical Engineering Science 58, 2777-2784.

COMSOL; 3.0 ed.; COMSOL AB, 2004.

deJong, K. P., Mesters, C. M. A. M., Peferoen, D. G. R., vanBrugge, P. T. M., deGroot, C., (1996). Paraffin alkylation using zeolite catalysts in a slurry reactor: Chemical engineering principles to extend catalyst lifetime. Chemical Engineering Science 51, 2053-2060.

Duong, D. D., (1998) Adsorption analysis: Equilibria and kinetics, Imperial College Press: London, River Edge, NJ.

Kärger, J., Ruthven, D. M., (1992) Diffusion in zeolites and other microporous solids, Wiley: New York.

Lee, C. K., Ashtekar, S., Gladden, L. F., Barrie, P. J., (2004). Adsorption and desorption kinetics of hydrocarbons in FCC catalysts studied using a tapered element oscillating microbalance (TEOM). Part 1: experimental measurements. Chemical Engineering Science 59, 1131-1138.

Lyon, C. J., Sarsani, V. S. R., Subramaniam, B., (2004). 1-butene plus isobutane reactions on solid acid catalysts in dense CO_2-based reaction media: Experiments and modeling. Industrial & Engineering Chemistry Research 43, 4809-4814.

Nivarthy, G. S., He, Y. J., Seshan, K., Lercher, J. A., (1998). Elementary mechanistic steps and the influence of process variables in isobutane alkylation over H-BEA. Journal of Catalysis 176, 192-203.

Ruthven, D. M., Xu, Z., (1993). Diffusion of oxygen and nitrogen in 5A zeolite crystals and commercial 5A pellets. Chemical Engineering Science 48, 3307-3312.

Weitkamp, J., Traa, Y., (1999). Isobutane/butene alkylation on solid catalysts. Where do we stand? Catalysis Today 49, 193-199.

Youngquist, R. G., Allen, J. L., Eisenberg, J., (1971). Adsorption of hydrocarbons by synthetic zeolites. Industrial & Engineering Chemistry Product Research and Development 10, 308-314.

Chapter 6 Conclusions and Recommendations

The major research contributions of this dissertation are in two areas as follows: (1) Guided by the CEBC Industrial Advisory Board, comparative economic and environmental impact analyses of the DuPont/STRATCO sulfuric acid-based 1-butene+isobutane alkylation process and a supercritical CO_2-based solid-acid catalyzed alkylation process were completed to identify the major economic and environmental impact drivers in the two processes and to establish performance targets for any new solid acid alkylation process to be economically competitive with the conventional process. (2) Based on the results of these analyses, follow-up investigations of the adsorption/desorption of model alkylation reactant and product molecules in solid acid catalysts were performed for the first time in a TEOM, contributing to a better fundamental understanding of the causative factors behind the fouling and subsequent deactivation of solid acid catalysts.

The key findings of this dissertation research are summarized in the first section of this chapter. Then, the significance of this work and the recommendations to the future work are provided.

6.1. Key Findings

6.1.1. Economic and Environmental Impact Analyses of Solid Acid Catalyzed Alkylation in Supercritical Carbon Dioxide

Economic and environmental impact assessments of a solid acid/CO_2 alkylation process using SiO_2-supported Nafion catalyst and a conventional sulfuric acid alkylation process (with the same feed refinery stream compositions and the same capacity for alkylate production) have been conducted using plant scale simulations.

The results from the economic analysis show that the total capital investment of the solid acid/CO_2 process is 20-30% higher than that of the sulfuric acid process. For the solid acid/CO_2 process, the utility and chemical costs are 70-80% higher than the sulfuric acid process mainly because of the modest activity of the solid acid catalyst. In addition, it is estimated that the net profit of the solid acid/CO_2 process is 40-50% of the sulfuric acid process. Sensitivity analysis shows that the utility and chemical costs and capital investment would be more or less identical for the two processes if the olefin space velocity (OSV), or catalyst activity, of the solid acid/CO_2 process is increased four-fold from the base-case value while maintaining the same C_8 alkylates productivity.

The environmental impact assessment shows that the sulfuric acid process has an approximately four-fold greater potential for adverse environmental impact than the solid acid/CO_2 process, as inferred from the process composite (toxicity) index. For

the sulfuric acid process, the main pollution comes from the SO_2 emissions during sulfuric acid regeneration (53%) and acid leakage in the alkylation unit (10%); the major contributors to the process composite index are acid rain (66%) and inhalation toxicity (32%). For the solid acid/CO_2 process, the main pollution sources are fugitive emissions; the major contributors to the process composite index are inhalation toxicity (83%), global warming (10%), and acid rain (6%).

6.1.2. Adsorption/Desorption Studies on Solid Acid Alkylation Catalysts Using a TEOM

The TEOM is demonstrated as a useful tool to measure the adsorption equilibria and adsorption/desorption dynamics of hydrocarbons in porous catalysts, and a deeper understanding of adsorption/desorption characteristics of alkylation reactants and products on zeolites and mesoporous materials is successfully gained.

At typical temperatures (303-398 K) reported in the literature for solid acid alkylation catalysis, the equilibrium adsorption isotherms of isobutane, *n*-butane, and propane in USY-zeolite are fitted well by Langmuir model. However, for the same molecules, the dual-site Langmuir model is a better descriptor of the adsorption isotherms in β-zeolite at relatively low temperatures, indicating the existence of perhaps two types of adsorption sites.

The adsorption capacity of 224-TMP (the desired alkylate product) in β-zeolite is 0.09-0.11 g/g of catalyst, nearly identical to that of *n*-butane or isobutane in β-zeolite.

However, the adsorption isotherms of 224-TMP in β-zeolite are not fully reversible under the conditions studied, indicating that adsorbate size has a significant effect on the adsorption affinity.

The dramatic differences in the shapes of equilibrium adsorption isotherms between silica supports Davicat SI 1301 (with average pore size of 14 nm in which capillary condensation occurs) and 1401 (with average pore size of 2.3 nm wherein no capillary condensation occurs) indicate that the pore size has a significant effect on the adsorption/desorption behavior (the influence of acid sites is eliminated because both materials are non-acidic).

Investigations into adsorption/desorption dynamics in large-pore (12-ring) zeolite crystals (< 1 μm) reveal that the corrected intracrystalline diffusivity of isobutane in β-zeolite, estimated from TEOM experiments and complementary single particle model describing simultaneous diffusion and adsorption, is 3-4 orders of magnitude lower than the literature values of similar systems. This implies that an additional mass transfer resistance, other than just the intra-crystalline diffusion resistance, is also influencing the measurements. Designed investigations with pelletized zeolite samples, ranging from 2.0 to 3.5 mm, conclusively show that transport resistances in the extra-crystalline meso- and macropores control the adsorption and desorption dynamics. The experimental adsorption/desorption profiles from the pelletized zeolites were regressed with available mathematical models to obtain effective mesopore/macropore diffusivities for reactant molecules such as isobutane, *n*-butane

and propane. At a given temperature, the effective mesopore/macropore diffusivity (resulting from the nearly perfect fits of the experimental and the modeled profiles) increases with adsorbate loading, mainly due to the decreasing slope of the equilibrium adsorption isotherm. Similar to the zero length column (ZLC) method, the TEOM technique requires the diffusion time scales in the pores to be slow enough for reliable measurement with minimal or insignificant signal dampening from the system dead-volume and dispersion effects. An order of magnitude analysis indicates that a reasonable criterion for reliable measurements of the diffusion time constants by the TEOM technique is: $D/R^2 < 0.02\ s^{-1}$.

Adsorption/desorption profiles of 224-TMP, obtained with a bed of β-zeolite crystals, clearly demonstrate that the bed-length effect is significant under the conditions studied. Even at the highest carrier gas flow rates (i.e., 400 sccm) that eliminate external mass transport resistance, longer beds result in slower rates. The adsorption profiles on the pelleted zeolites are adequately described by the macropore diffusion model, and the estimated zero-coverage effective diffusivity of 224-TMP in β-zeolite pellet at 373 K is approximately 1.2×10^{-6} cm^2/s. In sharp contrast, each desorption profile is characterized by a rapid initial decrease in mass (i.e., a desorption burst that scales with t/R_p^2), followed by a rather long transient that approaches complete desorption asymptotically. These results imply that while the initial desorption rate is controlled by diffusion of species in the extra-crystalline space, the extremely long transient is due to the slow diffusion of species in the pores

of the zeolite crystals. In other words, the product molecule experiences severe transport limitations.

Identical adsorption/desorption experiments of 224-TMP performed with H-form and sodium-exchanged β-zeolites showed that while the adsorption and the initial part of the desorption profiles are identical in both cases, the second stage of desorption is significantly slower in the H-form β-zeolite compared to the Na-form β-zeolite, possibly due to the strong chemisorption of 224-TMP in the H-form β-zeolite.

Even at 473 K, the total desorption time in β-zeolite for 224-TMP is more than 50 h, and the tailing effect is significant. Clearly, the desorption of 224-TMP from β-zeolite is hindered such that its accumulation will eventually lead to catalyst deactivation by fouling. It was found that 224-TMP can be completely burned off by air oxidation at 773 K for 2 h. The adsorption and desorption profiles in the regenerated catalyst are identical to those observed prior to deactivation.

These results along with the fact that the mesoporous materials provide good pore accessibility for large alkylate molecules such as 224-TMP explain the longer catalyst life time observed by Lyon et al. [Lyon, 2004] in silica-supported Nafion catalyst.

6.2. Recommendations

The economic and environmental impact analyses conducted in this work successfully guided the research activities of solid acid testbed at CEBC and provided a valuable framework. This approach is strongly recommended to be further utilized in the future research not only for alkylation but also for other reaction systems.

As more data become available, the economic and environmental impact analyses of solid acid catalyzed alkylation processes should be continually updated to identify the performance targets and benchmarks for economic viability and also to guide process development (e.g., reactor design and regeneration method).

The results from this dissertation are in excellent agreement with the conclusions by Kärger and Ruthven [Kärger, 1992] that the adsorption/desorption dynamics of hydrocarbons in large-pore zeolites with small crystals are controlled by extracrystalline diffusion. Therefore, larger crystals with longer diffusion length is recommended to be used to reliably measure the intracrystalline diffusivity with the TEOM. To experimentally determine whether the intracrystalline diffusion is the rate-limiting step, systematic investigations of adsorption/desorption dynamics with different sizes of crystals should be carried out under identical conditions. Similarly, systematic investigations must be undertaken to better understand the effects of acidity of β-zeolites and other solid acid catalysts such as SiO_2-supported Nafion on the adsorption/desorption kinetics of probe molecules.

The size and structure of the catalyst pores have strong effects on the adsorption/desorption dynamics that in turn have significant influences on the catalytic performance of the solid acid catalysts. Yoo and coworkers [Yoo, 2001] systematically investigated the impacts of structure on the reaction performance of one-, two-, and three-dimensional zeolites, and found that the specific pore structures of β-zeolite and ZSM-12 result in better stabilities. A similar study focusing on the effects of pore structure on adsorption/desorption dynamics would offer a deeper understanding of the correlation between the catalytic performance and pore structures.

In this dissertation, C_3, C_4, and C_8 alkanes were chosen as the model compounds of reactants and products. In the future, adsorption/desorption studies of the heavier products (e.g., C_{12} and C_{16} alkanes) and C_4 olefins in various solid acid catalysts should be performed to get a clearer picture of the catalyst deactivation during alkylation.

The TEOM technique could also be employed in the alkylation reaction (and coking) studies. Even though the reaction can only be investigated in the gas phase because of the limitations of the TEOM technique, such a study would possibly result in a better understanding of the deactivation mechanism and intrinsic reaction kinetics. This type of investigation should, of course, include the evaluation of catalyst regeneration methods (e.g., regeneration using H_2) for potential industrial applications.

TEOM should also be implemented to study other reaction systems, on which the advantages of this technique can be fully taken. For example, it could be employed in the kinetic measurement of biomass pyrolysis. Currently, thermogravimetry (TG) is the method of choice for the fundamental kinetic characterization of biomass pyrolysis. Unfortunately, the TG technique suffers from significant systematic errors of temperature measurement and intrusions of unwanted secondary gas-solid reactions [Antal, 1995; Narayan, 1996; Antal, 1997; Antal, 1998]. The significant enhancement in the external mass and heat transfer for the biomass samples and the ability of measuring true sample temperature make TEOM a superior tool over thermogravimetric analyzer (TGA) for the studies of biomass pyrolysis kinetics.

References

Antal, M. J., Varhegyi, G., (1995). Cellulose pyrolysis kinetics - The current state knowledge. Industrial & Engineering Chemistry Research 34, 703-717.

Antal, M. J., Varhegyi, G., (1997). Impact of systematic errors on the determination of cellulose pyrolysis kinetics. Energy & Fuels 11, 1309-1310.

Antal, M. J., Varhegyi, G., Jakab, E., (1998). Cellulose pyrolysis kinetics: Revisited. Industrial & Engineering Chemistry Research 37, 1267-1275.

Kärger, J., Ruthven, D. M., (1992) Diffusion in zeolites and other microporous solids, Wiley: New York.

Lyon, C. J., Sarsani, V. S. R., Subramaniam, B., (2004). 1-butene plus isobutane reactions on solid acid catalysts in dense CO_2-based reaction media: Experiments and modeling. Industrial & Engineering Chemistry Research 43, 4809-4814.

Narayan, R., Antal, M. J., (1996). Thermal lag, fusion, and the compensation effect during biomass pyrolysis. Industrial & Engineering Chemistry Research 35, 1711-1721.

Yoo, K., Burckle, E. C., Smirniotis, P. G., (2001). Comparison of protonated zeolites with various dimensionalities for the liquid phase alkylation of *i*-butane with 2-butene. Catalysis Letters 74, 85-90.

Appendices

A: Calibration of Mass Flow Controllers and Pressure Transducers

The mass flow controllers employed in this dissertation research were calibrated against a wet test meter (GCA/Precision Scientific). The OMEGA pressure transducers used for the TEOM inlet/outlet pressure measurements were calibrated against a Cole-Parmer digital pressure gauge (EW-68332-02), which was calibrated and certified by the manufacturer to ±0.15 psig.

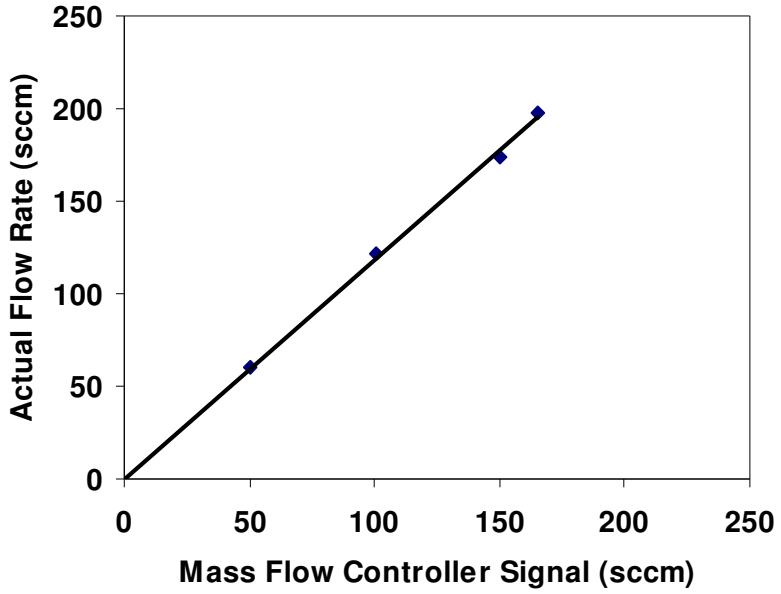

Figure A-1. Mass flow controller calibration (MFC-1: Brooks 5850 E).

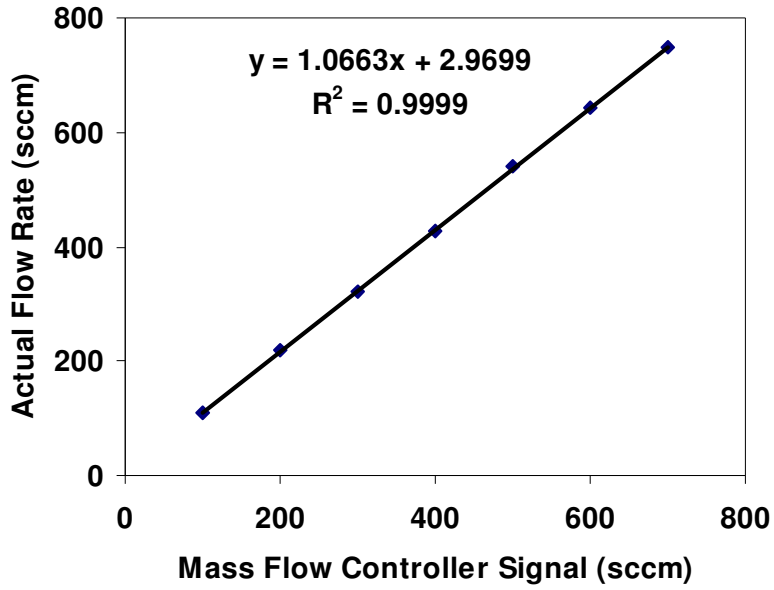

Figure A-2. Mass flow controller calibration (MFC-2: OMEGA FMA766A).

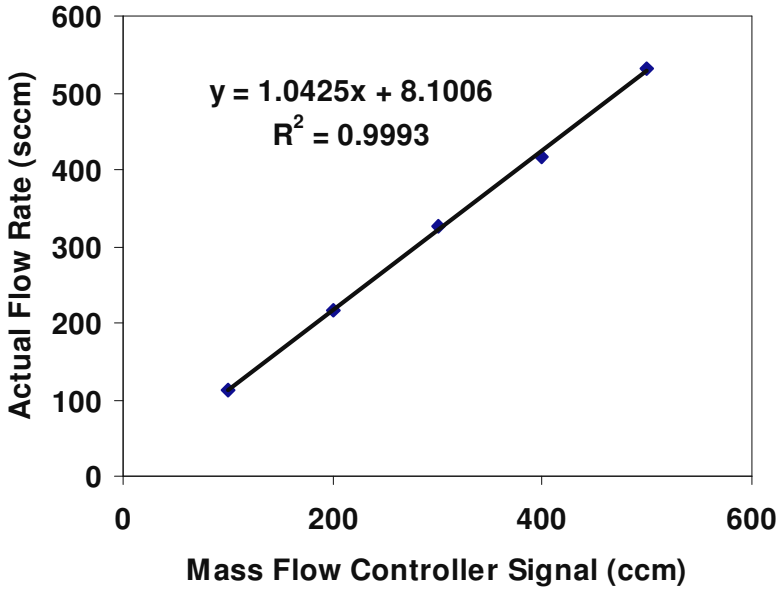

Figure A-3. Mass flow controller calibration (MFC-3: OMEGA FMA-766A).

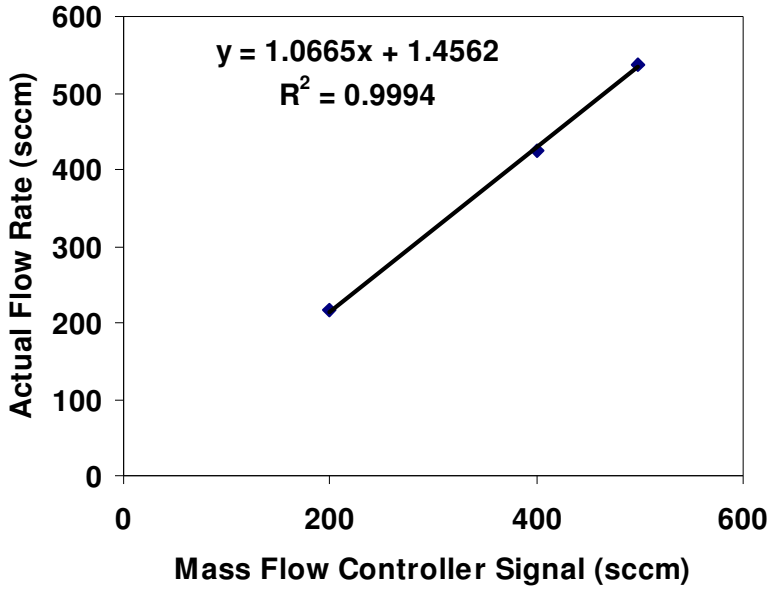

Figure A-4. Mass flow controller calibration (MFC-4: OMEGA FMA-767A).

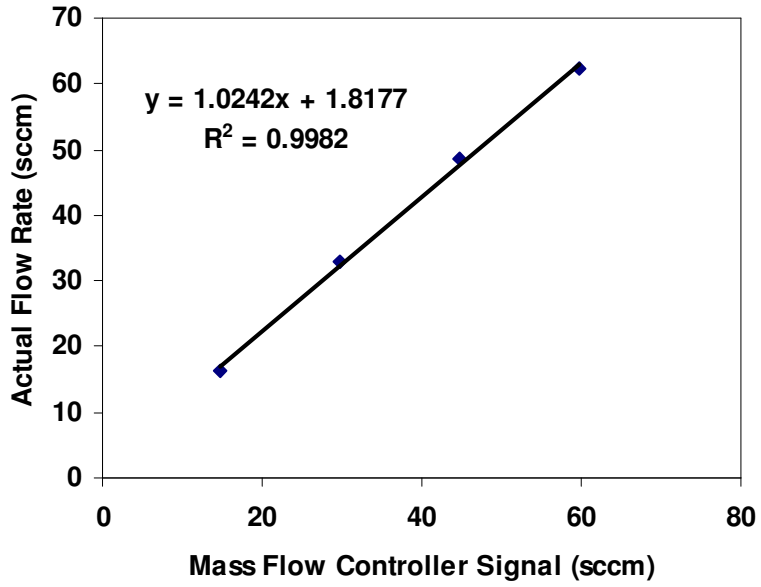

Figure A-5. Mass flow controller calibration (MFC-5: OMEGA FMA-763A).

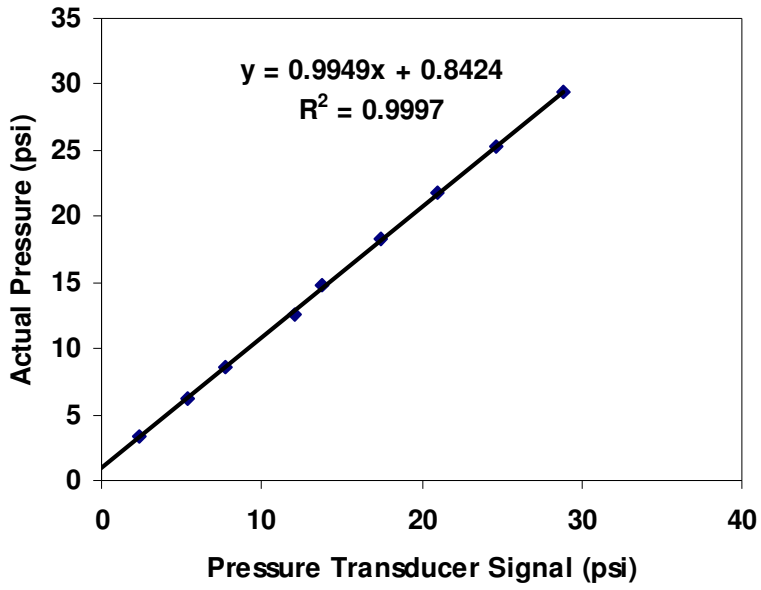

Figure A-6. Pressure transducer calibration (PT-1: OMEGA PX4201-060GV).

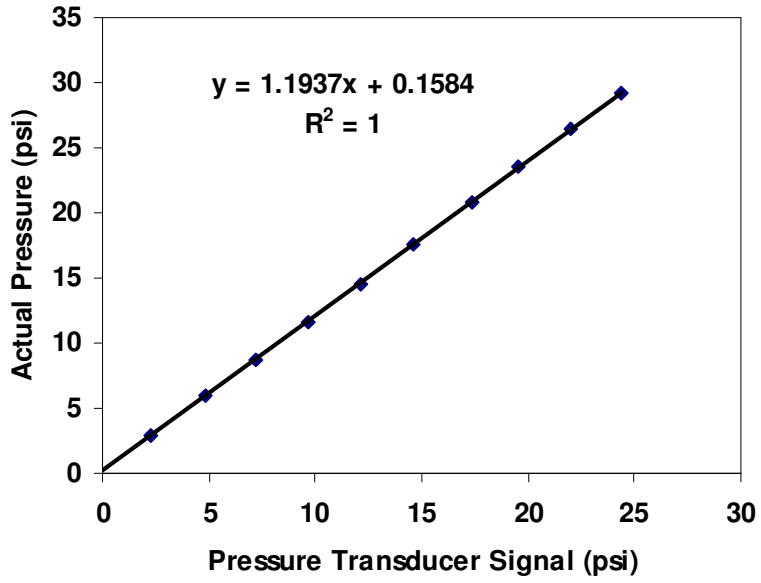

Figure A-7. Pressure transducer calibration (PT-4: OMEGA PX302-050GV).

B: TEOM Front Panel Setting for Mass Flow Controllers and Pressure Transducers

The constants for the mass flow controllers and pressure transducers in the TEOM front panel setting are listed in Table B-1. Each file shown in the table is employed for a specific substrate of interest, for example, file UKansas.FP is used when isobutane is the adsorbate in the experiments. The other TEOM front panel settings, such as the PID control constants for the heaters, were specified by the manufacturer.

Table B-1. TEOM front panel setting for mass flow controllers and pressure transducers.

	MFC-1	**MFC-2**	**MFC-3**	**MFC-4**	**MFC-5**	**PT-1**	**PT-4**
File: UKansas.FP							
Gas	He	He	He	butane	butane	/	/
Constant	0.0240	0.00693	0.00693	0.0192	0.385	0.00167	0.00200
File: Ukansas-01.FP							
Gas	He	He	He	He	He	/	/
Constant	0.0240	0.00693	0.00693	0.00346	0.0693	0.00167	0.00200
File: Ukansas-02.FP							
Gas	He	He	He	CO_2	CO_2	/	/
Constant	0.0240	0.00693	0.00693	0.00671	0.134	0.00167	0.00200
File: Ukansas-03.FP							
Gas	He	He	He	propane	propane	/	/
Constant	0.0240	0.00693	0.00693	0.0134	0.269	0.00167	0.00200

The mass flow controllers used were calibrated by the manufacturers with N_2 under certain operating conditions. In this study, these mass flow controllers work with gases other than the original calibration gas N_2. The constant of a mass flow controller in the front panel setting is calculated as the full signal range divided by the full scale of new gas flow rate. For example, the following calculation procedures

were used to obtain the constant in the front panel setting for the mass flow controller MFC-2 (OMEGA FMA-766A) when the flow rate of He gas is controlled: given that the full scale of N_2 flow rate in the mass flow controller is 500 sccm, and that the conversion factors for N_2 and He is 1.000 and 1.444, respectively, the full scale of He gas flow rate is therefore $500 \times 1.444 / 1.000 = 722$ sccm; given that the full scale of the signal is 5 V, it follows that the constant in the front panel setting is: 5/722 = 0.00693 V/sccm.

The constants for the pressure transducers in the front panel setting were calculated as the full signal ranges divided by the full scales of pressure measurements. For example, for PT-1 (OMEGA PX-4201-060GV), given that the full signal range is 0.1 V and that the full scale of pressure measurement is 60 psig, the constant is therefore 0.1/60 = 0.00167 V/psig.

C: TEOM Service and Calibration

The TEOM service conditions and outputs are listed in Table C-1 and C-2, respectively. The results of the spring constant calibration for the tapered element are shown in Table C-3. The parameter definition and calibration procedure are available elsewhere [R&P, 2000].

Table C-1. TEOM service conditions.

Items	**Specifications**	**Items**	**Specifications**
Serial No.	779	Average time	10 s
Sample holder size	0.10 cc	Gate time	0.8 s
Balance weight (left)	496 g	TC used	wall
Balance weight (right)	0 g	Amplitude	500
K_0	1861	AGC gain	200
Basic frequency with cap	43	SW1	up
Sample	out	Cap	on

Table C-2. The outputs of the TEOM services.

Date	**TP0**	**DC offset**	**TP1**	**TP2**	**TP3**	**TP4**	**VDC**	**TP5**	**NSD**	**Freq**	**Notes**
02/25/2004	5.3	-4.8	10.2	15.7	1.3	1.6	1.3	17.6	1-3	43.445	Ambient T and P
02/25/2004	5.1	-5	10.2	15.5	2	2.1	1.1	17.6	2-4	43.472	600 ^{o}C, ambient P
02/25/2004	4.8	-5	10.2	15	2.8	1.8	1.8	17.6	2-5	43.413	600 ^{o}C, 56 atm
06/03/2005	5.2	-4.5	10.1	15.5	3.7	1.9	2.1	16.7	2-4	43.423	Ambient T and P
06/09/2005	5.6	-4.5	10.6	16.1	3.3	2.8	1.5	16.7	1-3	43.452	150 ^{o}C, ambient P
06/09/2005	5.5	-4.5	10.5	15.9	3.1	2.8	1.4	16.7	2-4	43.463	600 ^{o}C, ambient P
09/07/2005	5.2	-4.0	10.1	16.1	3.1	1.1	1.8	17.0	1-4	43.414	Ambient T and P
09/07.2005	5.5	-4.0	10.2	16.1	3.0	1.1	1.6	17.0	1-4	43.443	150 ^{o}C, ambient P

Table C-3. The calibration of spring constant for the tapered element (calibration conditions: T = 323 K, gas flow rate = 0 sccm, atmospheric pressure).

Date	f_0	f_1	**Cap weight**	K_0
02/25/2004*	N/A	N/A	N/A	1861.0
02/08/2006	51.7026	43.4392	290.69 mg	1865.1
12/18/2006	51.7250	43.4664	290.00 mg	1864.7
07/01/2007	51.7475	43.4737	290.27 mg	1864.6

* Calibrated by the manufacturer (Rupprecht & Patashnick Co., Inc.).

Reference

R&P, (2000) Operating manual: TEOM series 1500 pulse mass analyzer. Rupprecht & Patashnick Co., Inc.: Albany, NY.

D: Repeatability of Experiments

The repeatability of experiments is exemplified by the measurements of adsorption/desorption profiles of isobutane in β-zeolite, as shown in Figure D-1. In this dissertation research, excellent repeatability of the TEOM measurements is obtained.

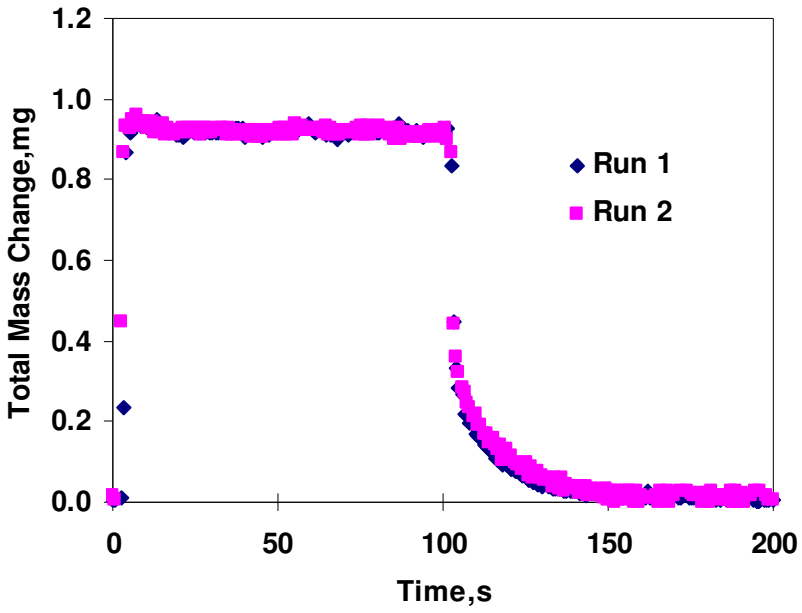

Figure D-1. Repeatability test for the adsorption/desorption experiments (T = 373 K, P_{iC4} = 0.23 bar, F_{total} = 200 sccm, P_{total} = 1.01 bar, β-zeolite loading = 6.7 mg).

E: Stability of TEOM Temperature/Pressure during Sorption Experiments

Typical TEOM temperature and pressure profiles obtained during the adsorption/desorption experiments are shown in Figure E-1. It can be seen that the temperature and pressure are not disturbed when the valve 1 is switched.

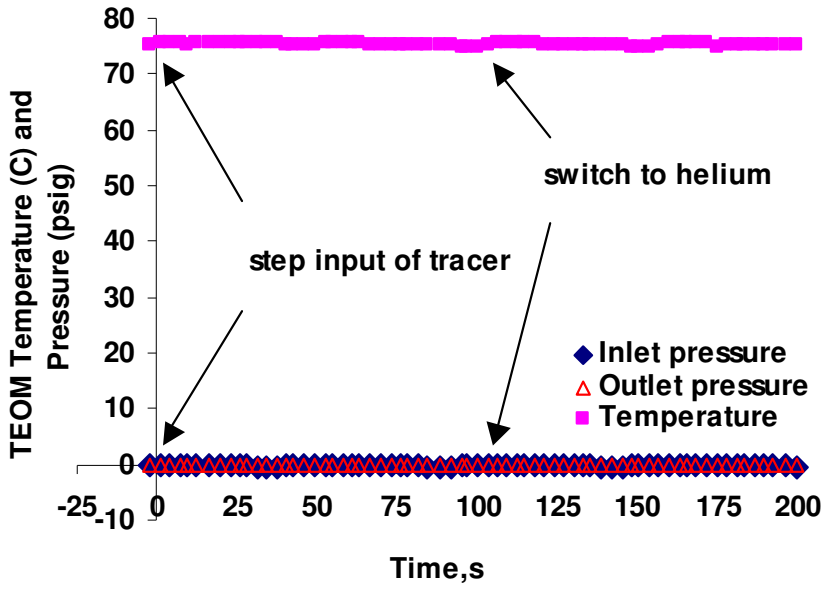

Figure E-1. Typical TEOM temperature and pressure profiles obtained during the adsorption/desorption experiments (*n*-butane adsorption/desorption in USY-zeolite, P_{nC4} = 0.253 bar, F_{total} = 200 sccm, USY-zeolite sample size = 9.6 mg).

F: Report on the Acidity Measurements of USY-zeolite, β-zeolite, and MCM-41

F-1: Objective

To determine the acidity values of USY-zeolite, β-zeolite, and MCM-41 using the ammonia temperature-programmed desorption (TPD) method.

F-2: Experimental

The TPD experiments were conducted at ConocoPhillips using a Micromeritics ASAP 2910 sorption analyzer equipped with a thermal conductivity detector (TCD). Before TPD experiments, the internal loop of the equipment was calibrated to get area under the curve corresponding to a known NH_3 concentration. Blank experiments were conducted before actual TPD runs to determine NH_3 uptake. For TPD runs, about 0.2 g of catalyst was placed in a glass U-tube sandwiched between the quartz wool. Before TPD experiments, the sample was heated to 623 K at 50 K/min and held there for 10 min to remove moisture. The temperature was then decreased to 303 K and the flow of 15% NH_3/He was started. After 60 min, the flow of NH_3/He was stopped and the flow of He was started and continued for 30 min to remove any physisorbed NH_3. Following this, the temperature was ramped from ambient to 873 K at 3 K/min and the desorbing NH_3 was detected using TCD. Following this temperature ramp, the sample was cooled down to ambient temperature.

F-3: Results

Blank experiments did not show any NH_3 uptake. The acidity values of catalysts are shown in Table F-1. The TPD profiles of USY-zeolite, β-zeolite and MCM-41 are shown in Figures F-1, F-2, and F-3, respectively. From Figures F-1 and F-2, it is observed that the profiles were composed of 3 individual peaks corresponding to weak, intermediate, and strong acid sites. In order to get the acidity values for these acid sites, the profiles were deconvoluted using equation F-1:

$$TPD_{model} = \sum_{i=1}^{3} A_i \exp\left(-\frac{(T - B_i)^2}{2C_i^2}\right) \qquad \text{(F-1)}$$

Table F-1. Acidity values of USY-zeolite, β-zeolite, and MCM-41.

Catalyst	Acidity (Exp 1)	Acidity (Exp 2)	Acidity (Exp 3)	Average Acidity	Std.Dev
	(μmole NH_3/g cat)	(μmole NH_3/g cat)	(μmole NH_3/g cat)	(μmole NH_3/g cat)	
USY-zeolite	480.20	455.60	462.30	466.03	12.72
β-zeolite	256.50	314.90	302.20	291.20	30.71
MCM-41	160.50	157.80	166.05	161.45	4.21

Using the above model, the deconvoluted Gaussian peaks were obtained, and concentrations of weak, intermediate, and strong acid sites were calculated. The contributions of these acid sites (obtained from the model) in total acidity are shown in Table F-2 and F-3 for USY-zeolite and β-zeolite, respectively. The deconvoluted peaks for USY-zeolite and β-zeolite are shown in Figure F-4 and F-5, respectively.

The total acidity values obtained from the model were in close agreement with the experimental values for both USY-zeolite and β-zeolite.

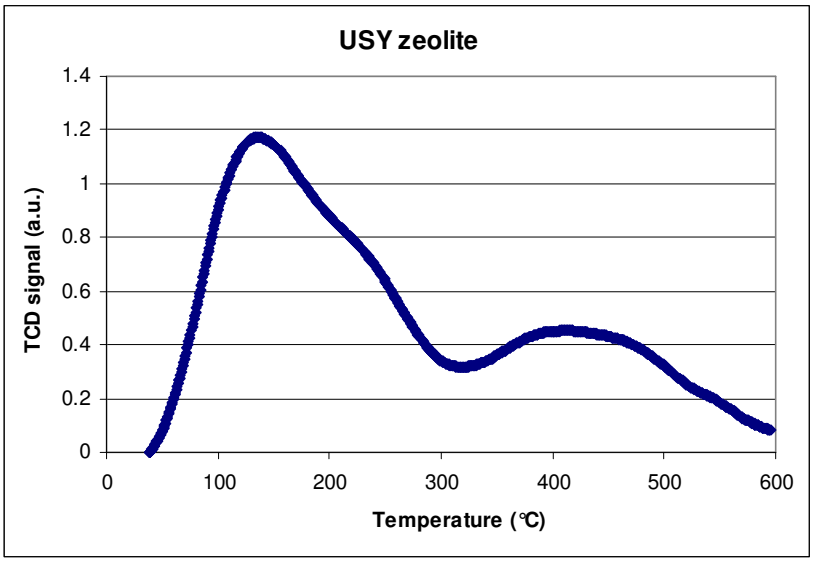

Figure F-1. TPD profile of USY-zeolite.

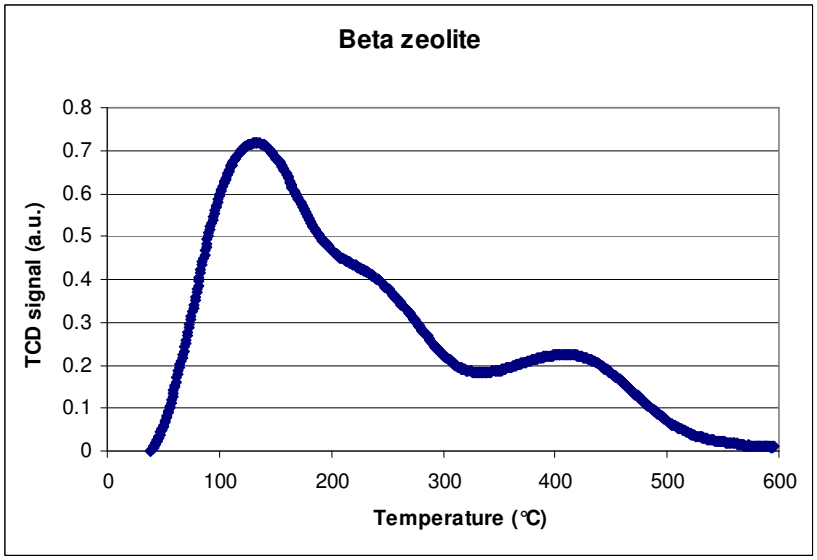

Figure F-2. TPD profile of β-zeolite.

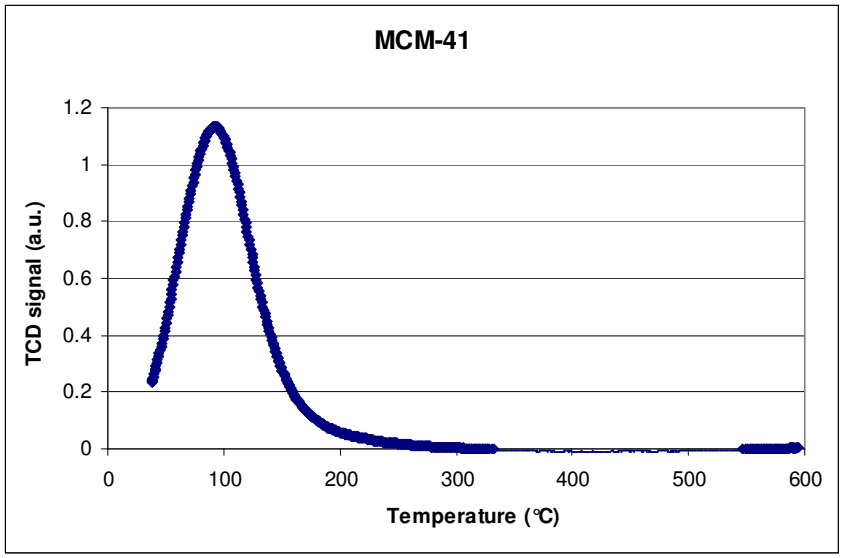

Figure F-3. TPD profile of MCM-41.

The results showed that USY-zeolite had the highest acidity value of 466 μmole NH_3/g cat with intermediate acid sites being the main contributing sites while MCM-41 was the least acidic with an acidity value of 161 μmole NH_3/g cat (which is also evident from the single peak at lower temperature as observed in Figure F-3).

Table F-2. Contributions of weak, intermediate, and strong acid sites (obtained from the model) in total acidity of USY-zeolite for experimental run 3.

	Area	Acidity (μmole NH_3/g cat)	% acidity	Signal Max	T_{max} (K)	Heat of adsorption (kJ/mol)
Weak sites (Peak 1)	85.46	141.64	30.57%	1.000	370.48	95.83
Intermediate sites (Peak 2)	129.61	214.82	46.36%	0.760	457.02	119.01
Strong sites (Peak 3)	64.52	106.93	23.08%	0.361	694.88	183.37
Total	279.60	463.39				

Table F-3. Contributions of weak, intermediate, and strong acid sites (obtained from the model) in total acidity of β-zeolite for experimental run 2.

	Area	Acidity (μmole NH_3/g cat)	% acidity	Signal Max	T_{max} (K)	Heat of adsorption (kJ/mol)
Weak sites (Peak 1)	57.73	119.90	37.66%	0.587	381.55	98.78
Intermediate sites (Peak 2)	70.42	146.25	45.94%	0.396	479.86	125.15
Strong sites (Peak 3)	25.13	52.19	16.39%	0.205	682.38	179.96
Total	153.27	318.33				

From the T_{max} value of each peak, the heats of adsorption were calculated for USY-zeolite and β-zeolite (Table F-2 and F-3) using the Redhead equation as shown in equation F-2 [Sakakini, 1997]:

$$\Delta H_{ads} = RT_{max}\left[\ln\left(\frac{AT_{max}}{\beta}\right) - 3.64\right] \qquad \text{(F-2)}$$

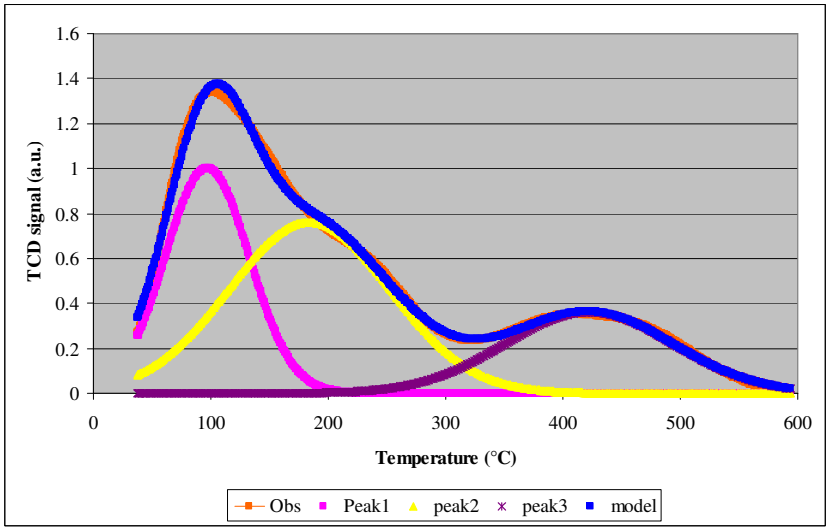

Figure F-4. Deconvoluted TPD peaks for USY-zeolite.

where R is the gas constant, T_{max} is the temperature corresponding to the maximum value of the peak, A is the pre-exponential factor of desorption (with a value of 10^{13} K^{-1}), and β is the heating rate.

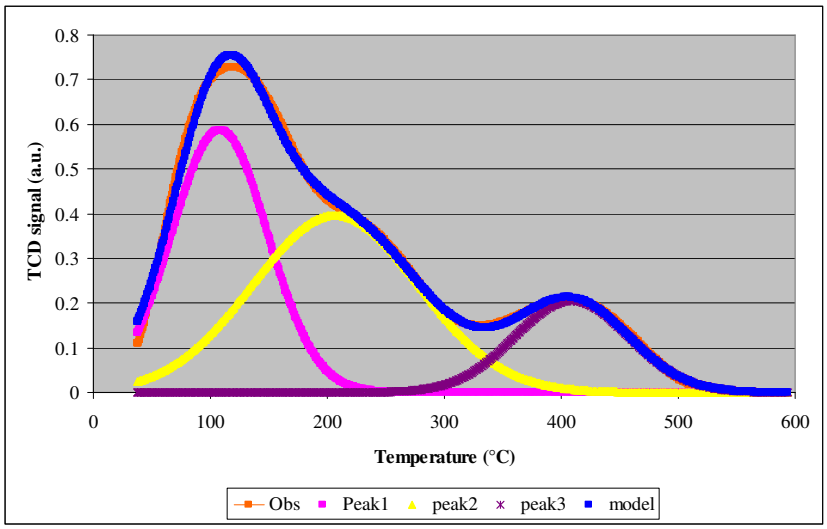

Figure F-5. Deconvoluted TPD peaks for β-zeolite.

F-5: Reference

Sakakini, B. H., Verbrugge, A. S., (1997). Temperature-programmed surface reaction as a means of characterizing supported-metal catalysts and probing their surface reactivity. Journal of Chemical Society, Faraday Transactions 93, 1637-1640.